2020

Design, microstructure and properties of metastable beta-type biomedical titanium alloys

Syed Faraz Jawed

Edith Cowan University

Copyright Warning

DESIGN, MICROSTRUCTURE AND PROPERTIES OF METASTABLE BETA-TYPE BIOMEDICAL TITANIUM ALLOYS

This thesis is submitted in fulfillment of the requirement for the degree of

Doctor of Philosophy

By:

Syed Faraz Jawed

Principal Supervisor:

Prof. Lai-Chang Zhang

Associate supervisor:

Dr. Liqiang Wang

(Shanghai Jiao Tong University)

School of Engineering

Edith Cowan University (ECU)

2020

Page deliberately left blank

Abstract

Many existing implant biomaterials including cobalt-chromium alloy, stainless steel, Ti-6Al-4V and commercially pure titanium have all been shown to demonstrate mechanical incompatibility, poor osseointegration and/or cause cytotoxic effects on the human body after some years of application, leading to revision surgery in most cases. Consequently, there is an immediate need for an enduring biomaterial that displays good mechanical properties and possesses biocompatibility and corrosion resistance, in order to reduce rates of revision surgeries. In this PhD work, based on the $\overline{Bo}$-$\overline{Md}$, $\overline{e/a}$-$\overline{\Delta r}$ and *BF-d-electron superelastic* theoretical relationships four new series of quaternary Ti-25Nb-8Zr-xCr, Ti-25Nb-xSn-yCr, Ti-26Nb-xMn-yZr and Ti-25Nb-xMn-ySn alloys have been designed for the first time. These designed alloys were produced using the cold crucible levitation melting method, where the effect of balanced combination of β-isomorphous (Nb), β-eutectic (Cr, Mn) and neutral (Zr, Sn) elements on phase transformation, β-phase stability and mechanical properties of the alloys are investigated.

Microstructural investigations of Ti-25Nb-8Zr-xCr (x = 0, 2, 4, 6, 8) demonstrate a single β phase, with the exception of Ti-25Nb-8Zr-0Cr which shows dual α" and β phases. Furthermore, the addition of Cr is shown to be effective in achieving a single β phase where suppressing the formation of α" phase. As the content of Cr increases, the yield strength (382-773 MPa) and hardness (1.91-2.63 GPa) also increase in Ti-25Nb-8Zr-xCr alloys. Notably, all the investigated alloys demonstrated significant strain hardening rates.

The Ti-25Nb-xSn-yCr (x = 1, 3, 5 wt% and y= 2, 4 wt%) alloys demonstrated only β phase in their microstructures. It is of note that all Ti-25Nb-xSn-yCr alloys displayed large plasticity of ~80% without failure during mechanical testing. Yield strength, hardness and elastic modulus were (314-463) MPa, (2.36-1.93) GPa and (66-78) GPa, respectively. Ti-25Nb-1Sn-2Cr possessed the higher values of wear resistance indices (i.e. *H/E* and $H^3/Eeff^2$) as compared to commercially pure titanium and Ti-6Al-4V.

The Microstructural features of Ti-26Nb-xZr-yMn (x = 4, 7, 10 wt% and y = 3, 5 wt%) alloys revealed a monolithic β phase. Notably, none of the alloys displayed failure and demonstrated substantial true plasticity of ~160% during mechanical compression testing. Yield strength, hardness and dislocation density were (609-451) MPa, (242-207) HV and (2.45×10^{15}-0.4×10^{15}) m^{-2}, respectively. Additionally, Ti-26Nb-4Zr-5Mn demonstrates good strain hardening ability

and electrochemical kinetics in terms of high strain hardening indices (0.42 and 0.09) and small corrosion current density (0.839 nA/cm^2), respectively.

In Ti-25Nb-xMn-ySn (x = 2, 4 wt% and y = 1, 5 wt%) alloys, it was found that only Ti-25Nb-2Mn-1Sn displayed dual β and α" phases while others showed a monolithic β phase. Yield strength, hardness and superelastic recovery ratio were (710-563) MPa, (244-207) HV and (90-80) %, respectively. It is of noteworthy; Ti-25Nb-4Mn-1Sn displays the low elastic modulus and high energy absorption.

The results demonstrate that among the investigated alloys Ti-25Nb-8Zr-4Cr, Ti-25Nb-1Sn-2Cr, Ti-26Nb-4Zr-5Mn and Ti-25Nb-4Mn-1Sn display superior combination of mechanical properties making them suitable materials for implant applications.

Declaration

I certify that this PhD thesis does not, to the best of my knowledge and belief:

- Incorporate without acknowledgment any material previously submitted for a degree or diploma in any institution of higher education;
- Contain any material previously published or written by another person except where due reference is made in the text of this thesis; or
- Contain any defamatory material.

Syed Faraz Jawed

07/12/2020

Page deliberately left blank

Acknowledgements

First of all, praises and thanks to the Allah (S.W.T), the Almighty for His countless blessings upon me, which gives me strength and understanding to complete this Ph.D. work successfully.

I would like to express my sincere and deep gratitude to my supervisor Prof. Lai-Chang Zhang for providing me the opportunity to be the part of his top-quality research group and for his valuable guidance throughout this Ph.D. work. I have always been motivated through his sincerity, vision and dynamism. I have greatly improved my research knowledge and academic skills based on his proficient comments and advice. It was a great honor and privilege for me to work under his guidance and support. I would also like to thank Dr. Liqiang Wang and Dr. Kevin Hayward for being my associate supervisors and for providing good suggestions during this Ph.D. work. I would like to extend my thanks to Mr. Adrian Styles and Mr. Adrian Davis for giving me a technical support during this work.

I would like to further extend my thanks to Dr. Yujing Liu for providing me an opportunity to conduct many of the experiments at The University of Western Australia and for providing his valuable time and skilled suggestions. I would like to present my heartiest thanks to my senior colleague and sincere friend Dr. Chirag Rabadia who always gave his support, time and guidance throughout this Ph.D. tenure. I would also like to thank my colleagues Dr. Shunxing Liang, Mr. Jincheng Wang and Mr. Peng Qin for their kind help and support throughout this work.

I am extremely grateful to my parents and parents-in-law for their prayers, love, sacrifices and encouragement. I would like to express my heartiest gratitude to my incredibly patient wife Dr. Mehwish for her constant support and unconditional love, she has made countless sacrifices and always encouraged me throughout this journey.

Page deliberately left blank

List of Publications

A) First-authored peer reviewed journal publications

1. **S.F. Jawed**, Y.J. Liu, J.C. Wang, C.D. Rabadia, L.Q. Wang, Y.H. Li, X.H. Zhang, L.C. Zhang, Tailoring deformation and superelastic behaviors of beta-type Ti-Nb-Mn-Sn alloys, J. Mech. Behav. Biomed. Mater. 110 (2020) 103867. https://doi.org/10.1016/j.jmbbm.2020.103867

2. **S.F. Jawed**, C.D. Rabadia, Y.J. Liu, L.Q. Wang, P. Qin, Y.H. Li, X.H. Zhang, L.C. Zhang, Strengthening mechanism and corrosion resistance of beta-type Ti-Nb-Zr-Mn alloys, Materials Science and Engineering: C 110 (2020) 110728. https://doi.org/10.1016/j.msec.2020.110728.

3. **S.F. Jawed**, C.D. Rabadia, Y.J. Liu, L.Q. Wang, Y.H. Li, X.H. Zhang, L.C. Zhang, Beta-type Ti-Nb-Zr-Cr alloys with large plasticity and significant strain hardening, Materials & Design 181 (2019) 108064. https://doi.org/10.1016/j.matdes.2019.108064.

4. **S.F. Jawed**, C.D. Rabadia, Y.J. Liu, L.Q. Wang, Y.H. Li, X.H. Zhang, L.C. Zhang, Mechanical characterization and deformation behavior of β-stabilized Ti-Nb-Sn-Cr alloys, Journal of Alloys and Compounds 792 (2019) 684-693. https://doi.org/10.1016/j.jallcom.2019.04.079.

B) Co-authored peer reviewed journal publications

1. C.D. Rabadia, Y.J. Liu, **S.F. Jawed**, L.Q. Wang, H. Sun, L.C. Zhang, Deformation and toughness behavior of β -type titanium alloys comprising C15-type Laves phase, Materials Today Sustainability 9 (2020) 100034. https://doi.org/10.1016/j.mtsust.2020.100034.

2. C.D. Rabadia, Y.J. Liu, C.H. Zhao, J.C. Wang, **S.F. Jawed**, L.Q. Wang, L.Y. Chen, H. Sun, L.C. Zhang, Improved trade-off between strength and plasticity in titanium based metastable beta type Ti-Zr-Fe-Sn alloys, Materials Science and Engineering: A 766 (2019) 138340. https://doi.org/10.1016/j.msea.2019.138340

3. C.D. Rabadia, Y.J. Liu, L.Y. Chen, **S.F. Jawed,** L.Q. Wang, H. Sun, L.C. Zhang, Deformation and strength characteristics of Laves phases in titanium alloys, Materials &

Design 179 (2019) 107891. https://doi.org/10.1016/j.matdes.2019.107891.

4. C.D. Rabadia, Y.J. Liu, **S.F. Jawed**, L. Wang, Y.H. Li, X.H. Zhang, T.B. Sercombe, H. Sun, L.C. Zhang, Improved deformation behavior in Ti-Zr-Fe-Mn alloys comprising the C14 type Laves and β phases, Mater. Des. 160 (2018) 1059-1070. https://doi.org/10.1016/j.matdes.2018.10.049

Table of Contents

Page deliberately left blank

List of Abbreviations

316 stainless steel	316SS
Cobalt-chromium	Co-Cr
Titanium	Ti
Alpha	α
Beta	β
Molybdenum equivalency	Mo_{eq}
Bond order	*Bo*
d-orbital energy level	*Md*
valence atom to electron ratio	*e/a*
Bonding force	*BF*
Atomic radius difference	Δr
Commercially pure Ti	CP-Ti
Ti-6Al-4V	Ti64
Cold crucible levitation melting	CCLM
X-ray diffraction	XRD
Scanning electron microscope	SEM
Energy dispersive x-ray	EDX
Open circuit potential	OCP
Electrochemical impedance spectroscopy	EIS
Corrosion potential	E_{corr}
Corrosion current density	i_{corr}
Hexagonal closed-pack	hcp
Body-centered cubic	bcc
Face-centered cubic	fcc
Niobium	Nb
Chromium	Cr
Zirconium	Zr
Manganese	Mn
Tin	Sn
Alpha double prime	α"
Alpha prime	α'
Omega	ω

Lattice parameter	a
Volume fraction	v_f
Yield strength	$\sigma_{0.2}$
Hardness	H
True plastic strain	ε_p
Strain hardening rate	θ
Strain hardening index	n
Superelastic recovery ration	η
Back scattered electron	BSE
Stress induced martensite transformation	SIMT
Strengthening coefficient	K
Stress for inducing martensite	σ_{SIM}
Ti-25Nb-8Zr-xCr	TNZx
Ti-25Nb-8Zr	TNZ0
Ti-25Nb-8Zr-2Cr	TNZ2
Ti-25Nb-8Zr-4Cr	TNZ4
Ti-25Nb-8Zr-6Cr	TNZ6
Ti-25Nb-8Zr-8Cr	TNZ8
Ti-25Nb-xSn-yCr	TNxy
Ti-25Nb-1Sn-2Cr	TN12
Ti-25Nb-3Sn-2Cr	TN32
Ti-25Nb-5Sn-2Cr	TN52
Ti-25Nb-1Sn-4Cr	TN14
Ti-25Nb-3Sn-4Cr	TN34
Ti-25Nb-5Sn-4Cr	TN54
Ti-26Nb-xZr-yMn	TNZM
Ti-26Nb-4Zr-3Mn	T43
Ti-26Nb-7Zr-3Mn	T73
Ti-26Nb-10Zr-3Mn	T103
Ti-26Nb-4Zr-5Mn	T45
Ti-26Nb-7Zr-5Mn	T75
Ti-26Nb-10Zr-5Mn	T105
Ti-25Nb-xMn-ySn	Ti25xy
Ti-25Nb-2Mn-1Sn	Ti2521

Ti-25Nb-2Mn-5Sn	Ti2525
Ti-25Nb-4Mn-1Sn	Ti2541
Ti-25Nb-4Mn-5Sn	Ti2545

Page deliberately left blank

List of Figures

List of Tables

The following chapters are not included in this version of the thesis:

1. **Introduction and research significance**
2. **Literature review**
3. **Research problems and applied approaches**
4. **Methods and materials**

5. Beta-type Ti-Nb-Zr-Cr alloys with large plasticity and significant strain hardening

This work has been published in the "*Materials & Design*" journal.

5.1. Rationale theoretical design for the novel Ti alloys

The Ti-25Nb-8Zr-xCr (TNZx) alloys were theoretically designed on the basis of approach established by Morinaga et al. [163] known as DV-Xα cluster strategy which is widely used to predict β phase stability and deformation mechanism for the designed Ti alloys based on the two electronic parameters [164] i.e. the bond order (Bo) and the d-orbital energy level (Md) [63]. Bo represents the overlap population between the atomic orbitals of parent element and alloying elements [160]. The overlap population is in proportional relationship with covalent bond strength between a parent element and other alloying elements [160]. Whereas, Md correlates the atomic radius and electronegativity of alloying elements [40]. Md remains in proportional relationship with atomic radius of an element, while it remains in inverse relationship with electronegativity of an element [160]. The average values of $\overline{\mathrm{Bo}}$ and $\overline{\mathrm{Md}}$ for the TNZx alloys were evaluated by the respective formulae suggested in Ref. [98]. Additionally, a new semi-empirical approach developed by Wang et al. [18] was used to design novel group of TNZx alloys. This approach was developed on the basis of two parameters, i.e. the valence electron concentration (e/a) and the atomic size difference (Δr). This approach involves plotting of their compositional average on $\overline{\mathrm{e/a}}$-$\overline{\Delta \mathrm{r}}$ diagram [18]. The values of $\overline{\mathrm{e/a}}$ and $\overline{\Delta \mathrm{r}}$ for the TNZx alloys were estimated using the Eqs. (5.1) and (5.2) [18].

$$\overline{\Delta \mathrm{r}} = \sum_{\mathrm{i}}^{\mathrm{n}} \mathrm{c_i}(\mathrm{r_i} - \mathrm{r_{Ti}}) \tag{5.1}$$

$$\overline{\mathrm{e/a}} = \sum_{\mathrm{i}}^{\mathrm{n}} \mathrm{c_i e_i} \tag{5.2}$$

where c_i, r_i and e_i are the atomic fraction, atomic radius and valence electron number of the ith atom, respectively. Moeq is also a significant parameter for theoretically ensuring the β phase stability and estimating various deformation mechanisms. Moeq can be calculated using the equation of Moeq suggested in Ref. [7]. The calculated-values of $\overline{Bo}$, $\overline{Md}$, $\overline{e/a}$, $\overline{\Delta r}$ and Moeq for the TNZx alloys are summarized in Table 5.1.

Table 5.1 The values of $\overline{Bo}$, $\overline{Md}$, $\overline{e/a}$, $\overline{\Delta r}$ (Å) and *Moeq* (wt%) for all the as-cast Ti-25Nb-8Zr-xCr alloys.

Alloys	**Chemical composition (wt%)**	$\overline{Bo}$	$\overline{Md}$	$\overline{e/a}$	$\overline{\Delta r}$	Mo_{eq}
TNZ0	Ti-25Nb-8Zr	2.8521	2.4677	4.25	0.59	6.9
TNZ2	Ti-25Nb-8Zr-2Cr	2.8519	2.4465	4.29	0.29	9.4
TNZ4	Ti-25Nb-8Zr-4Cr	2.8518	2.4252	4.33	-0.01	11.9
TNZ6	Ti-25Nb-8Zr-6Cr	2.8517	2.4038	4.37	-0.31	14.4
TNZ8	Ti-25Nb-8Zr-8Cr	2.8516	2.3824	4.41	-0.61	16.9

5.2. Results and discussion

5.2.1. Microstructure and phase analyses

Fig. 5.1 presents the XRD profiles of the TNZx alloys. The TNZ0 alloy comprises the orthorhombic α" and bcc β phases, whereas the Cr-containing alloys, i.e. TNZ2, TNZ4, TNZ6 and TNZ8, contain only bcc β phase. The diffraction peaks of bcc Cr-containing Ti alloys shift towards higher 2θ angles upon increasing the Cr content. This is evident due to smaller atomic radius of Cr as compared to Ti [15]. The calculated a_β values for TNZ0, TNZ2, TNZ4, TNZ6 and TNZ8 are found to be 0.3307, 0.3293, 0.3283, 0.3274 and 0.3264 nm respectively. The a_β of bcc Ti alloys comprising Cr reduces as content of Cr increases in the as-cast alloys because the atomic radius of Cr is smaller than Ti [15]. The a_β of TNZ0 alloy is 0.3307 nm which is slightly higher than that of standard bcc Ti (0.3306 nm) due to presence of Zr as it has higher atomic radius as compared to Ti [203, 204]. The orthorhombic α" is found in the TNZ0 alloys because of martensitic transformation which occurs after rapid quenching [205, 206]. The cooling rate plays a significant role in phase transformation from β → α" phase when alloys solidify from high temperature [207]. It was widely reported that, after rapid quenching of Ti alloys, β phase may transform into different phases, i.e. α", α', α and ω phases [120, 207]. It can be noticed that only bcc β peaks are evident on the XRD profiles of the as-cast Cr-containing alloys. It is well known that Cr is a strong β stabilizer [40, 208] and therefore, it substantially enhances the β stability by adding only 2% of Cr in the TNZx alloys. It was reported that the existence of ω phase (Space group: P6/mmm, PDF card no: 00-051-0631) can be detected by XRD at low scanning speed of 0.5 °/min [145, 174]. Accordingly, the XRD curves of the TNZx alloys acquired at slow scan speed of 0.011 °/s with a step size of 0.013 ° in this work, which

could also detect the ω phase if it exists in the studied alloys. According to PDF card no: 00-051-0631, ω phase is associated with the XRD peaks having hkl = 001, 111, 002, 112. In the present work, none of the aforementioned XRD peaks are found for the investigated alloys. Therefore, ω phase is not expected or has trace amount in all the investigated TNZx alloys.

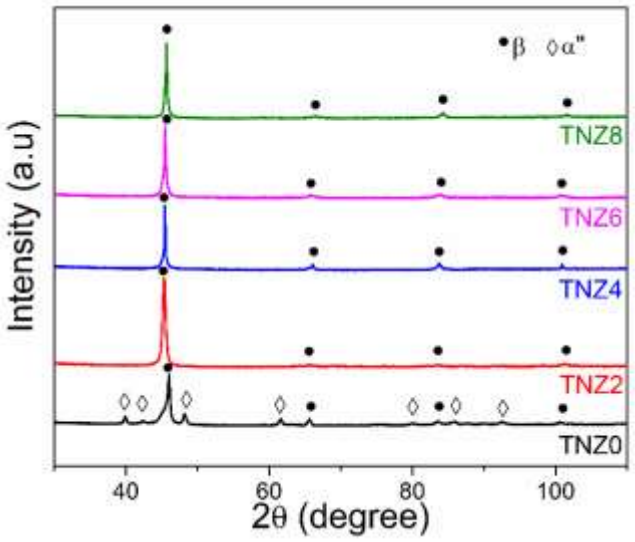

Fig. 5.1. The XRD patterns of the Ti-25Nb-8Zr-xCr alloys (the alloys are shortened as TNZx).

The microstructure images of the TNZx alloys are shown in Fig. 5.2. Only the TNZ0 represents the two phases, i.e. bcc β and orthorhombic α" phases, whereas the Cr-containing TNZx alloys, i.e. TNZ2, TNZ4, TNZ6 and TNZ8 predominantly constitute the full β phase. Therefore, β is a leading phase in the microstructures of all the TNZx alloys. Moreover, an equiaxed structure of the bcc β phase can be clearly observed with the β grain boundaries in the SEM images of all the TNZx alloys. Further, the dendritic substructure, which usually occurs during solidification [209], can also be visible inside the β equiaxed grains in all the studied alloys. It can be noted that, the two kind of contrast happen in Fig. 5.2b-e for TNZ2, TNZ4, TNZ6 and TNZ8 respectively due to dendritic sub-structure which is present inside the β grains. By contrast, in Fig. 5.2a, needles of α" phase are also evident in the microstructure along with the contrast effect produced by dendritic sub-structure of the β grains. The evident peaks related to α" phase are also found in the XRD profile of TNZ0. A high-magnification BSE inset image has been placed in Fig. 5.2 to clearly show the acicular structure of α" phase. Based on the results of microstructure and phase characterization, TNZ0 contains dual phase, i.e. β and α" phases, while the remaining alloys (TNZ2, TNZ4, TNZ6 and TNZ8) contain single β phase. Moreover, EDX mapping results (not shown herein) show that the Cr has homogeneously distributed in the alloys for all the investigated alloys.

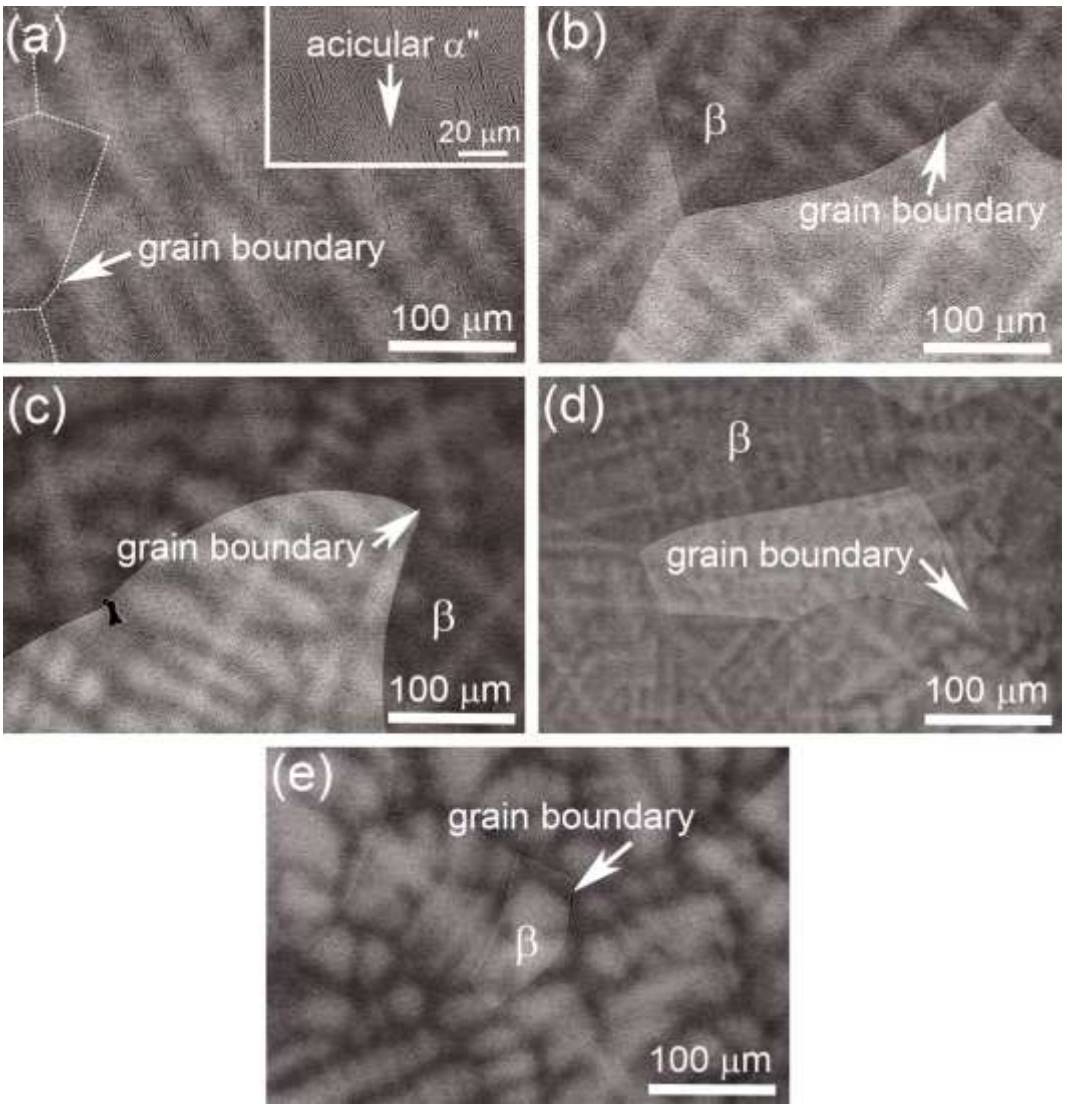

Fig. 5.2. The backscattered SEM microstructure images of the Ti-25Nb-8Zr-xCr alloys: (a) 0 wt%, (b) 2 wt%, (c) 4 wt%, (d) 6 wt% and (e) 8 wt%.

5.2.2. Mechanical properties

It is known that the microstructural characteristics and their corresponding V_f constitutes in Ti alloys influence their mechanical properties [120, 196]. Therefore, to investigate the influence of different compositions on the mechanical performance of the designed Ti alloys, compression testing at room temperature and Vickers micro-hardness tests were conducted.

Fig. 5.3 demonstrates the compressive engineering stress-strain curves taken for the TNZx alloys at room temperature. The stopping criterion for the compressive tests was either the alloy failed or when the compression testing machine reached 100 kN (the load capacity of the mechanical machine). It can be noticed from Fig. 5.3 that all the studied TNZx alloys except for the TNZ0 exhibit very large plastic strain and do not fail until the 100 kN is reached. Note that, the addition of Cr significantly enhances the mechanical properties (strength and plasticity) of

the TNZx alloys. Fig. 5.3 inset shows the difference in specimen-size before and after compression testing for TNZ8. A small shear crack (after the compression test) on the specimen-surface of TNZ8 can also be seen in Fig. 5.3 inset because the definite fracture has not occurred in any Cr-containing TNZx alloys, until the load reaches 100 kN in compression testing.

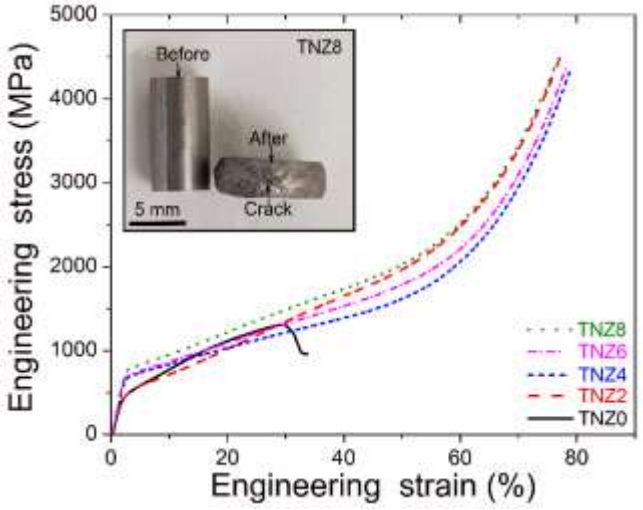

Fig. 5.3. The ambient temperature engineering stress-strain curves of the Ti-25Nb-8Zr-xCr alloys (the alloys are shortened as TNZx).

Fig. 5.4 shows the relationship between yield strength ($\sigma_{0.2}$) and Hardness (H) of the TNZx alloys. In this work, both $\sigma_{0.2}$ and H change in a same fashion as both have a proportional relationship with each other [40, 210, 211]. It is clear from Fig. 5.4 that the values of $\sigma_{0.2}$ and H increase gradually with increasing the Cr content in the studied alloys. The values of $\sigma_{0.2}$ for the Cr-containing alloys vary from 385 $\pm$ 44 MPa to 773 $\pm$ 28 MPa. Further, the values of H for the Cr-containing alloys vary from 1.94 $\pm$ 0.05 GPa to 2.63 $\pm$ 0.06 GPa. Such an increasing trend of $\sigma_{0.2}$ and H for the TNZx alloys is positively influenced by the effect of solid-solution strengthening [42]. The phenomenon of solid-solution strengthening occurs as per the well-known Hume-Rothery rule due to adding low atomic radius (solute) element, i.e. Cr, in the alloys [15].

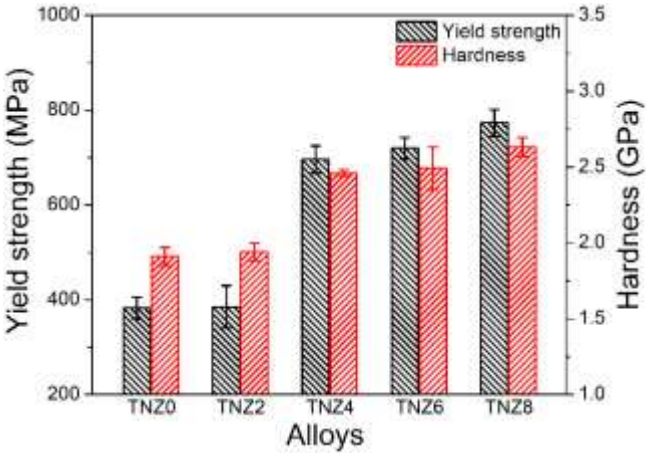

Fig. 5.4. Yield strength ($\sigma_{0.2}$) and hardness (H) of the Ti-25Nb-8Zr-xCr alloys (name of the alloys are shortened as TNZx).

It is of worth noting from Fig. 5.5 that the addition of Cr significantly enhances the plastic strain and maximum compressive strength obtained at 100 kN for all the studied alloys. Among the investigated alloys, TNZ0 exhibits the lowest plastic strain (28 ± 0.5%) as it consists of α" phase along with β phase. Whereas, all the Cr-containing alloys display superior plastic strain (~75%) and maximum compressive strength (~4.5 GPa) at 100 kN, because the Cr has enhanced the β phase stability and thus suppresses the α". Accordingly the mechanical properties (both strength and plasticity) of all the investigated Cr-containing TNZx alloys are significantly enhanced [120]. In the present work, the mechanical properties are influenced by the addition of Cr. Moreover, all the investigated alloys show equiaxed β grains and the size of the β grains decrease as the content of Cr increases in the TNZx alloys. However, it is difficult to measure the accurate average size of the β grains as the size of the β grains is greater than around 300-500 μm in all the investigated alloys. It can be inferred based on the points discussed above that the mechanical properties are mainly affected due to the content of solute element (i.e. Cr) instead of the minimum differences in dendritic structures of the investigated alloys.

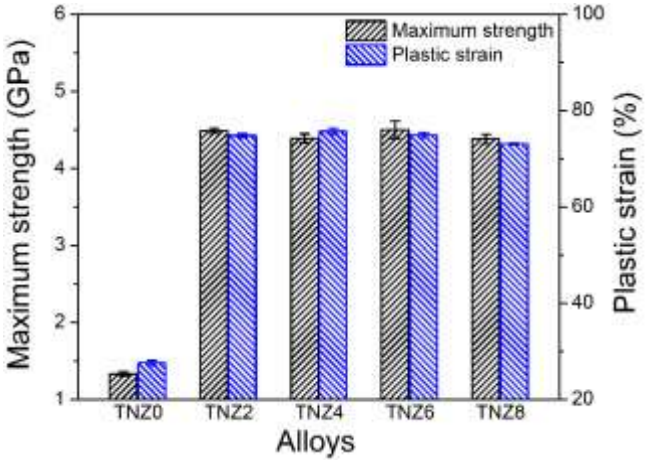

Fig. 5.5. Maximum strength (σ_{max}) and plastic strain (e_p) of the Ti-25Nb-8Zr-xCr alloys (the alloys are shortened as TNZx).

Fig. 5.6 presents the compressive true stress-strain curves obtained at room temperature for the TNZx alloys. It can be observed from Fig. 5.6 that the true stress-strain curves comprise multiple peaks of stress oscillations and these curves include four stages: (I) elastic stage, (II) first strain hardening stage, (III) strain softening stage and (IV) second strain hardening stage as presented in Fig. 5.6 inset only for TNZ4 as an example to show the four stages. Such kind of multiple-peak oscillations have also been reported in the previous work on Ti-Nb-Ta-Zr-O alloy during straining [212]. The first strain hardening stage occurs based on the dynamic Hall-Petch effect, which shows that α" martensite and twinning deformation produce new sharp interfaces due to continuous sub-grain division. These interfaces would also restrict the dislocation motion and minimize the dislocation mean free path, thereby causing increased rate of strain hardening [213, 214]. The strain softening is produced due to the effect of stress relaxation in which stress intensity reduces when the specimen is loaded for quite long period of time at constant strain rate [215]. Second strain hardening stage occurs due to the formation of shear bands [212, 216]. As such, at the end of compression test, a high intensity of shear stress remains in the specimen and the deformation mechanism alters into the formation of shear bands [212].

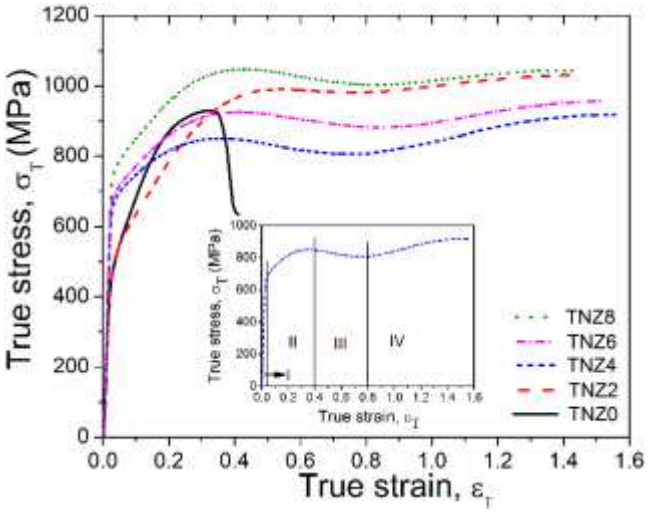

Fig. 5.6. The true stress-strain curves of the Ti-25Nb-8Zr-xCr alloys (the alloys are shortened as TNZx). Inset shows the four stages in deformation.

Fig. 5.7 illustrates the relationship between strain hardening rate (θ) and true plastic strain (ε_p) for the TNZx alloys. The inset presented in Fig. 5.7 is for TNZ4 only as an example to show the variation in θ. The $\partial\sigma_T/\partial\varepsilon_p$ for TNZx alloys containing Cr comprises, the first strain hardening stage (before point A), the strain softening stage (between points A and B) and the second strain hardening stage (after point B). It is clear from inset Fig. 5.7 that $\partial\sigma_T/\partial\varepsilon_p < 0$ during strain softening stage, $\partial\sigma_T/\partial\varepsilon_p > 0$ during strain hardening stages and $\partial\sigma_T/\partial\varepsilon_p \approx 0$ at points A and B. Notably, the θ increases by adding 2 wt% Cr in the TNZ0 alloy (i.e. the TNZ2 alloy) (5 GPa) during first stage of strain hardening. This occurs due to the activation of twin deformation mechanism [176, 217, 218]. The second strain hardening stage occurs due to the formation of shear bands. Therefore, TNZ4 demonstrates the highest rate of strain hardening (0.65 GPa) in the second stage among the investigated TNZx alloys because the highest plasticity is also found in TNZ4 among all the studied alloys [212].

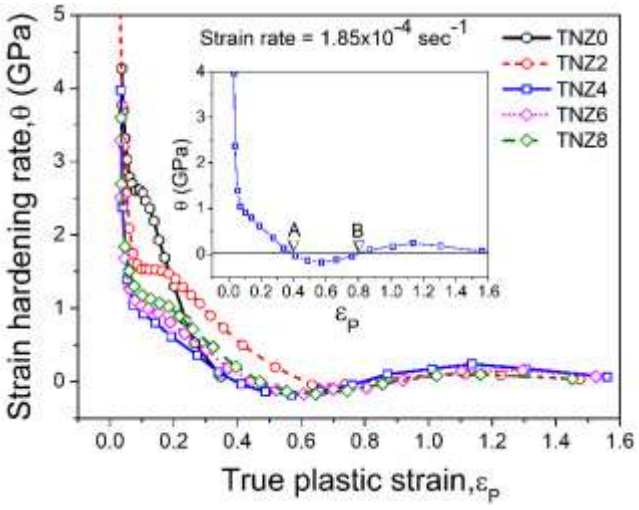

Fig. 5.7. The strain hardening rate as a function of true plastic strain of the Ti-25Nb-8Zr-xCr alloys (the alloys are shortened as TNZx). Inset shows the variation in strain hardening stages.

5.2.3. The elasto-plastic deformation

The elasto-plastic deformation behavior can be analyzed effectively by studying the deformation patterns around the Vickers indentation [218]. Typically, there are three forms of morphologies formed around micro-hardness indentations of an alloy (i.e. “Sink-in”, “pile-up” and “crack”) [210]. The formation of deformation bands, extrusion and cracks may occur during hardness testing around the impression of an indenter [210]. While performing indentation in hardness testing, the deformation of material around the edge of an indenter takes place due to both the shear and normal stress components, whereas the deformation around the corners emerges because of normal stress components only which remains the cause of crack formation [210]. The wavy and straight morphologies of deformation bands around the hardness indentation can be used to determine the boundaries between slip and twin mechanism in $\overline{Bo}$-$\overline{Md}$ map [160]. Wavy slip bands form around indentation when slip mechanism is dominant and straight twin bands form around indentation when twin mechanism dominates the deformation of a material [160].

Fig. 5.8 displays the optical micrographs which were captured around the micro-hardness indentations of the TNZx alloys. No crack morphology is found on the corners of an indenter for all the investigated alloys as all show significant plasticity in compressive testing as shown in Fig. 5.6. Hence, few deformation bands are obtained around the hardness indentation for TNZ0 (Fig. 5.8a), because it has the lowest plastic deformation strain among the investigated alloys. A substantial increase in the number of bands can be clearly observed from Fig. 5.8b after addition of 2 wt% Cr in the TNZ0 alloy. As such, the morphology of the bands around the

indentations of TNZ2 is straight twin, which represents that twin mechanism is dominant in the deformation of TNZ2 alloy [160]. In Fig. 5.8c, more wavy slip bands are observed along with a few straight twin bands, which represents the activation of twin + slip deformation mechanism in the TNZ4 alloy [160]. It can be clearly seen from Fig. 5.8d-e that only wavy slip bands are formed around the indentations, which indicates that slip mechanism is dominant in the defamation of both TNZ6 and TNZ8 alloys [160].

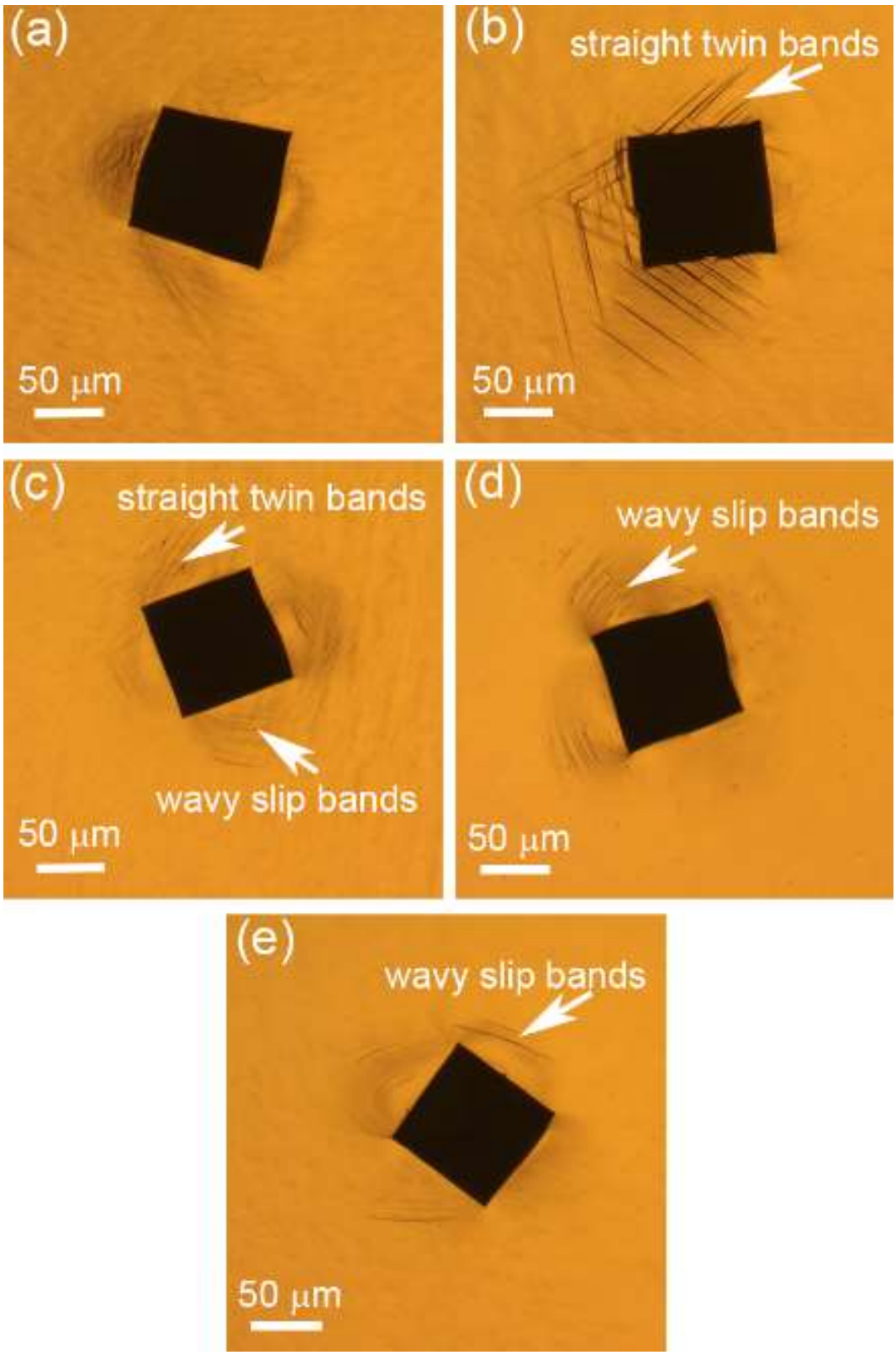

Fig. 5.8. The optical micrographs around the Vickers micro-hardness indentations captured for the Ti-25Nb-8Zr-xCr alloys (the alloys are shortened as TNZx): (a) TNZ0, (b) TNZ2, (c) TNZ4, (d) TNZ6 and (e) TNZ8.

Fig. 5.9 and Fig. 5.10 shows the boundaries between different deformation mechanisms of the TNZx alloys. In Fig. 5.9, the regions of α, α+β and β phases and their possible deformation

mechanisms (i.e. slip and twin) can be clearly seen. The phase stability in $\overline{Bo}$-$\overline{Md}$ map can be observed by plotting the $\overline{Bo}$ and $\overline{Md}$ values of the TNZx alloys in the $\overline{Bo}$-$\overline{Md}$ map as suggested by Ref. [19]. It is reported that alloy should have high $\overline{Bo}$ and low $\overline{Md}$ values to attain a high β stability position in the $\overline{Bo}$-$\overline{Md}$ map [40]. The locations of all the studied alloys, on the basis of their respective $\overline{Bo}$ and $\overline{Md}$ values presented in Table 5.1 are plotted in the $\overline{Bo}$-$\overline{Md}$ map. It is clearly observed from Fig. 5.9 that TNZ0 is located in the martensite region, TNZ2 is placed in the twin region, TNZ4 is almost on the boundary of slip/twin, while the rest alloys (i.e. TNZ6 and TNZ8) are located in the slip region. Deformation mechanisms can also be estimated by plotting the $\overline{e/a}$ and $\overline{\Delta r}$ values of the studied alloys in $\overline{e/a}$-$\overline{\Delta r}$ diagram as suggested by Ref. [18].

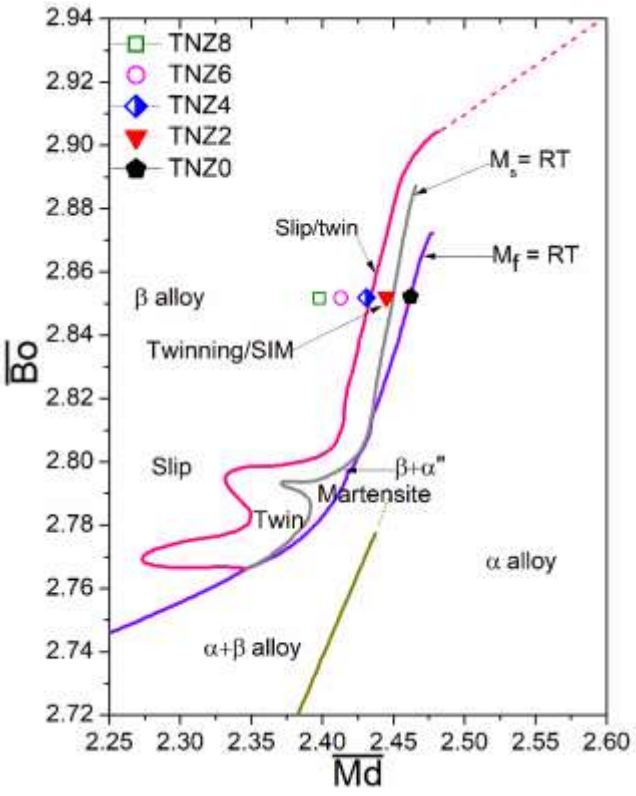

Fig. 5.9. The locations of the Ti-25Nb-8Zr-xCr alloys (the alloys are shortened as TNZx) on the phase stability diagram.

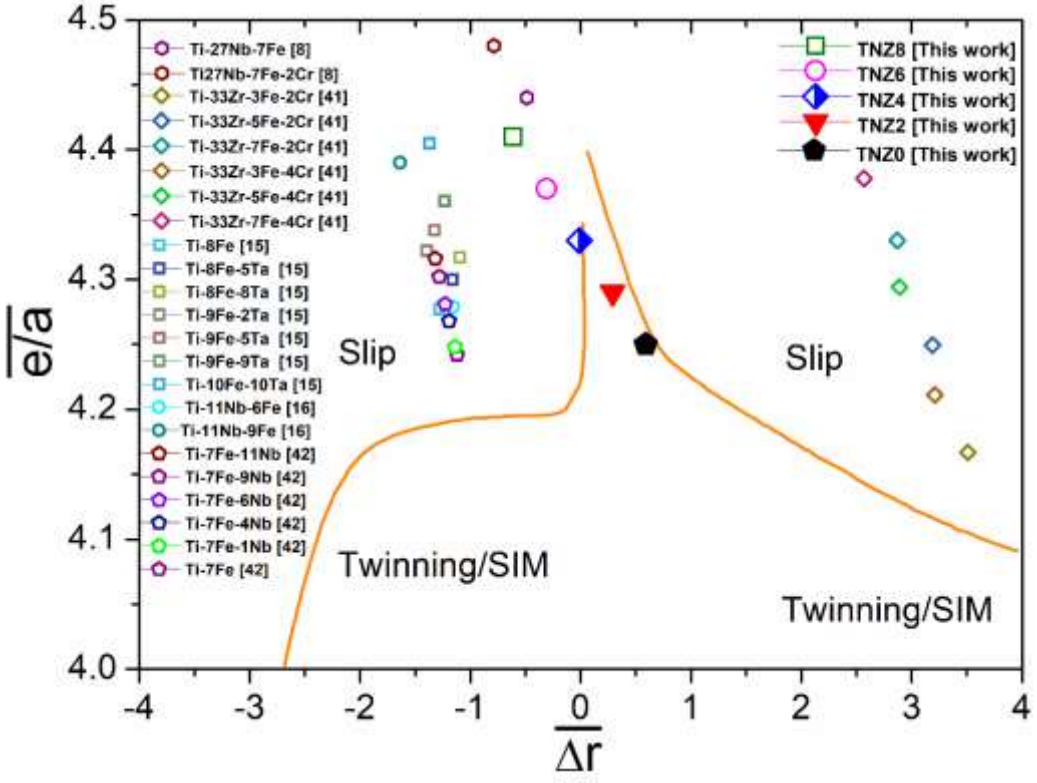

Fig. 5.10. The locations of the Ti-25Nb-8Zr-xCr alloys (name of the alloys are shortened as TNZx) on the $\overline{e/a}$-$\overline{\Delta r}$ diagram. The orange lines in this diagram are plotted based on Ref. [18].

In this work, the values of $\overline{e/a}$ and $\overline{\Delta r}$ (Table 5.1) for all the TNZx alloys and some other studied Ti alloys in literature are plotted in Fig. 5.10 in order to investigate the deformation mechanism through $\overline{e/a}$-$\overline{\Delta r}$ diagram. All the plotted alloys are in good agreement with the predicted deformation mechanisms as suggested by $\overline{e/a}$-$\overline{\Delta r}$ diagram. Fig. 5.10 predicts the twin or SIM mechanism for TNZ2 and TNZ0, slip + twin mechanism for TNZ4 and slip mechanism for TNZ6 and TNZ8. Furthermore, Kolli et al. [16] studied the influence of the values of Mo_{eq} on the various deformation mechanisms for Ti alloys and found that the deformation mechanisms change in the sequence of α' → α" → ω + twinning → twinning + Slip → Slip as increasing the values of Mo_{eq} [16]. The values of Mo_{eq} for the studied TNZx alloys (as shown in

Table 5.1) suggest the similar trend as suggested by Ref. [16]. As a result, the deformation mechanisms predicted by the $\overline{Bo}$-$\overline{Md}$ diagram and $\overline{e/a}$-$\overline{\Delta r}$ diagram are in good agreement with that by morphologies of deformation bands around the micro-hardness indentations for the studied TNZx alloys.

5.2.4. Fracture analyses

It is known that shear bands are the localization of high shear strains which cause the

occurrence of deformation bands along the direction of maximum shear stress [219]. Prior to the formation of shear bands, a material typically experiences a yielding and deformation twinning during the plastic deformation [220]. Thus, analyses of shear bands were performed on the samples prepared metallographically for the investigated Cr-containing Ti alloys at the same load limit (at 100 kN). The features of these analyses are presented in Fig. 5.11. TNZ0 is not included in this analysis as the TNZ0 fails before reaching the 100 kN in compression testing. Hence, for analyzing the shear bands at the same load limit, the compression tests were stopped at 100 kN in the present work. Shear bands can be clearly noticed in Fig. 5.11a-d. In Fig. 5.11b, thick shear bands can be observed in TNZ4, which indicates that a large plastic deformation occur in TNZ4 alloy and as a consequence TNZ4 relatively displays the largest plastic strain [15, 221].

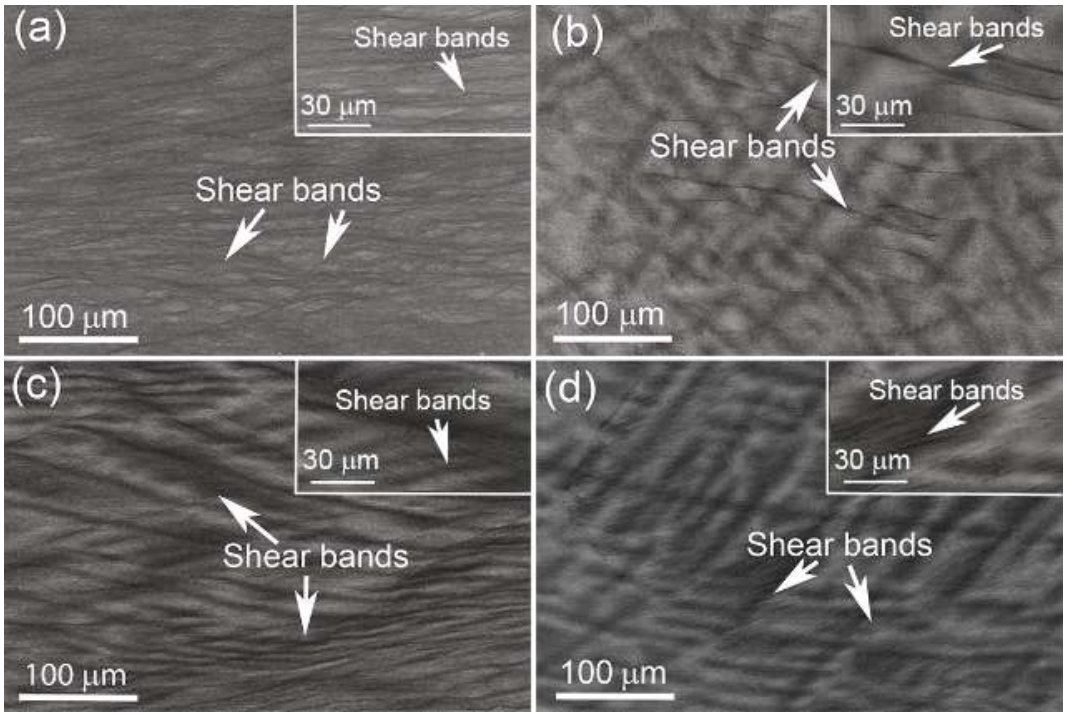

Fig. 5.11. Backscattered SEM images of mechanically deformed surface morphologies of the Ti-25Nb-8Zr-xCr alloys containing Cr: (a) TNZ2, (b) TNZ4, (c) TNZ6 and (d) TNZ8.

Fig. 5.12 shows the SEM images of fractographic morphologies captured on the deformed-outer surfaces of the tested specimens for the investigated TNZx alloys. The shear crack angle between the fracture plane and compressive loading direction is almost 45 °which indicates that cracks form in a shear mode [139]. There is a minor shear crack on the outer surfaces of the Cr-containing alloys. Fig. 5.12 shows the SEM fractographic images for the deformed Cr-containing TNZx alloys together with TNZ0. Fig. 5.12a displays the flat main fracture in TNZ0

which demonstrates a transgranular fracture. Further, the cracks can be observed on the fractographic image of TNZ0. On the other hand, Fig. 5.12b-e displays that fracture is not observed in the deformed samples of all the investigated Cr-containing TNZx alloys since these alloys do not fail in mechanical compression testing. Nonetheless, many shear bands are observed in all the deformed Cr-containing TNZx alloys. Therefore, all of the investigated Cr-containing TNZx alloys possess a significantly large plasticity. The fractographic results are in line with the studied mechanical properties of TNZx alloys.

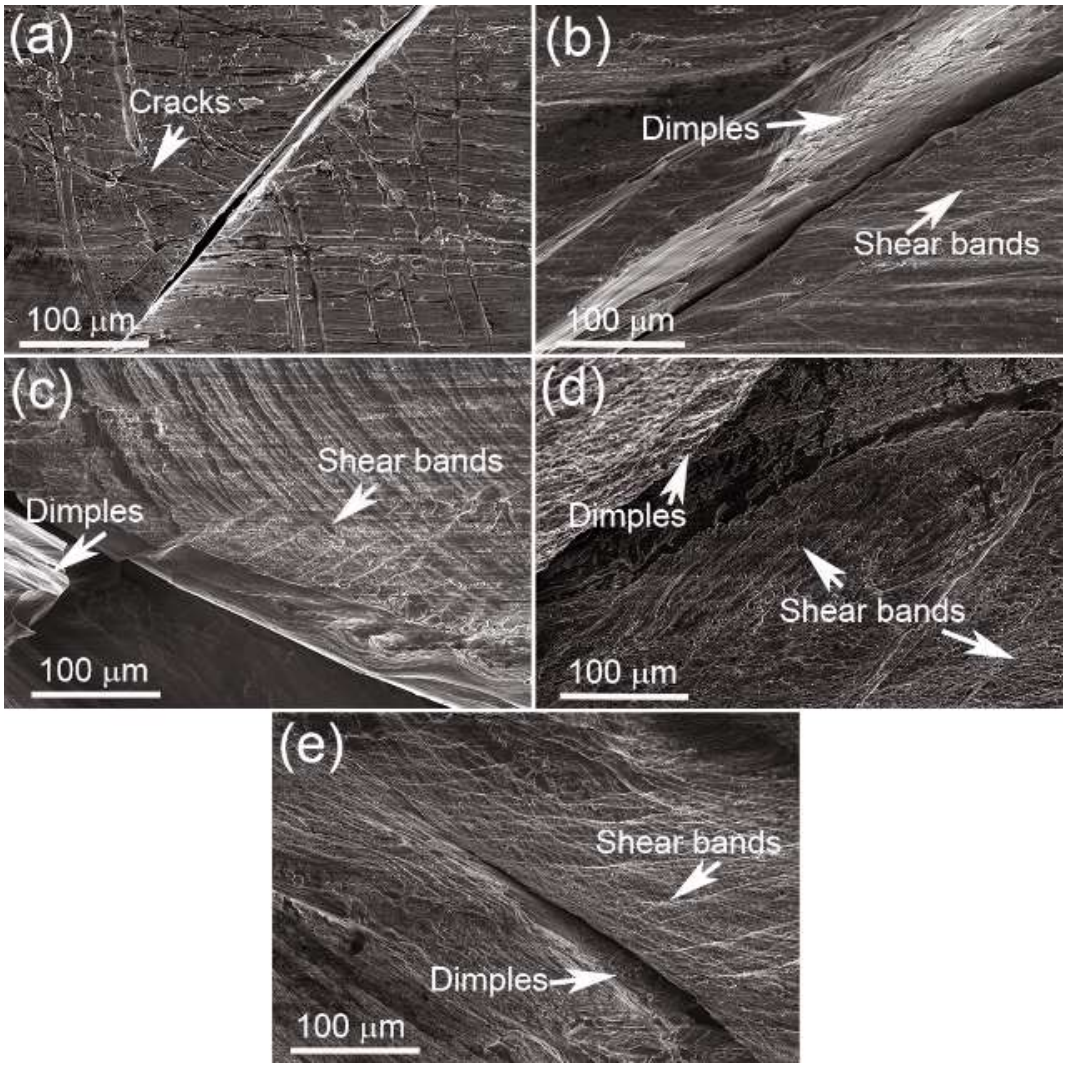

Fig. 5.12. SEM fracture surface morphologies of the Ti-25Nb-8Zr-xCr alloys: (a) TNZ0, (b) TNZ2, (c) TNZ4, (d) TNZ6 and (e) TNZ8.

5.3. Conclusions

The present work investigates the microstructural characteristics, the mechanical properties, the elasto-plastic deformation and deformation behaviors for the newly-designed Ti-25Nb-8Zr-xCr (x = 0, 2, 4, 6, 8 wt%) alloys, which were designed based on DV-Xα cluster method and $\overline{e/a}$-

$\overline{\Delta r}$ diagram. The following concluding remarks can be made from the results presented.

- The Ti-25Nb-8Zr alloy displays a dual-phase (bcc β and orthorhombic α" phases) microstructure while the Cr-containing Ti-25Nb-8Zr-xCr alloys predominantly comprise a single bcc β phase in microstructure.
- All the Cr-containing alloys do not fail in the compression tests performed up to the load capacity at 100 kN. All the Cr-containing alloys exhibit impressive maximum compressive strength (~4.5 GPa) and superior plastic strain (~75%). Both hardness (1.91 GPa to 2.63 GPa) and yield strength (382 MPa to 773 MPa) increase as the Cr concentration increases in the Ti-25Nb-8Zr-xCr alloys. Enhanced strain hardening rate (5 GPa) is achieved in Ti-25Nb-8Zr-2Cr alloy.
- The predicted deformation mechanisms based on deformation bands investigated around micro-hardness indentations, $\overline{Bo}$-$\overline{Md}$ diagram and $\overline{e/a}$-$\overline{\Delta r}$ diagram are in line with each other for the investigated Ti-25Nb-8Zr-xCr alloys. Moreover, the results of the fracture analyses and the mechanical properties for the investigated alloys are also in good agreement with each other.
- Among all the as-cast alloys, the Ti-25Nb-8Zr-2Cr and Ti-25Nb-8Zr-4Cr alloys exhibit significant strain hardening and superior plasticity. Both alloys can be potentially used in advanced biomedical and structural applications.

The following chapter is not included in this version of the thesis:

6. Mechanical characterization and deformation behaviour of β-stabilized Ti-Nb-Sn-Cr alloys

Page deliberately left blank

7. Strengthening mechanism and corrosion resistance of beta-type Ti-Nb-Zr-Mn alloys

This work has been published in the "*Material Science and Engineering: C*" journal.

7.1. Material design

The Ti-26Nb-xZr-yMn (TNZM) alloys and their elemental concentrations were theoretically designed using DV-Xα cluster design strategy. The mean values of bond order ($\overline{Bo}$) and metal *d*-orbital energy level ($\overline{Md}$) for the designed alloys are shown in Table 7.1 The $\overline{Bo}$ and $\overline{Md}$ values were designed with an objective to achieve the fully stabilized β phase based on the phase stability map suggested by Abdel-Hady et al. [19].

Table 7.1. The values of mean bond order ($\overline{Bo}$) and mean metal d-orbital energy level ($\overline{Md}$), and the lattice parameter (a) of β phase (a_β) estimated from XRD patterns in as-cast (a_β) and after compression testing (a_β*) and the mean grain size (D) estimated by ImageJ for all the Ti-26 wt% Nb-(4, 7, 10) wt% Zr-(3, 5) wt% Mn alloys.

Alloys	Chemical composition (wt%)	$\overline{Bo}$	$\overline{Md}$	a_β (nm)	a_β*(nm)	D (μm)
T43	Ti-26Nb-4Zr-3Mn	2.8438	2.4169	0.3275	0.3278	203 ± 32
T73	Ti-26Nb-7Zr-3Mn	2.8503	2.4255	0.3277	0.3281	245 ± 50
T103	Ti-26Nb-10Zr-3Mn	2.8570	2.4345	0.3279	0.3284	315 ± 54
T45	Ti-26Nb-4Zr-5Mn	2.8426	2.391	0.3269	0.3274	122 ± 27
T75	Ti-26Nb-7Zr-5Mn	2.8491	2.3993	0.3271	0.3277	183 ± 29
T105	Ti-26Nb-10Zr-5Mn	2.8558	2.4078	0.3276	0.3280	244 ± 45

7.2. Results and discussion

7.2.1. Phase and microstructure characterizations

Fig. 7.1 shows the XRD profiles of all the TNZM alloys. All the TNZM alloys show the peaks related to body-centered cubic (bcc) β phase (PDF card no.: 00-044-1288 and 01-071-9942). The diffraction peaks slightly shift towards a higher 2θ angle when augmenting the amount of Mn in the TNZM alloys. This phenomenon occurs because of the addition of Mn which possesses the smaller atomic radius than Ti. Furthermore, the a of bcc β phase (a_β) in as-cast condition for the TNZM alloys are presented in Table 7.1. The decreasing trend of a_β is apparent while increasing the amount of Mn in the TNZM alloys. The decreasing trend in the values of a_β occurs due to replacing Ti by Mn comprising smaller atomic radius than Ti [42].

Whereas, the increasing trend in the values of a_β can be observed by increasing the amount of Zr in the TNZM alloys because Zr has a larger atomic radius compared to Ti [233]. In this work, the XRD profile of each alloy was acquired at slow scan speed of 0.011 °/s and a step size of 0.013 °. In XRD profiles of the investigated alloys, the peaks associated with miller indices 001, 111, 002, 112 of ω phase are not detected with Co-kα radiation source (Space group: P6/mmm, PDF card no: 00-051-0631) [152]. Therefore, ω phase is not expected in all the TNZM alloys.

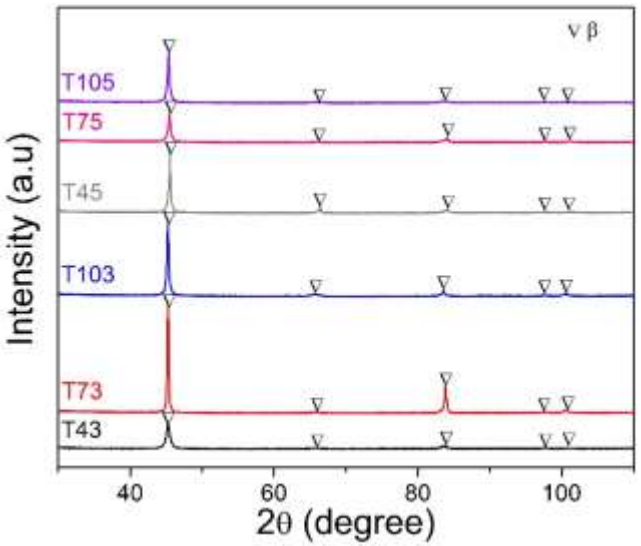

Fig. 7.1. XRD profiles of the Ti-26Nb-xZr-yMn (x = 4, 7, 10 wt% and y = 3, 5 wt%) alloys (The alloys are named in the Txy format).

The microstructural topographies of all the TNZM alloys are presented in Fig. 7.2. The equiaxed bcc β grains with elongated grain boundaries can be observed for all the TNZM alloys. Furthermore, the dendritic substructure is obvious in the β grains of all the TNZM alloys which typically forms during solidification process after casting. The mean grain size for each TNZM alloy estimated using an ImageJ software is shown in Table 7.1 Among the TNZM alloys, the T103 displays the largest mean grain size of 315 ± 54 μm, whereas T54 shows smallest mean grain size of 122 ± 27 μm. It is noted that the mean grain size of the TNZM alloys decreases as the amount of Mn as a solute atom increases. The reduction in grain size of the TNZM alloys occurs due to the addition of Mn. In general, Mn comprises high growth-restriction factor when alloy to Ti and therefore, the addition of Mn in the TNZM alloys leads to a grain refinement [234]. By contrast, grain size increases when increasing the amount of Zr in the TNZM alloys. A similar trend has been reported in the previous studies [42, 235]. The phase and microstructural characterizations indicate that all the TNZM alloys are comprised of

a monolithic β phase. It has been reported in previous studies that the addition of 30 wt% or high quantities of Nb in Ti-Nb binary alloys can result in monolithic β phase [223]. In this work, Mn and Zr are added with 26% of Nb to compensate towards the stabilization of a monolithic β phase in all the TNZM alloys.

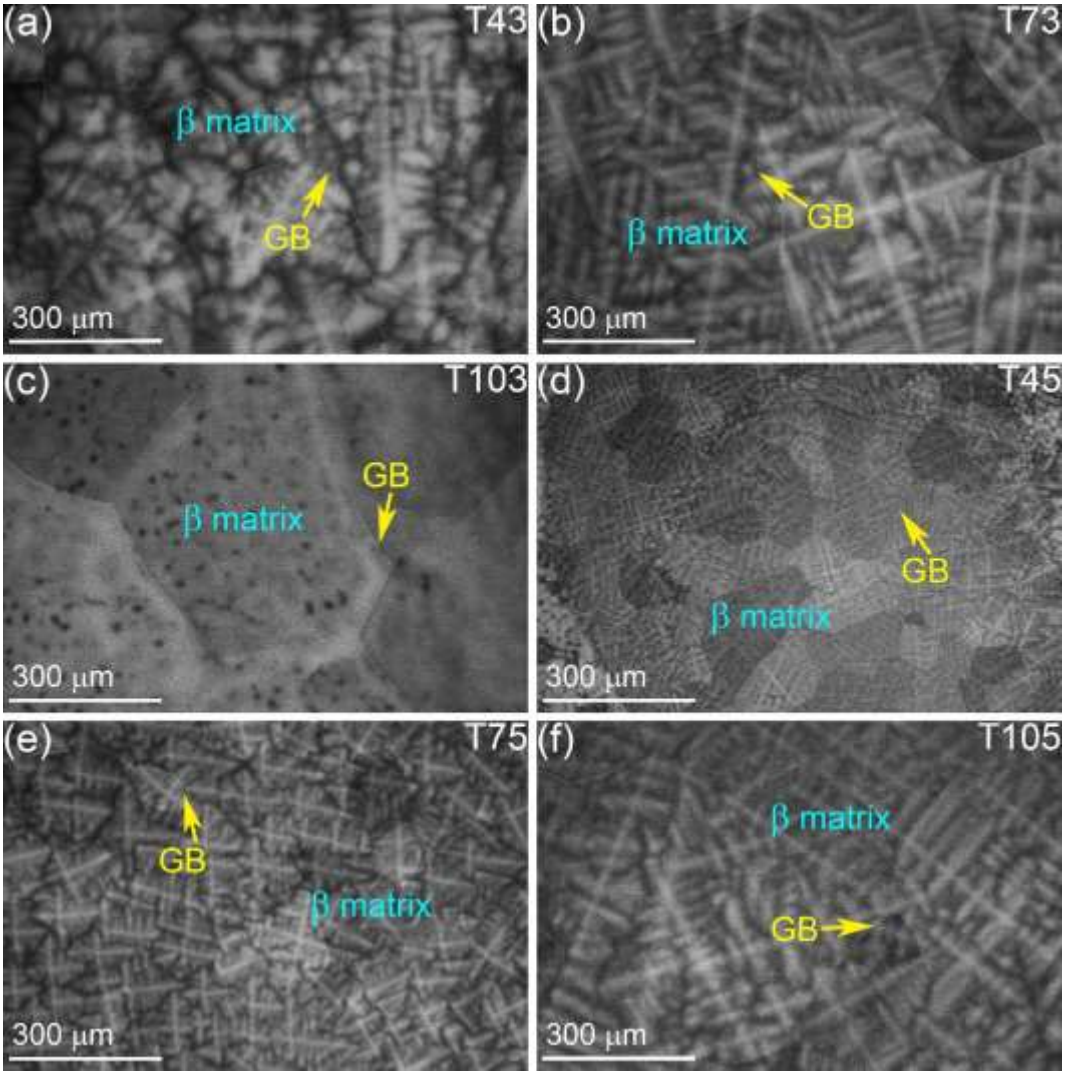

Fig. 7.2. The backscattered SEM microstructural features of the Ti-26Nb-xZr-yMn (x = 4, 7, 10 wt% and y = 3, 5 wt%) alloys (The alloys are named in Txy format). Note that grain boundary is labelled as GB.

7.2.2. Mechanical characterizations

It is well known that the microstructure and phase characterization of an alloy greatly influence their mechanical properties [196, 236]. The newly designed TNZM alloys were subjected to mechanical compression testing in order to demonstrate its rudimentary mechanical characterizations. As a matter of fact, the bones and surrounding hard tissues are primarily subjected to compressive loads; therefore, the compression testing has been carried out in this work [237]. Fig. 7.3a displays compressive engineering stress strain curves for all the TNZM

alloys. Moreover, the properties of true stress-strain curves of polycrystalline materials remain analogous in compression and in tension except the strain to failure propert [201, 238]. Therefore, the compressive true stress-strain curves for all the TNZM alloys have also been presented in Fig. 7.3b. All the TNZM alloys exhibit a significant plastic deformation in mechanical compression testing. The engineering stress-strain curves (Fig. 7.3a) of the TNZM alloys are comprised of mainly three stages, i.e., elastic stage, plateau stage and densification stage [95]. According to Gibson-Ashby's model for compressive stress-strain curves, the unit cell wall bending, the collapse of the unit cell and the continuous load applied to strengthen the completely collapsed unit cells remain responsible for the elastic stage, the plateau stage and the densification stage, respectively [20]. Notably, all the TNZM alloys do not display a fracture during the compression tests within the load capacity of 100 kN. The values of engineering maximum compressive strength and plastic strain presented in Table 7.2 were obtained at 100 kN for all the TNZM alloys. All the TNZM alloys demonstrate engineering plasticity of ~80% and engineering maximum strength of ~5 GPa due to the strong β-phase stability found in all the TNZM alloys [40]. The true stress-strain curves Fig. 7.3b) display significant amount of plasticity and strength within the load capacity of 100 kN. An oscillating effect can be noted in plastic region of true stress-strain curves that shows a softening behavior which occur due to stress relaxation [238]. The values of true maximum strength and plastic strain presented in Table 7.3 were obtained at 100 kN for all the TNZM alloys. All the TNZM alloys display significant true plasticity of ~160% and true maximum strength of ~950 MPa. In general, the instantaneous cross-sectional area of a specimen increases when a material undergoes the deformation in the plastic region during compression testing. Therefore, engineering strain remains lower than true strain and contrastingly, engineering stress remains higher than engineering strain [201, 238]. The analogous behavior can be observed for true strain with engineering strain and true stress with engineering strain values of the TNZM alloys. Moreover, the TNZM alloys display moderate hardness values in the range of 200-250 HV (Table 7.2). The values of hardness increase upon increasing the amount of Mn in the TNZM alloys. By contrast, the value of hardness decreases upon increasing the amount of Zr in the TNZM alloys.

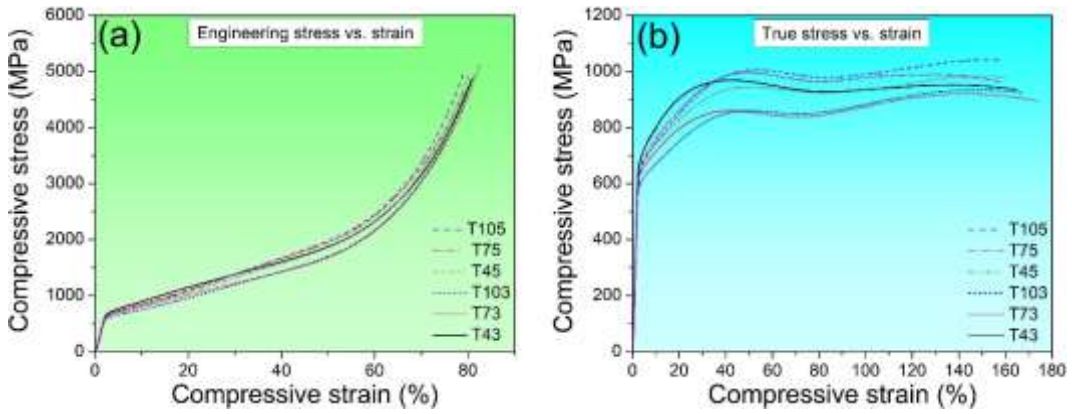

Fig. 7.3. The (a) engineering and (b) true stress-strain curves of the Ti-26Nb-xZr-yMn (x = 4, 7, 10 wt% and y = 3, 5 wt%) alloys (The alloys are named in Txy format).

Table 7.2. The compressive engineering mechanical properties such as yield strength ($\sigma_{0.2}$), plastic strain (ε_p) and maximum strength (σ_{max}) along with hardness (H) obtained for all the Ti-26 wt% Nb-(4, 7, 10) wt% Zr-(3, 5) wt% Mn alloys.

Alloys	**Chemical composition (wt%)**	$\sigma_{0.2}$ **(MPa)**	ε_p **(%)**	σ_{max} **(GPa)**	H **(HV)**
T43	Ti-26Nb-3Mn-4Zr	591 ±18	79.2 ±0.5	4.91 ±0.12	225 ±5
T73	Ti-26Nb-3Mn-7Zr	557 ±6	80.4 ±0.4	5.13 ±0.21	219 ±2
T103	Ti-26Nb-3Mn-10Zr	451 ±19	80.0 ±0.4	4.94 ±0.35	207 ±5
T45	Ti-26Nb-5Mn-4Zr	609 ±18	78.9 ±0.7	4.91 ±0.21	242 ±5
T75	Ti-26Nb-5Mn-7Zr	571 ±3	77.7 ±0.5	4.89 ±0.30	236 ±4
T105	Ti-26Nb-5Mn-10Zr	488 ±19	77.9 ±0.3	4.90 ±0.15	228 ±4

Table 7.3. The compressive true mechanical properties such as plastic strain ($\varepsilon_{p,\ T}$), maximum strength ($\sigma_{max,\ T}$) and strength co-efficient (K) obtained for all the Ti-26 wt% Nb-(4, 7, 10) wt% Zr-(3, 5) wt% Mn alloys.

Alloys	**Chemical composition (wt%)**	$\varepsilon_{p,\ T}$ **(%)**	$\sigma_{max,\ T}$ **(MPa)**	K **(MPa)**
T43	Ti-26Nb-3Mn-4Zr	163 ±2	923 ±54	902 ±18
T73	Ti-26Nb-3Mn-7Zr	166 ±7	935 ±42	889 ±20
T103	Ti-26Nb-3Mn-10Zr	168 ±2	929 ±16	865 ±26
T45	Ti-26Nb-5Mn-4Zr	162 ±3	964 ±39	1000 ±19
T75	Ti-26Nb-5Mn-7Zr	157 ±2	961 ±23	974 ±15
T105	Ti-26Nb-5Mn-10Zr	157 ±2	968 ±23	921 ±24

In order to calculate the dislocation density as well as to confirm the formation of any stress induced martensitic transformation (SIMT) during deformation, the XRD analyses have been carried out on a deformed specimen (after compression testing) of all the TNZM alloys. It is evident in Fig. 7.4 that all the investigated alloys show only a single bcc β-phase even after compression testing and the evidence of peaks related to martensitic phases in the XRD spectra are not found. This suggests that the SIMT does not occur during the deformation of all the

TNZM alloys. The values of a_β* for all the TNZM samples after compression testing presented in Table 7.1 followed a similar trend like a_β, however, the values of a_β* are increased in comparison to the values of a_β due to the lattice distortion that occurs when a material undergoes a compression testing or a rolling operation [201, 239].

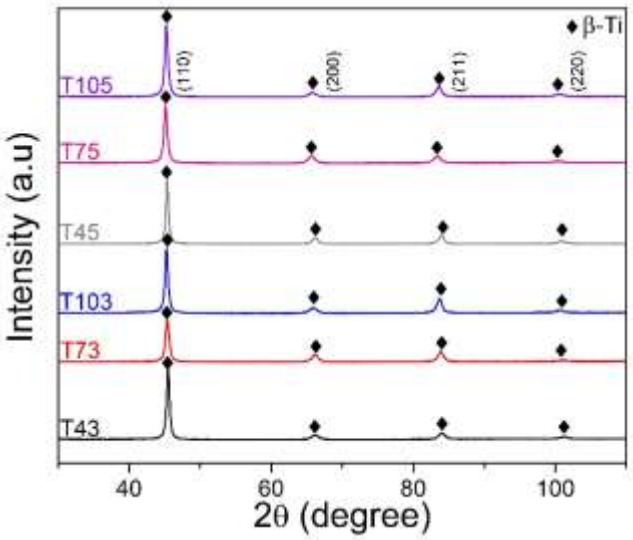

Fig. 7.4. XRD spectra of the Ti-26Nb-xZr-yMn (x = 4, 7, 10 wt% and y = 3, 5 wt%) alloys after compression testing (The alloys are named in the Txy format).

7.2.3. Strengthening mechanism

The strengthening mechanism for monolithic β phase Ti alloys has been recently modeled by Zhao et al. [159] through the integration effect of solid-solution hardening, grain-boundary hardening and dislocation hardening. The solid solution hardening is usually defined by the elastic misfit (η) and lattice parameter misfit (γ) between the solvent and solute atoms [156, 240]. The effect of solid solution strengthening was first studied by Fleisher et al [241], in which the effect of isolated solute atoms was determined in the crystal structure of the solvent. Thus, the isolated solute atoms hinder the dislocation movement. This approach was further extended by Gypen et al. [242] and Toda-Caraballo et al. [241] to approximate the solid solution hardening in multi component alloys. The solid solution hardening in multi-component alloys can be expressed using Eq. (7.1) [241]:

$$\sigma_{ss} = \left(\sum_i {B_i}^{3/2} X_i\right)^{2/3} \tag{7.1}$$

where σ_{ss} is yield strength component produced due to solid solution hardening, B_i is solid solution strengthening co-efficient which depends on η and γ, and X_i is fraction of solute atom

in an alloy. The values of B_i for the alloying elements Nb, Zr and Mn in Ti alloys were taken as 71, 1201, 1485 MPa.at.$^{-2/3}$, respectively [159]. Conventionally, the grain-boundary strengthening increases the strength of an alloy through grain-boundary refinement and therefore, it is also known as grain refinement strengthening [243]. It has been established that the small sized grains provide a greater number of grain boundaries which could immensely hinder the dislocations movement [158]. The grain-boundary strengthening in an alloy can be estimated using the classical Hall-Petch expression using Eq. (7.2) [243]:

$$\sigma_{gb} = \sigma_o + \frac{k_Y}{\sqrt{D}} \tag{7.2}$$

where σ_{gb} is yield strength component produced due to grain refinement, σ_o is friction stress, k_Y is Hall-Petch constant and D is mean grain size. The values of k_Y were derived using the expression Eq. (7.3):

$$k_y = k_{Ti} + \sum_i k_i X_i \tag{7.3}$$

where k_{Ti} and k_i are Hall-patch constants for pure Ti and alloying elements, respectively. The value k_{Ti} for pure Ti is 0.75 MPa $\sqrt{m}^{1/2}$ and the values of k_i for Nb, Zr and Mn in Ti alloys were taken as 1.05, 0.28, 0.06 MPa $\sqrt{m}^{1/2}$, respectively [243-245]. Moreover, the dislocation strengthening occurs when two dislocations gliding on the different slip planes cross each other and consequently, their total energy reduces and a new junction forms as a third dislocation segment [246]. This dislocation junction is immobilized and it impedes the other dislocations movement. The critically resolved shear stress (τ) needs to break this junction so that the dislocations cross each other based on a relationship Eq. (7.4):

$$\tau \propto \mu b/l \tag{7.4}$$

where μ is shear modulus, b is burgers vector and l is length between the interesting obstacles and the mean value of length (l_m) is related to dislocation density according to a relationship: $l_m \propto 1/\sqrt{\rho}$ [246]. This phenomenon leads to the famous Bailey-Hirsch expression demonstrating the dislocation strengthening as Eq. (7.5) [247]:

$$\sigma_\rho = \alpha M \mu b \sqrt{\rho} \tag{7.5}$$

where σ_ρ is yield strength component produced due to dislocation strengthening, α is mean junction strength (0.3), M is Taylor factor (2.8), μ is shear modulus for Ti (45 GPa), b is Burgers vector and ρ is dislocation density of an alloy [156, 159]. The theoretical yield stress

for β-type Ti alloys operating with slip dominated mechanism can be predicted using the following model that can be expressed as Eq. (7.6) [159].

$$\sigma_Y = \sigma_{Ti} + \alpha M \mu b \sqrt{\rho} + \left(\sum_i {B_i}^{3/2} X_i\right)^{2/3} + \frac{k_{Ti} + \sum_i k_i X_i}{\sqrt{D}} \quad (7.6)$$

where σ_{Ti} is slip activation critical stress for Ti. Considering the solid-solution, grain-boundary and dislocation strengthening mechanisms, the contribution of each strengthening mechanism estimated using the corresponding equations described above is presented in Fig. 7.5 for each TNZM alloy. It can be noted in Fig. 7.5 that the grain-boundary strengthening contributes the least in strengthening the TNZM alloys. By contrast, the dislocation and solid solution strengthening mechanisms are the main contributors in enhancing the strength of the TNZM alloys. Notably, the trend of σ_ρ is directly proportional to dislocation density of the TNZM alloys, whereas both Mn and Zr are producing the solid solution strengthening effect and increases the σ_{ss} in the TNZM alloys because of their high values of B_i in Ti alloys.

Nonetheless, Fig. 7.5 demonstrates the greater contribution of dislocation and solid-solution strengthening mechanisms as compared to grain-boundary strengthening because grain-boundary strengthening correlates with the grain size. All the TNZM alloys comprise large grain size (>120 μm). Therefore, the number of grain boundaries remains less and as a result, the contribution of grain-boundary strengthening remains less as compared to dislocation and solid-solution strengthening mechanisms. Moreover, dislocation strengthening can occur inside the grains as well as at the grain boundaries due to interaction of multiple dislocations, whereas the strengthening effect produced due to solid solution strengthening remains directly proportional to the amount of Zr and Mn added in the TNZM alloys, which can be evidently seen in Fig. 7.5. This demonstrates that the interaction of dislocations should have occurred extensively and therefore, the interaction of dislocations produces the greater amount of strengthening.

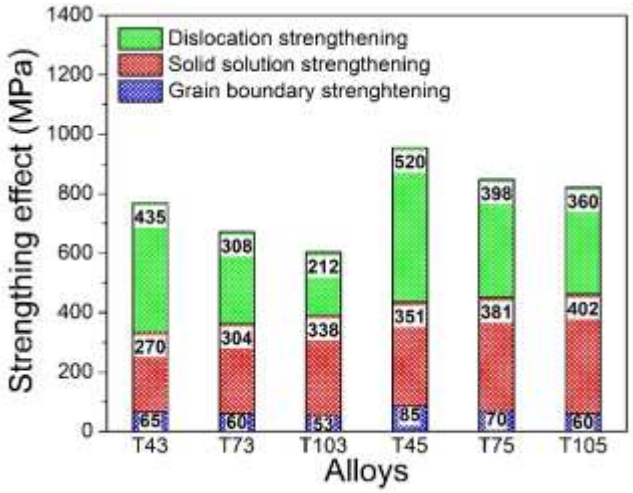

Fig. 7.5. The estimated strengthening contributions of the dislocation, solid-solution and grain-boundary strengthening mechanisms in yield strength of the Ti-26Nb-xZr-yMn (x = 4, 7, 10 wt% and y = 3, 5 wt%) alloys (The alloys are named in Txy format).

The values of measured true yield strength and dislocation density for all the TNZM alloys are presented in Fig. 7.6. It can be noted that measured engineering yield strength and measured true yield strength followed an identical trend. Therefore, from now onwards the values of true yield strength have been used in subsequent discussion. It can be noted in Fig. 7.6 the measured true yield strength displays an increasing trend upon the addition of Mn as a solute atom because Mn has relatively higher values of η and γ [138, 159]. Consequently, Mn produces a strong solid solution strengthening effect in the TNZM alloys. The direct relationship between true yield strength and dislocation density has been demonstrated by the Bailey-Hirsch relationship in Eq. (8). Accordingly, it can be noted in Fig. 7.6 that the dislocation density is directly proportional to the true yield strength for all the TNZM alloys. By contrast, the Hall-Petch relationship demonstrates the inverse relationship between the measured true yield strength and mean grain size of an alloy [243]. Hence, the measured true yield strength varies with mean grain size Table 7.1 for all the TNZM alloys. Thus, the measured true yield strength of all the TNZM alloys are influenced by the combined effects of solid-solution, grain-boundary and dislocation strengthening. Notably, T45 possesses the highest measured true yield strength (654 ± 12 MPa) among all the TNZM alloys.

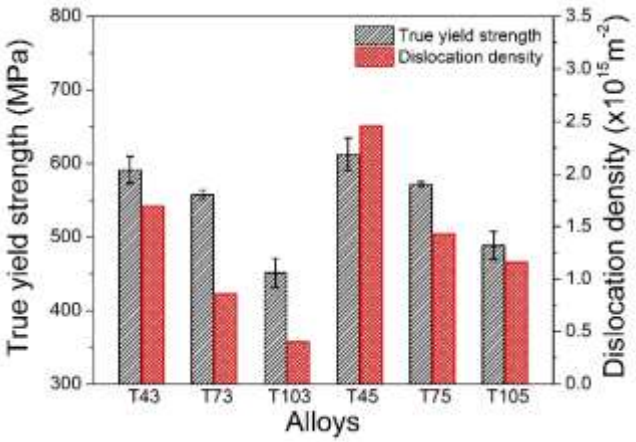

Fig. 7.6. True yield strength and dislocation density of the Ti-26Nb-xZr-yMn (x = 4, 7, 10 wt% and y = 3, 5 wt%) alloys (The alloys are named in Txy format).

As shown in Fig. 7.3a, the strain hardening ability of all the TNZM alloys is apparent. The strain hardening ability is generally characterized in terms of either the strain hardening rate or the strain hardening index [248]. In this work, to characterize the strain hardening ability of the TNZM alloys in the plastic region, the strain hardening index which symbolizes the resistance to plastic deformation [249] can be evaluated by using a classical Holloman expression using Eq. (7.7) [250].

$$\sigma_t = K{\varepsilon_t}^n \tag{7.7}$$

where σ_t is true stress, ε_t is true strain and K is strength coefficient of a material. The material demonstrates the perfect elastic fracture when the value of strain hardening index is equal to 1, whereas it displays a complete plastic deformation when the value of strain hardening index is equal to 0 [249]. To evaluate the values of n_1 & n_2 for the TNZM alloys, Eq. (7.7) is rearranged and rewritten as Eq. (7.8) [249].

$$ln\sigma_t = lnK + nln\varepsilon_t \tag{7.8}$$

By using Eq. (7.8), the $\ln\sigma_t$-$\ln\varepsilon_t$ plots for all the TNZM alloys are presented in Fig. 7.7. It can be noted in Fig. 7.7Fig. *7.7*f that the strain hardening is comprised of two stages. The n_1 displays the elastic-plastic deformation, whereas the n_2 shows the complete plastic deformation [249]. All the TNZM alloys exhibit the high n_1 and low n_2 values in the range of 0.428 ± 0.01 to 0.542 ± 0.01 and 0.125 ± 0.005 to 0.090 ± 0.006, respectively, which demonstrate their enhanced strain hardening behavior and good work formability. The values of n_1 & n_2 for the TNZM alloys rise upon increase in the Zr content, whereas the values of n_1 & n_2 demonstrate a decreasing trend upon increase in the Mn content. Similar results of strain hardening behavior

have been reported in the previous studies [251, 252]. The decreasing trend of the values of n_1 & n_2 is associated with an increase in dislocation density of the TNZM alloys [248]. Moreover, it has also been reported in previous studies that the strain hardening index of a material increases with increasing mean grain size up to a certain extent [253]. By contrast, strain hardening index decreases with increasing mean grain size when the amount of second phase is precipitated in an alloy [253]. The strain hardening index and mean grain size can be correlated by using the Morrison model as follows as presented in Eq. (7.9) [254]:

$$n = \frac{5}{(10+ D^{-1/2})} \tag{7.9}$$

where n is strain hardening index and D is mean grain size. In the present wok, all the TNZM alloys are comprised of a single phase. Therefore, it is noted that the values of n_1 & n_2 (Fig. 7.7Fig. *7.7*f) are directly proportional to mean grain size as presented in Table 7.1 for all the TNZM alloys. Furthermore, the values of strength coefficient presented in Table 7.3 follow the classical Hall-Petch relationship [255] as these values decrease with increasing values of n_1 & n_2 for all the TNZM alloys. The values of n_1 & n_2 for all the TNZM alloys demonstrate the high strain hardening ability and therefore, all of the TNZM alloys exhibit a significant plasticity and enhanced β phase stability [11, 256]. In conclusion to mechanical characterization and strengthening mechanisms for the TNZM alloys, T45 and T43 exhibit higher yield strength and significant strain hardening capability among all the TNZM alloys.

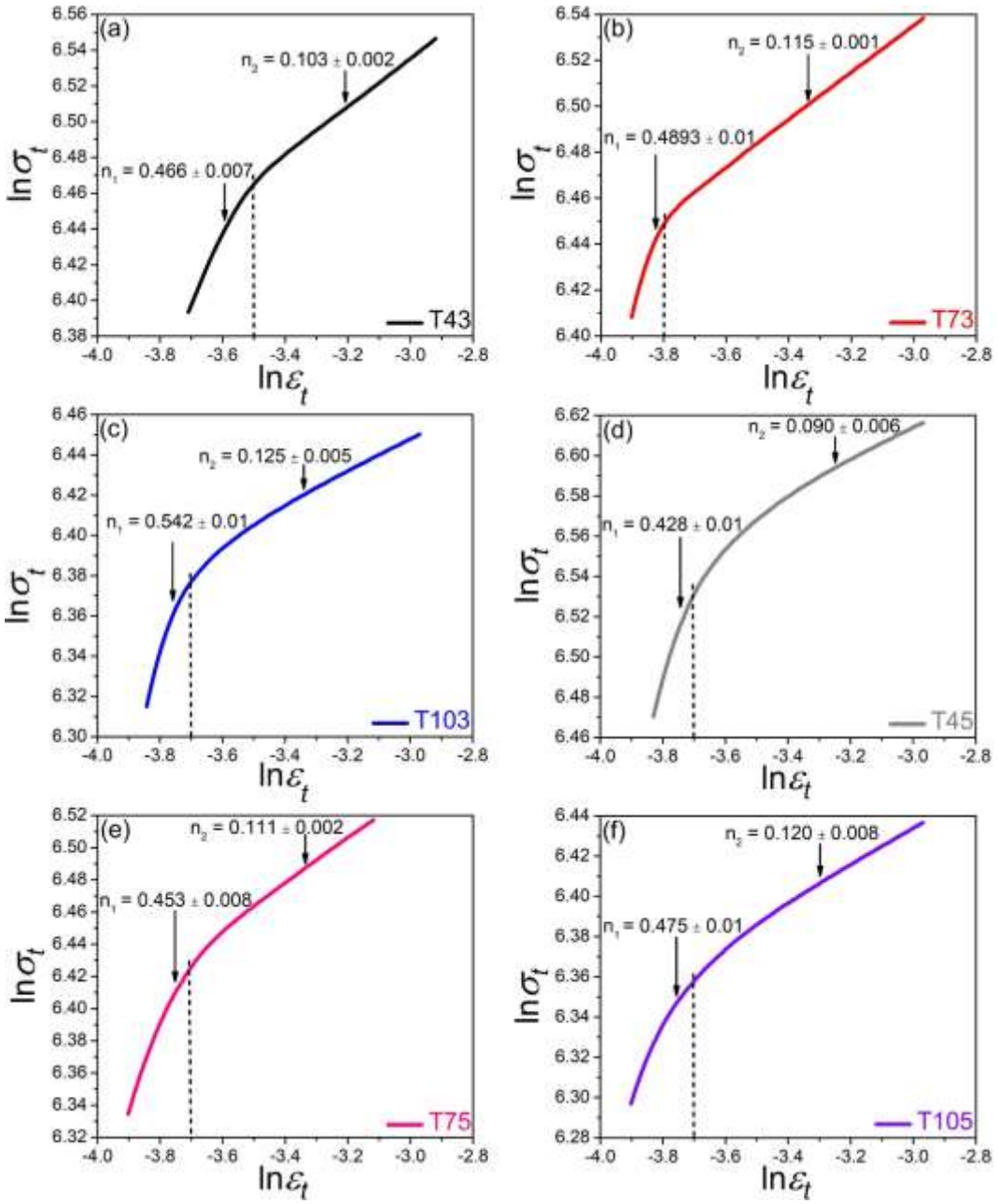

Fig. 7.7. Relationship between $\ln\sigma_t$ and $\ln\varepsilon_t$ for the Ti-26Nb-xZr-yMn (x = 4, 7, 10 wt% and y = 3, 5 wt%) alloys (The alloys are named in Txy format).

7.2.4. Electrochemical performance

It has been stated that any biomaterial used for orthopedic implant application should have enhanced electrochemical performance in the human body environment [257]. It has also been documented in the literature that the Ti-Nb-Zr system demonstrates excellent corrosion resistance with any amount of alloying elements as compared to Ti-6Al-4V in any artificial human body environment and for any immersion time for electrochemical analysis [257]. The high corrosion resistance of the Ti-Nb-Zr system is ascribed to quick formation of oxide film

(i.e., Ti oxide and Nb oxide) on the surface of material [191, 257]. Notably, these layers have capability to self-repair any film damages, which in turn resists the additional corrosion in the material [191]. Among the all the TNZM alloys, T43 and T45 exhibit superior mechanical properties. Therefore, the electrochemical analyses were performed for only T43 and T45 among the investigated TNZM alloys. The OCP curves for T43 and T45 are presented in Fig. 7.8a. The OCP curves display a slight fluctuation during the preliminary phase of the test. The fluctuating behavior is ascribed to electron movement occurred between the material surface and the simulated body fluid until the equilibrium potential attained for both sides [258]. It can be noted in Fig. 7.8a that both alloys attain a more positive and a stable state after few initial minutes; this trend attributes to the rapid development of oxide layer on the surface of alloys [259]. In order to better characterize the strength of the developed Ti and Nb oxide layers, potentiodynamic polarization curves are obtained in modified Hank's solution for T43 and T45 alloys and presented in Fig. 7.8b. The corrosion kinetics parameters, i.e. E_{corr} and i_{corr}, are obtained from the Tafel region of the potentiodynamic polarization curves. In the present work, the E_{corr} values of T43 and T45 are -0.45 and -0.48 V, respectively. The relatively positive values of E_{corr} for T43 and T45 alloys demonstrate their better corrosion resistance than the as-cast CP-Ti, i.e., -0.58 V [191]. In general, according to the concept of electrochemistry, the high value of E_{corr} and the low value of i_{corr} are the indicators for good corrosion resistance of a material [259, 260]. The reported value of i_{corr} in this work for T43 and T45 are 0.838 and 0.839 nA/cm^2, respectively. Both the alloys exhibit lower i_{corr} value than the as-cast Ti-6Al-4V, i.e., 1.037 nA/cm^2 [259]. Thus, the investigated T43 and T45 alloys demonstrate a better corrosion resistance than CP-Ti and Ti-6Al-4V. Furthermore, the EIS study was carried out on the T43 and T45 alloys to illustrate the nature of formed passive oxide layer. The characterization of electron movement resistance can usually be performed by EIS Nyquist curve. The extent of semi-circular arc radius on EIS Nyquist plot is directly proportional to the corrosion resistance of a material [260]. The radius of a semi-circular arc for T43 is somewhat higher than T45, as presented in Fig. 7.8c which demonstrates that the passive oxide film of T43 has better polarization resistance on the surface [258]. The Bode impedance plot and the Bode phase plot are presented in Fig. 7.8d. The Bode impedance plot displays two distinct phases: (i) the flat phase in the frequency range of 1×10^5 Hz to 1×10^3 Hz, the flat portion illustrates the solution resistance [258], (ii) the inclined phase in the frequency range of 1×10^3 Hz to 1×10^{-1} Hz. The impedance increases up to 1×10^6 Ω cm^2 during this phase. Moreover, the phase angle close to 90 ° demonstrates a denser passive oxide film [191]. In the present work, the Bode phase angle plot displays a wide plateau above phase angle of 80 ° from middle to low frequency range

which illustrates the formation of denser passive oxide films on the surface of both alloys.

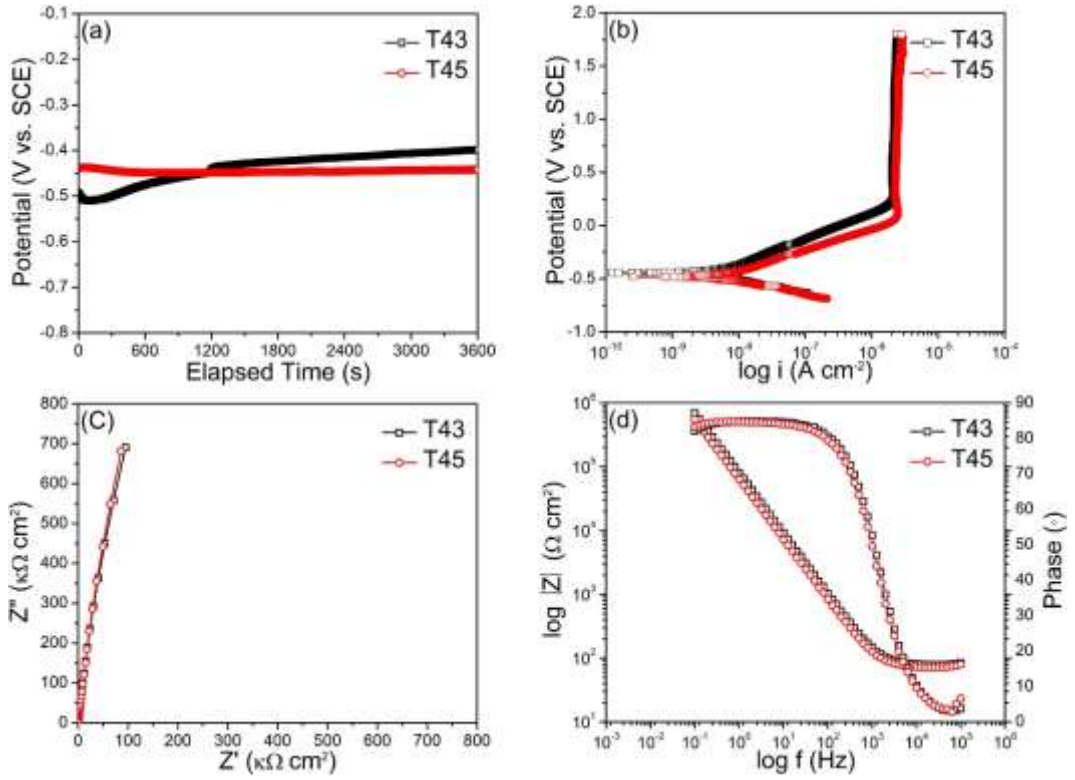

Fig. 7.8. Results of the electrochemical tests for the T43 and T45 alloys in modified Hank's solution at a pH value of 7.4 at room temperature. (a) Open circuit potential curves vs. time (b) Potentiodynamic polarization curves. EIS results in the form of (c) Nyquist plots and (d) Bode plots.

Moreover, the SEM-EDX surface analyses were performed in order to confirm the formation of oxides on the surface of T43 and T45 alloys after corrosion tests. Fig. 7.9 shows the formation of oxides on the surface of T43 and T45 (after 1 h immersion into Hank's solution). The similar kind of oxide formation has been reported for Ti-5Cu alloy after corrosion analysis [260]. The formation of oxides on the surface of T43 and T45 alloys has been further confirmed by means of EDX spectrum analysis which was performed on the oxide particles as well as on the surface other than oxide particles. The EDX spectra of T43 and T45 alloys (Fig. 7.9c-d) exhibit a peak of oxygen besides the peaks of other elements composing the alloys, i.e., Ti, Nb, Mn and Sn suggesting the formation of surface passive film by a mixture of oxides. Hence, the SEM-EDX surface analyses results are in good agreement with results of electrochemical tests. Based on the points discussed above, T43 and T45 alloys exhibit good corrosion resistance for their use in orthopedic implant applications.

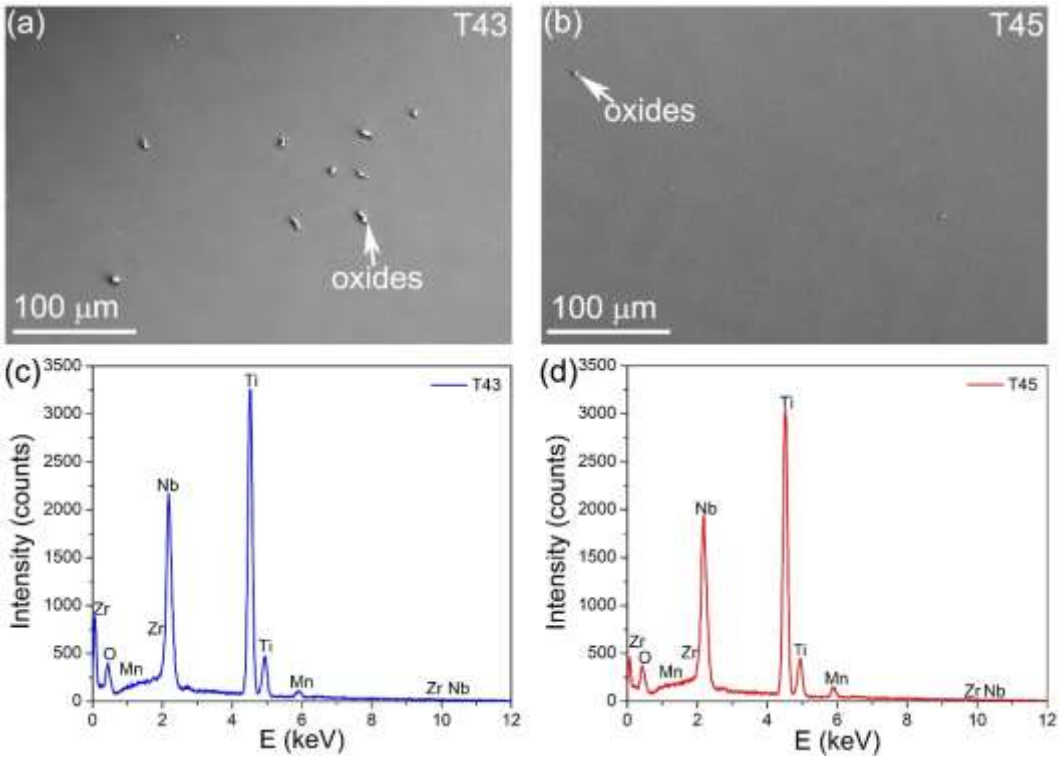

Fig. 7.9. The SEM micrographs of (a) T43 (b) T45 after corrosion test in Hank's solution and their corresponding EDX spectra (c) T43 (d) T45.

7.3. Conclusions

The present work evaluates the phase, microstructure and mechanical characterizations including and the strengthening mechanisms of the newly designed Ti-26Nb-xZr-yMn (x = 4, 7, 10 wt% and y = 3, 5 wt%) alloys and based on the superior mechanical properties among the investigated alloys the electrochemical kinetics of the Ti-26Nb-4Zr-3Mn Ti-26Nb-4Zr-5Mn alloys. The key findings from this work are summarized as below.

- The phase and microstructural analyses illustrate a monolithic β phase in all the investigated alloys.
- All the investigated alloys exhibit a pronounced true plastic strain (~ 160%) and a true maximum strength (~ 950 MPa) and do not show any fracture in compression testing.
- The addition of Mn positively affects the strength of the Ti-Nb-Zr system alloys. The strengthening in the present work is influenced by combined effect of solid-solution, grain-boundary and dislocation strengthening.
- The Ti-26Nb-4Zr-3Mn and Ti-26Nb-4Zr-5Mn alloys demonstrate an improved electrochemical performance as compared to commercially available biomaterials.

Among the investigated alloys, Ti-26Nb-4Zr-5Mn displays a superior combination of true

maximum strength (951 MPa), large true plasticity (162%), highest true yield strength (654 MPa), dislocation density (2.45×10^{15} m^{-2}) and hardness (242 HV) along with improved strain hardening ability and electrochemical kinetics considering the high strain hardening indices (0.42 and 0.09) and low corrosion current density (0.839 nA/cm^2). Therefore, Ti-26Nb-4Zr-5Mn could be the promising candidate for orthopedic implant applications.

8. Tailoring deformation and superelastic behaviors of beta-type Ti-Nb-Mn-Sn alloys

This work has been published in "*Journal of Mechanical Behavior of Biomedical Materials*".

In this work a new series of alloys Ti-25Nb-xMn-ySn have been designed. The phase, microstructure, mechanical and superelastic behaviors of the aforementioned group of alloys have been investigated in this work for the biomedical applications.

8.1. Results and discussion

8.1.1. Empirical design for novel Ti alloys

The novel series of the Ti-25Nb-xMn-ySn (Ti25xy) alloys were empirically designed on the basis of a "*BF-d-electron superelasticity"* empirical relationship based on Coulomb's law and *d*-electron alloy theory, as developed by Morinaga [261, 262]. The Coulomb's law demonstrates that the attractive force between two charges is directly proportional to their multiplication and inversely proportional to the square of the distance between them, which can be shown, as below in Eq. (8.1):

$$F \propto \frac{q_1 q_2}{r^2} \tag{8.1}$$

where q1 and q2 are the electric charges and r represents the distance between them. The positive charge on ion cores refers to the effective nucleus charge (Zeff) experienced by valence electrons which is regarded as q1. The value of Zeff can be calculated by using the relationship (Zeff = Z–s), where Z is the atomic number and s is the Slater shielding parameter. The other two electronic parameters used in the d-electron alloy theory are named as bond order (Bo) and metal d orbital energy level (Md), which are calculated particularly for distinctive alloying elements in bcc Ti and hcp Ti clusters [263]. The parameter Bo demonstrates the probability distribution of valence electrons between atoms of alloying elements and Ti. Therefore, Bo is regarded as q2 charge, which operates to neutralize the positive charge of the ion core and restricts it in metallic crystal. The parameter Md displays the d orbital energy level of an alloying element, where the level of Md is directly related with metallic radius irrespective the shell in which element is present. Hence, the Md value can be considered as an approximated value of the metallic radius. By combining d-electron theory and Coulomb's law the interatomic bonding force (BF) of Ti alloys can be measured using Eq. (8.2):

$$BF \propto \frac{\overline{Z_{eff}} \cdot \overline{Bo}}{\overline{Md}} \quad (8.2)$$

where $\overline{Z_{eff}}$, $\overline{Bo}$ and $\overline{Md}$ are the compositional averages of the effective charge experienced by valence electron, bond order and metal *d* orbital energy level, respectively. The values of theoretically designed electronic parameters of the investigated Ti25xy alloys were calculated, with their results presented in Table 8.1 It has been reported that alloys having high *BF* values are anticipated to respond elastically to a large stress [17]. Hence, a high amount of recoverable strain is expected to be achieved in theoretically designed alloys with a high *BF* value [17]. *BF* values reported for recently developed Ni-free superelastic and shape memory Ti alloys are typically in the range of 1.54 – 1.69 [17]. Therefore, in the present work, all the Ti25xy alloys with *BF* values in the range of 1.61 – 1.76 (Table 8.1) are anticipated to exhibit high recoverable strain.

Table 8.1 The electronic parameters for all the Ti-25Nb-xMn-ySn (wt%; x = 2,4 and y = 1,5; denoted in the form of Ti25xy) alloys. $\overline{Bo}$ and $\overline{Md}$ are the compositional averages of bond order and metal d orbital energy level, respectively; $\overline{Z_{eff}}$ is the compositional averages of the effective charge experienced by valence electron; BF is the interatomic bonding force and e/a is the valence atom to electron ratio.

Alloys	Compositions (wt%)	$\overline{Bo}$	$\overline{Md}$	$\overline{Z_{eff}}$	BF	e/a
Ti2521	Ti-25Nb-2Mn-1Sn	2.8320	2.4168	3.336	1.617	4.20
Ti2525	Ti-25Nb-2Mn-5Sn	2.8235	2.4094	3.388	1.648	4.22
Ti2541	Ti-25Nb-4Mn-1Sn	2.8308	2.3916	3.490	1.727	4.26
Ti2545	Ti-25Nb-4Mn-5Sn	2.8222	2.3834	3.547	1.762	4.28

8.1.2. Phase constitution and morphology

Fig. 8.1 shows the XRD patterns of the Ti25xy alloys. Among all the investigated Ti25xy alloys, only Ti2521 demonstrates the peaks of dual phases, i.e., the bcc β and orthorhombic α" phases (PDF card # 00-044-1288 and 01-078-4886). By contrast, the other investigated Ti25xy alloys, i.e., Ti2525, Ti2541 and Ti2545, illustrate the peaks of a single bcc β phase (PDF card # 00-044-1288). The values of volume fraction for α" and β phases in the Ti25xy alloys are presented in Table 8.2. The monolithic bcc β phase has been achieved in the Ti25xy alloys by adding further 2 wt% Mn or 4 wt% Sn to Ti2521 alloy. This phenomenon clearly manifests that both the alloying elements Mn and Sn contribute to the β-phase stability of Ti alloys [264, 265]. It can be noted in Fig. 8.1 that the diffraction peaks shift to higher 2θ angels when increasing the amount of Mn in the Ti25xy alloys. Moreover, the estimated a_β for all the Ti25xy alloys are presented in Table 8.2, which shows a decreasing trend when increasing the content of Mn in the

Ti25xy alloys. Both the preceding phenomena are attributed to the larger difference in atomic radii of Mn (0.127 nm) in comparison of that of Ti (0.147 nm) [42]. By contrast, the addition of Sn increases the a_β for the Ti25xy alloys; where a similar trend has been documented in existing literature [20, 201]. The a_β for all the Ti25xy alloys are lower than the standard a_β for Ti (0.3306 nm), which demonstrates that a_β for the Ti25xy alloys are lower due to the addition of Mn with smaller atomic radius in all the Ti25xy alloys [42].

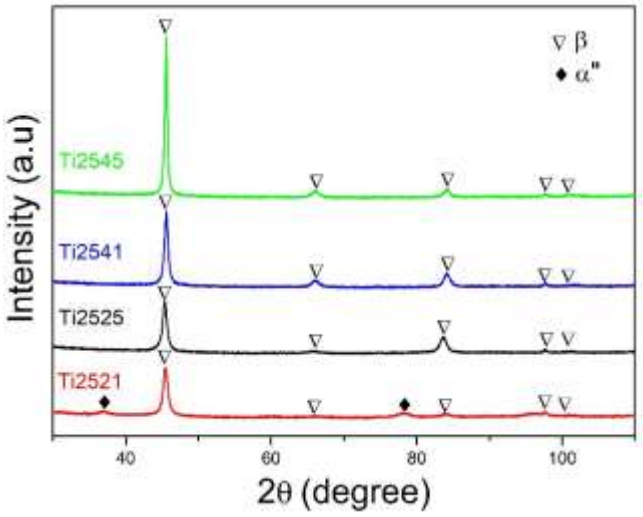

Fig. 8.1. The XRD spectra for all the Ti-25Nb-xMn-ySn (x = 2,4 wt% and y = 1,5 wt%) alloys (The alloys are designated as Ti25xy).

Table 8.2. The constituent phases, volume fraction (V_f) estimated from XRD peaks, lattice parameter of β phase (a_β) and the average grain size of β phase (D_β) for all the investigated Ti25xy alloys.

Alloys	**Compositions (wt%)**	**Phases**	**$V_{f,\alpha}$ (%)**	**$V_{f,\beta}$(%)**	**a_β (nm)**	**D_β (μm)**
T2521	Ti-25Nb-2Mn-1Sn	β+α"	10	90	0.3281	151 ± 48
T2525	Ti-25Nb-2Mn-5Sn	β	0	100	0.3285	188 ± 50
T2541	Ti-25Nb-4Mn-1Sn	β	0	100	0.3272	105 ± 36
T2545	Ti-25Nb-4Mn-5Sn	β	0	100	0.3275	163 ± 49

In general, the β-phase stability in multi-component Ti alloys is a function of the amount of β-stabilizers alloyed in Ti alloys [16]. If the amount of β stabilizing elements is eliminated or added in a trace quantity, then only the α phase would exist upon quenching [16, 266]. If an intermediate quantity of β-stabilizers is added, then α+β phases would be present in Ti alloys upon quenching [16]. Upon addition of high enough quantities of β-stabilizers, only the

metastable β phase would dominate in Ti alloys, which usually undergoes some martensitic transformation, i.e., β → α', β → α" and β → ω, upon quenching [11, 267, 268]. The formation of previously mentioned martensitic phases upon quenching can be inhibited by the addition of an adequate amount of β-stabilizing elements in Ti alloys [16]. In this work, β-stability is achieved with the addition of Mn and Sn as alloying elements in the Ti25xy alloys. Fig. 8.2 illustrates the microstructural features of the Ti25xy alloys. The Ti2521 alloy displays significant retention of the β phase along with a small fraction of acicular α" martensitic phase which forms within the β matrix upon cooling as shown in Fig. 8.2a inset. By contrast, Ti2525, Ti2541 and Ti2545 alloys (Fig. 8.2b-d) exhibit a monolithic β phase in their microstructures. The β-stabilizing attribute of Mn and Sn as the alloying elements shows that a single β phase can be attained by further addition of 2 wt% Mn or 4 wt% Sn in Ti2521 alloy. Furthermore, the dendritic substructure can be clearly observed in Fig. 8.2 for each Ti25xy alloy. The dendritic substructure has formed during solidification when element with a high melting point (such as Nb used in this work) has been added to Ti alloys. This remarkable segregation occurred during solidification is due to the Nb element with a high melting point [140], which leads to a partition co-efficient higher than 1 when it dissolves in Ti alloys. The partition coefficient is defined as the ratio of solute constituents in the solid to that of in the liquid during solidification [269]. The partition coefficient is 1 when it is in equilibrium, where it is either <1 or >1 when the liquid in the surrounding of solid/liquid boundary is either enriched or depleted of solute, respectively [269]. The chemical speciation via EDX point analysis for dendritic substructure demonstrates the chemical homogeneity in all the Ti25xy alloys. Therefore, only the chemical speciation results for the dendritic substructure in Ti2541 are presented in Table 8.3. The backscattered electron (BSE) SEM image of Ti2541 in Fig. 8.2c which shows that the points marked by 1, 2 and 3 at lighter contrast display dendritic-core region whereas the points marked by 4, 5 and 6 are at darker contrast show inter-dendritic region. It is of noteworthy as presented in Table 8.3Table *8.3* that, the concentrations of Nb obtained in the dendritic-core areas (lighter contrast) against the points 1, 2, 3 are higher than its nominal composition; on the other hand, the inter-dendritic (darker contrast) region against the points 4, 5, 6 has higher Ti concentration than its nominal composition. This phenomenon occurs due to the higher melting point of Nb as compared to Ti. Additionally, the low-magnification micrographs presented in Fig. 8.3 were used to estimate the β grain size for each Ti25xy alloy. In this method, the β grain size of various β grains was measured using imageJ software and then average β grain size values for each Ti25xy alloy were taken and are presented in Table 8.2. As seen from Table 8.2, the Ti2541 alloy exhibits the smallest grain size of 105 ± 36 μm whereas the Ti2525 alloy

possesses the largest grain size of 188 ± 50 μm among the investigated Ti25xy alloys. It has been reported that different factors influence the microstructure of as-cast Ti alloys by affecting either growth or nucleation during solidification. The influence of solute elements on grain refinement of as-cast Ti alloys can be quantified using growth restriction factor. The growth restriction factor demonstrates the segregating potency of all alloying elements during solidification in the alloy. It has an important role in controlling the grain size of as-cast Ti alloys [234, 270]. Easton and John [271] has established a simple relationship between the growth restriction factor and the simple relationship between the growth restriction factor and the grain size for an alloy composition as shown below in Eq. (8.3):

$$d = a + \frac{b}{Q} \tag{8.3}$$

where, *d* is grain size, *a* is maximum number of active nucleants, *b* is nucleant potency and *Q* is growth restriction factor. Notably, the mean grain size decreases when the amount of Mn increases because it contains high growth-restriction factor whereas the mean grain size increases when the amount of Sn increases because it contains zero growth-restriction factor as a solute atom in Ti alloys [234]. Similar trend has been documented in previous work [234, 272]. Hence, the results of phase constitution are consistent with microstructural features of all the investigated Ti25xy alloys.

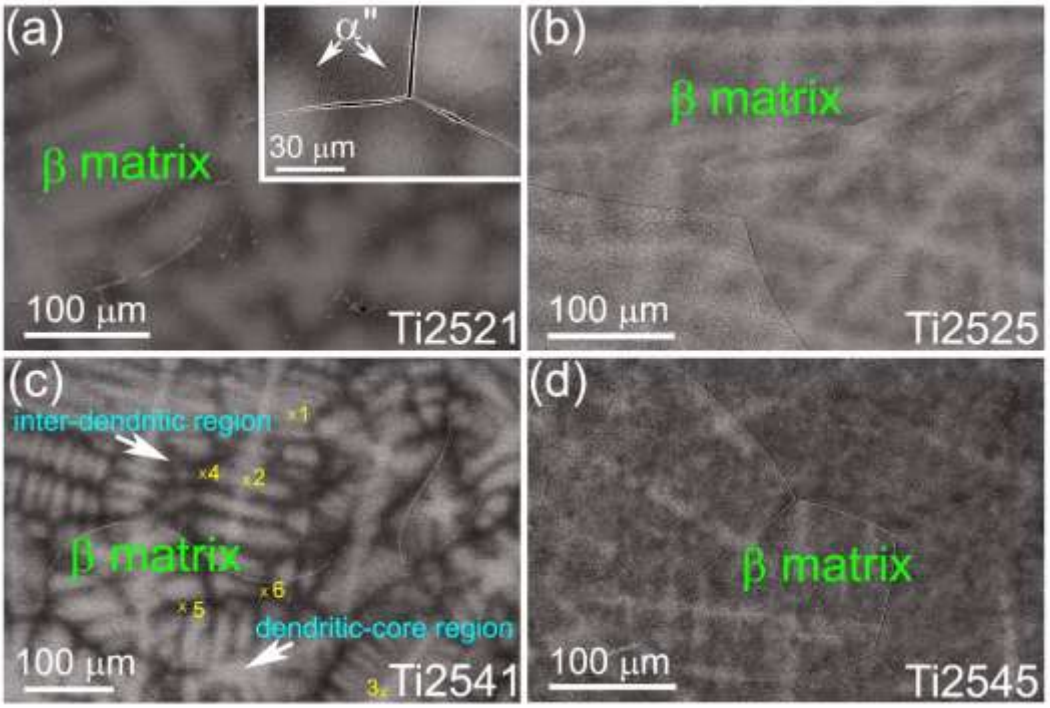

Fig. 8.2. The backscattered electron SEM images for all the Ti-25Nb-xMn-ySn (x = 2,4 wt% and y = 1,5 wt%) alloys (The alloys are designated as Ti25xy).

Table 8.3. The results of EDX point analysis measured on the points marked in Fig. 8.2c for Ti2541 (i.e., Ti-25Nb-4Mn-1Sn) alloy.

Points marked	**Ti (wt %)**	**Nb (wt %)**	**Mn (wt %)**	**Sn (wt %)**
1	65.0 ±1.2	31.9 ±1.1	2.4 ±0.6	0.7 ±0.6
2	65.0 ±0.6	30.8 ±0.8	3.2 ±0.3	1.1 ±0.3
3	64.7 ±1.3	31.0 ±1.3	2.7 ±0.7	1.6 ±0.6
4	71.3 ±0.6	23.3 ±0.6	4.7 ±0.3	0.8 ±0.3
5	71.2 ±2.5	21.3 ±2.4	6.0 ±1.4	1.5 ±1.1
6	70.7 ±1.2	23.1 ±1.1	5.0 ±0.7	1.2 ±0.5

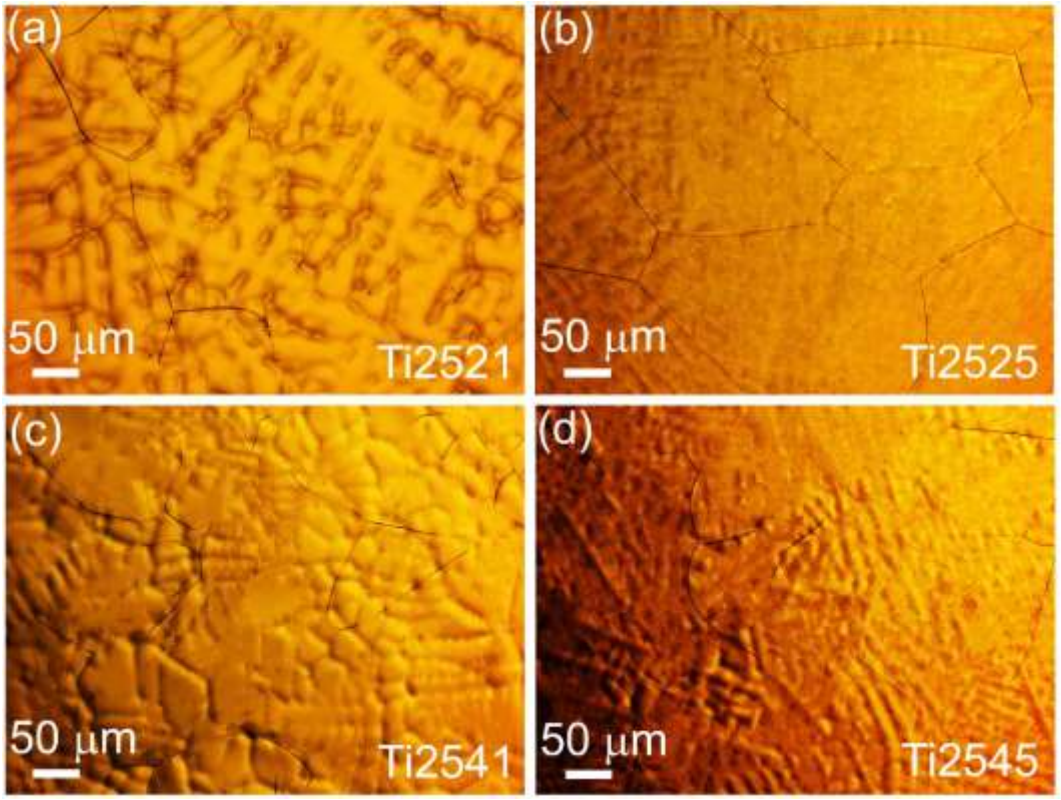

Fig. 8.3 The optical micrographs for all the Ti-25Nb-xMn-ySn (x = 2,4 wt% and y = 1,5 wt%) alloys (The alloys are designated as Ti25xy).

8.1.3. Mechanical properties

Generally, the mechanical performance of Ti alloys is a function of their phase constitutions and microstructural features. In order to evaluate the mechanical performance of newly designed Ti25xy alloys, the static compression tests, cyclic loading-unloading tests, Vickers micro-hardness tests and deformation behaviors were carried out in this work. Fig. 8.4 presents the uniaxial compressive stress-strain curves for all the Ti25xy alloys at room temperature. All the Ti25xy alloys except for Ti2521 demonstrate a substantial plasticity and do not fail until the load reaches the load capacity of mechanical testing machine (i.e., 100 kN). Notably, the addition of sufficient quantities of Mn and Sn in the Ti25xy alloys can considerably enhance the mechanical properties of the Ti25xy alloys. The room-temperature stress-strain curves of all the Ti25xy alloys except Ti2521 consist of three regions: (i) a linear elastic region, (ii) a stress plateau region and (iii) a strain hardening region. By contrast, Ti2521 demonstrates fracture in linear plastic region during static compression testing.

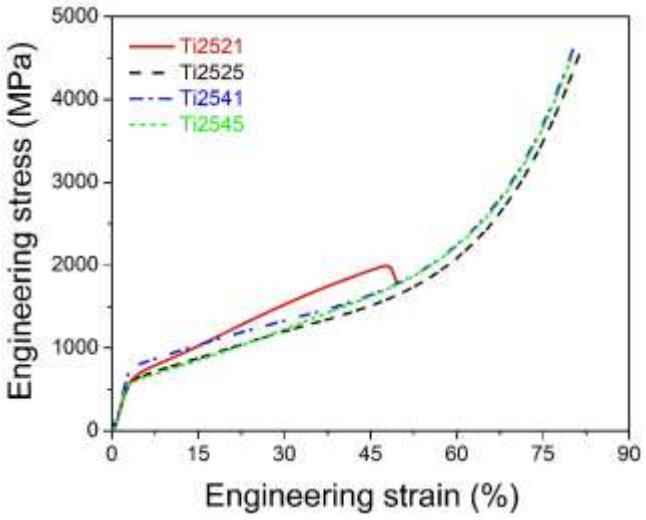

Fig. 8.4. The engineering stress - strain curves for all the Ti-25Nb-xMn-ySn (x = 2,4 wt% and y = 1,5 wt%) alloys (The alloys are designated as Ti25xy). All Ti25xy alloys except Ti2521 did not fail when the load reached the load capacity of mechanical testing ma machine (100 kN).

It can be noted in Fig. 8.4 that none of the Ti25xy alloys except Ti2521 has failed during testing, where the values of total plastic strain and ultimate compressive strength cannot be calculated for Ti25xy alloys except for Ti2521 which shows the total plastic strain of 41 ± 2.5 % and the ultimate compressive strength of 1800 ± 25 MPa. The Ti2521 alloy demonstrates a relatively low β-phase stability and comprising dual phase (α"+β) microstructure, which subsequently leads to its failure during compression testing [11]. By contrast, further addition of β-stabilizing elements in Ti25xy alloys leads to a monolithic β phase in their microstructure. Therefore, enhanced β stability has increased the number of slip systems, which results in easy deformation and large plasticity displayed in Ti2525, Ti2541 and Ti2545 alloys [13, 14, 264, 273]. The 0.2% strain offset method was used to estimate the compressive yield strength for all the Ti25xy alloys obtained from the engineering stress-strain curves of the Ti25xy alloys and the results are presented in Fig. 8.5; the values of compressive yield strength are affected by the concentration of Mn and Sn added in the Ti25xy alloys. It can be inferred from the trend of yield strength in Fig. 8.5 that, among the Ti25xy alloys, the alloy contains a highest content of Mn and a lowest content of Sn (i.e., Ti2541) shows the highest yield strength (710 ± 35 MPa) among the Ti25xy alloys. This is attributed to the strong solid solution strengthening effect as per the Hume-Rothery principle resulted from the smaller atomic radius of Mn compared to that of Ti [42]. Therefore, an increase in the amount of Mn enhances the yield strength of the Ti25xy alloys. Furthermore, the addition of Mn in the Ti25xy alloys reduces their grain size (Table 8.2). Hence, the grain boundary strengthening also contributes to the enhancement in the yield strength when raising the amount of Mn in Ti25xy alloys [42]. By contrast, the alloy

contains the lowest Mn content and the highest Sn content (i.e., Ti2525) exhibits the lowest yield strength (563 ± 23 MPa) among the Ti25xy alloys. This phenomenon results from an increase in a_β and/or an increase in grain size of the Ti25xy alloys (Table 8.2) when increasing the amount of Sn in the Ti25xy alloys [42]. Hence, the addition of Sn causes a decline in the yield strength of Ti25xy alloys [226]. Conversely, the highest Vickers micro-hardness (244 ± 6.3 HV) is observed in the Ti2521 alloy because it contains orthorhombic α" phase in microstructure [40]. The trend of hardness in Fig. 8.5 decreases with further addition of Mn and Sn due to having monolithic β phase in its microstructure, where the hardness of an alloy is affected by its primary microstructure [211]. Moreover, the trend of hardness for monolithic β alloys is similar to the trend of yield strength since hardness and yield strength are directly proportional to each other [210].

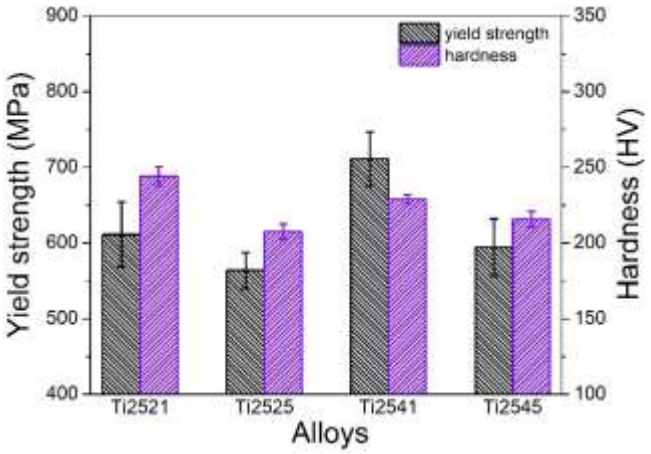

Fig. 8.5. Yield strength ($\sigma_{0.2}$) and hardness (H) of the Ti-25Nb-xMn-ySn (x = 2,4 wt% and y = 1,5 wt%) alloys (The alloys are designated as Ti25xy).

To evaluate the superelastic behavior of the Ti25xy alloys, the loading-unloading stress-strain curves for all the Ti25xy alloys are presented in Fig. 8.6. All the investigated Ti25xy demonstrate pseudo-elastic shape recovery upon unloading.

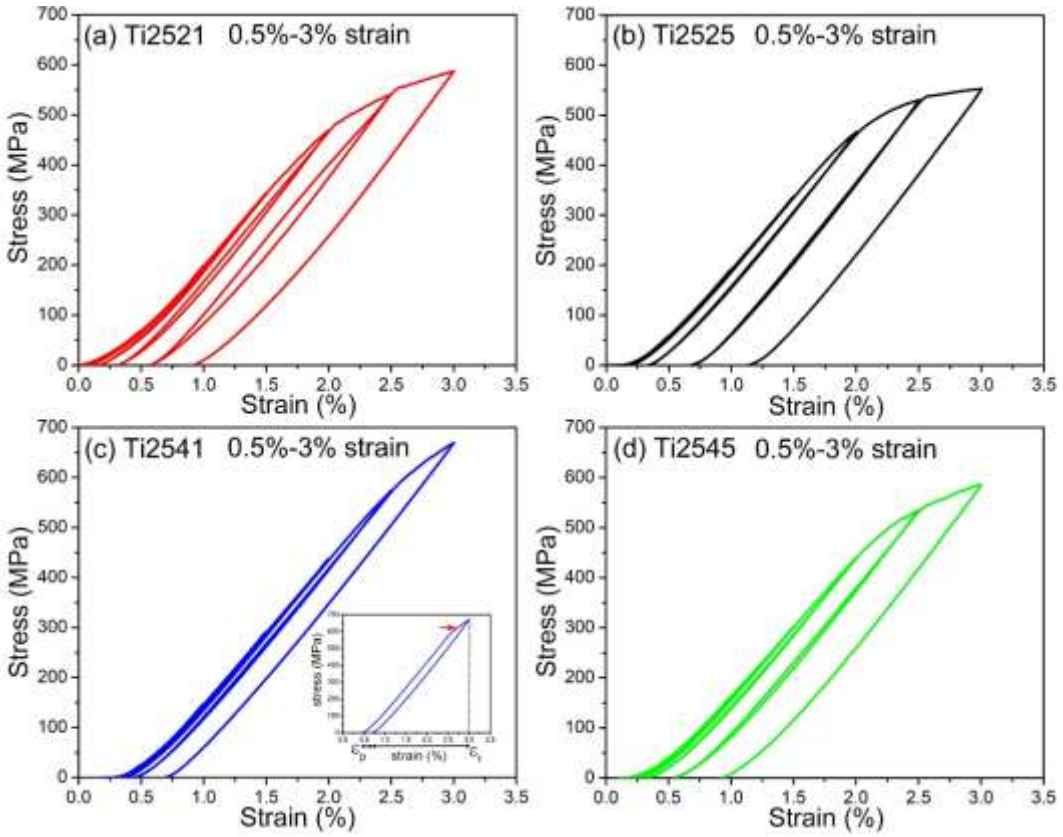

Fig. 8.6. The cyclic loading-unloading stress-strain curves for all the Ti-25Nb-xMn-ySn (x = 2,4 wt% and y = 1,5 wt%) alloys up to 3% engineering strain (The alloys are designated as Ti25xy).

In order to further illustrate the superelastic behavior of the Ti25xy alloys, the strain recovery rate and two types of strains during cyclic loading and unloading are described as follows: (i) the residual strain (ε_p) which remains permanent after unloading, (ii) the recoverable strain (ε_r) which is recovered after unloading and (iii) the superelastic recovery ratio (η) which can be defined as in Eq. (8.4) [265, 274]:

$$\eta = \frac{\varepsilon_r}{\varepsilon_r + \varepsilon_p} \tag{8.4}$$

The ε_r and ε_p are measured using loading-unloading stress-strain curves for each Ti25xy alloy as characterized in Fig. 8.6c inset. The values of ε_r for Ti2525, Ti2525, Ti2541 and Ti2545 are found to be 2.08, 1.80, 2.35 and 2.05 %, respectively. As seen from Fig. 8.6, all the Ti25xy alloys exhibit moderate pseudo-elastic shape recovery property. The η values for the Ti25xy alloys are displayed in Fig. 8.7. All the Ti25xy alloys exhibit adequate η where the Ti2541 alloy exhibits the highest η among the investigated Ti25xy alloys. Thus, the addition of Mn in the Ti25xy alloys improves their superelastic behavior. Furthermore, it has been reported that the superelastic shape recovery behavior of an alloy is due to the martensitic transformation and

martensitic reverse transformation upon loading and unloading, respectively, where the increase in σ_{SIM} may enhance the superelastic behavior of an alloy [265, 275, 276]. To clearly demonstrate the effect of alloying elements (i.e., Mn and Sn) on the superelastic behavior of the Ti25xy alloys, the values of σ_{SIM} were calculated using cyclic loading curves [277] (indicated by red arrow in Fig. 8.6c inset) for all the Ti25xy alloys and are presented in Fig. 8.7. It can be inferred from Fig. 8.7 that the values of η and σ_{SIM} demonstrate a similar changing trend. It is well known that Mn is a strong β stabilizing element [41]. Therefore, addition of Mn in Ti25xy alloys suppresses the martensitic transformation from β phase, which enhances the stress σ_{SIM}. In all the Ti25xy alloys, it can be noted that ε_r increases as σ_{SIM} increases during cyclic loading, which improves the superelasticity of Ti25xy alloys.

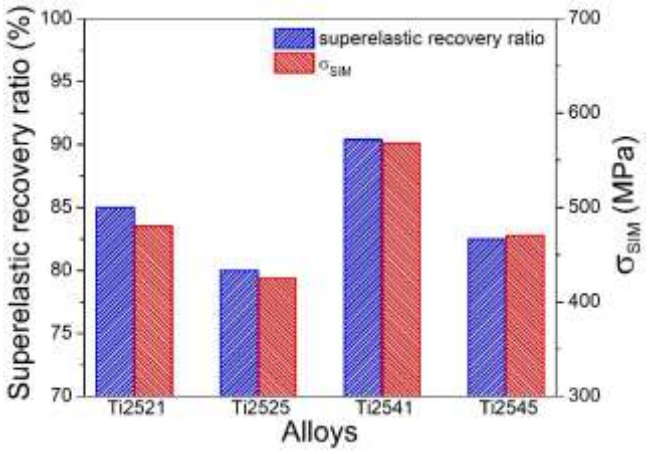

Fig. 8.7. The superelastic recovery ratio (η) versus critical stress for inducing martensite (σ_{SIM}) for all the Ti-25 wt% Nb-xMn-ySn (x = 2,4 wt% and y = 1,5 wt%) alloys (The alloys are designated as Ti25xy).

The evaluation of energy absorption is one of the key parameter in order to assess the performance of biomedical implant material. Therefore, in this work the absorbed total energy from displacement 0 to h_{max} for all the Ti25xy alloys can be evaluated using the Eq. (8.5) presented as below [278]:

$$W_T = \int_0^{h_{max}} P(h)\, dh \tag{8.5}$$

where W_T is the absorbed total energy and P is the applied loading force. The absorbed elastic energy during the deformation is calculated by using the Eq. (8.6) presented as below:

$$W_E = \int_{h_f}^{h_{max}} P(h) dh \tag{8.6}$$

where W_E represent the absorbed elastic energy and h_f denotes the displacement after unloading.

The absorbed plastic energy W_P can be given by using Eq. (8.7) shown as below:

$$W_P = W_T - W_E \tag{8.7}$$

Fig. 8.8a demonstrates the absorbed energy distribution. The absorbed total energy is the maximum stress at a certain strain level, which constitutes both the plastic and elastic absorbed energies. The high absorbed plastic energy is due to the movement and generation of slip and/or dislocation bands while the high absorbed elastic energy results in enhanced recovery after unloading. It can be noticed in Fig. 8.8b-d the Ti2525 demonstrates the lowest absorbed total energy as it possesses the lowest maximum stress during each cycle. By contrast, Ti2541 demonstrates the highest absorbed total energy. Notably, Ti2541 demonstrates the best recovery after loading among all the Ti25xy alloys; hence, it exhibits the highest absorbed total energy. The Ti2521 and Ti2545 have similar absorbed elastic energy but different absorbed total energy. Specifically, the Ti2521exhibits higher absorbed plastic energy compared with Ti2545 alloy.

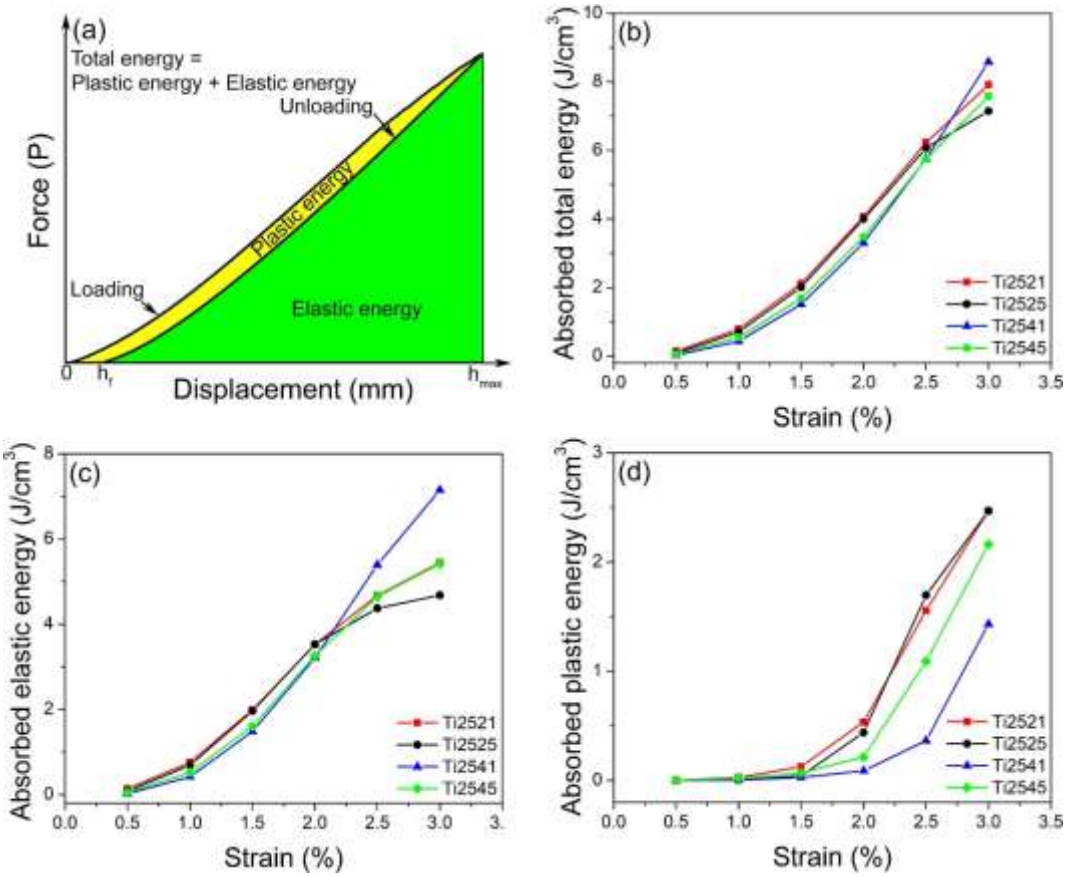

Fig. 8.8. The absorbed energy for all the Ti-25 wt% Nb-xMn-ySn (x = 2,4 wt% and y = 1,5 wt%) alloys: (a) the pictorial representation for absorbed energy, (b) the absorbed total energy, (c) the absorbed elastic energy, and (d) the absorbed plastic energy. (The alloys are designated as Ti25xy).

The occurrence of deformation bands is a kind of in homogeneity which originates in an alloy

during plastic deformation [279]. The shear bands occur at oblique angels with reference to primary deformation axis and infiltrate several crystals in the deformation structure [279]. To characterize the formation of shear bands, the deformation analyses were carried out on the outer surface of the Ti25xy alloys. The Ti2521 alloy contains α" phase and displays sufficient plasticity of (41 ± 2.5 %). Therefore, Ti2521 alloy shows some shear bands and cracks in its deformed morphology (Fig. 8.9a) [11]. By contrast, the Ti2525, Ti2541, Ti2545 alloys do not fail during compression testing, consequently all of them display several shear bands in their deformed morphologies (Fig. 8.9b-d).

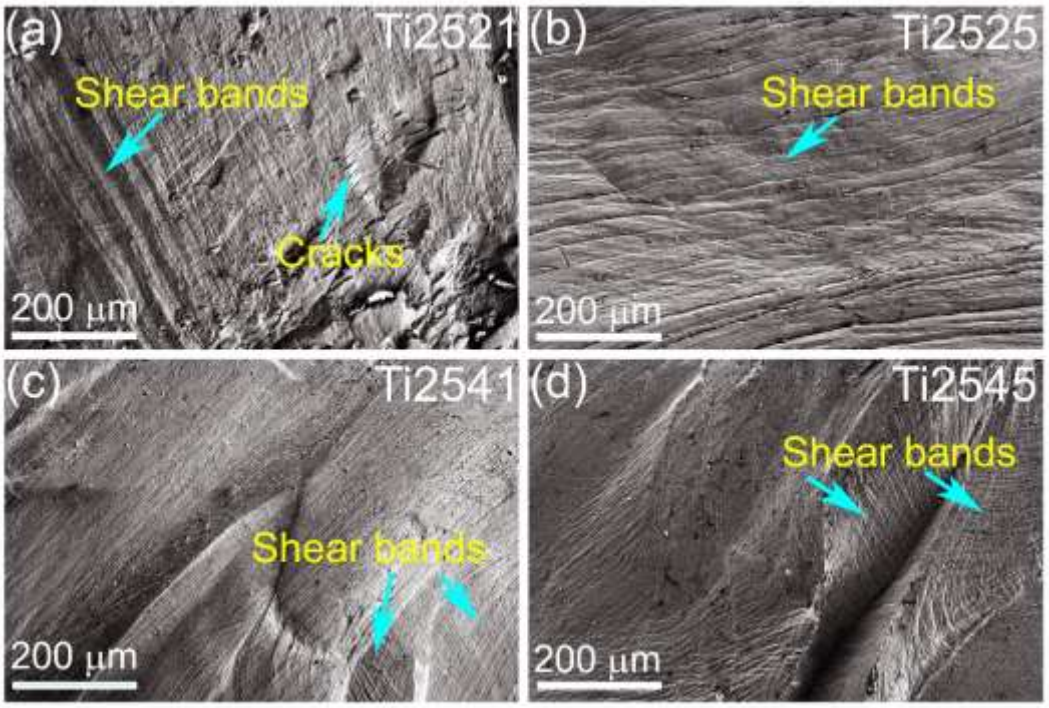

Fig. 8.9. The second electron SEM images of compressively deformed morphologies observed on the outer surface for all the Ti-25Nb-xMn-ySn (x = 2,4 wt% and y = 1,5 wt%) alloys (The alloys are designated as Ti25xy).

8.2. Conclusion

The present work investigates the microstructural features, phase constitution, static compressive and superelastic mechanical properties and deformation behavior for the newly designed Ti-25Nb-xMn-ySn (in wt.%; x = 2, 4 and y = 1, 5) alloys for biomedical implant applications. The following main conclusions can be made from this work:

- Microstructural and phase characterizations revealed that the Ti-25Nb-2Mn-1Sn alloy comprises a dual-phase microstructure (α"+β phases). By contrast, other alloys, i.e., Ti-25Nb-2Mn-5Sn, Ti-25Nb-4Mn-1Sn and Ti-25Nb-4Mn-5Sn, possess monolithic β phase.
- Static compression characterizations display that Ti-25Mn-2Mn-1Sn fails after attaining 41 ± 2.5 % plastic strain during compression testing. By contrast, the Ti-25Nb-2Mn-5Sn, Ti-25Nb-4Mn-1Sn and Ti-25Nb-4Mn-5Sn do not fail during compression testing even after the load reaches the load capacity of 100 kN.
- Ti-25Nb-4Mn-1Sn alloy exhibits the highest value of yield strength of 710 ± 35 MPa and the Ti-25Nb-2Mn-1Sn possesses the highest value of hardness i.e., 244 ± 6.3 HV among the Ti-25Nb-xMn-ySn alloys. Notably, yield strength is influenced by solid solution and grain boundary strengthening while hardness is affected by the amount of constituent phases in each alloy.
- The superelastic behaviors show that Ti-25Nb-4Mn-1Sn exhibits the maximum recoverable strain of 2.35 % and superelastic recovery ratio of 90 % during cyclic loading-unloading up to 3% strain level and demonstrates highest total energy absorption among the investigated Ti-25Nb-Mn-Sn alloys.
- Moreover, all the Ti-Nb-Mn-Sn alloys display shear bands while Ti-25Nb-2Mn-1Sn display shear bands as well as some cracks on the outer surface of compressively deformed morphologies.
- Based on the findings of this work, Ti-25Nb-4Mn-1Sn shows better blend of high yield strength, large plasticity, sufficient recoverable strain and high energy absorption provided that Ti-25Nb-4Mn-1Sn could be a promising material for biomedical implant applications.

9. Conclusion and future prospects

In this work, four new series of Ti-25Nb-8Zr-xCr, Ti-25Nb-xSn-yCr, Ti-26Nb-xZr-yMn and Ti-25Nb-xMn-ySn alloys have been designed for biomedical implant applications based on the performance and cost parameters. Low-cost, abundant earth metals such as Cr, Mn and Sn have been employed in the investigated alloys in order to further enhance the performance of the designed alloys. The key concluding remarks from this work are summarized as below:

1. In Ti-25Nb-8Zr-xCr, the addition of Cr renders a dual phase α"+β dual-phase microstructure formed in Ti-25Nb-8Zr to a monolithic β phase formed in the alloys comprised of Cr. Both yield strength and hardness of the studied alloys increase due to the effect of solid-solution strengthening. By contrast, the plasticity, maximum strength and strain hardening rate are influenced by the β stability as well as the distinct deformation mechanisms. None of the alloys comprising Cr fail up to 100 kN (the load capacity used) and all show impressive plasticity (~75%) and superior maximum compressive strength (~ 4.5 GPa) at 100 kN. Both hardness (1.91 GPa to 2.63 GPa) and yield strength (382 MPa to 773 MPa) increase as the Cr concentration increases in the Ti-25Nb-8Zr-xCr alloys. Enhanced strain hardening rate ~ 5 GPa is achieved after addition of 2 wt% Cr in Ti-25Nb-8Zr alloy.

2. In Ti-25Nb-xSn-yCr alloys, all the investigated alloys display a monolithic β phase microstructure and exhibit high maximum strength (~ 5 GPa) as well as superior plasticity (~ 80 %, without failure even though the maximum load limit is reached at the load capacity of 100 kN). Ti-25Nb-1Sn-2Cr displays the highest yield strength (463 ± 30 MPa), hardness (2.36 GPa) and lowest elastic modulus (66 GPa) among the Ti-25Nb-xSn-yCr alloys. Furthermore, Ti-25Nb-1Sn-2Cr possesses the higher values of wear resistance indices (i.e. H/E and H^3/E_{eff}^2) as compared to CP-Ti and Ti64.

3. All the Ti-26Nb-xZr-yMn alloys illustrate a monolithic β phase in their microstructure and they all possess substantial true plasticity (~ 160%) and true maximum strength (~ 950 MPa) without fracture during the compression tests within the load capacity of 100 kN. The contribution of solid-solution, grain-boundary and dislocation strengthening mechanisms has been evaluated using the strengthening model for β Ti alloys for all the investigated alloys. Among the investigated alloys, Ti-26Nb-4Zr-5Mn demonstrates the

highest true yield strength (654 MPa), dislocation density (2.45×10^{15} m^{-2}) and hardness (242 HV) along with improved strain hardening ability in terms of strain hardening indices (0.42 and 0.09). Furthermore, based on the superior mechanical properties among the investigated alloys, the electrochemical performance of Ti-26Nb-4Zr-3Mn and Ti-26Nb-4Zr-5Mn has also been analyzed in this work. The electrochemical measurements show that both alloys have almost similar corrosion potential and corrosion current density in simulated body fluid, i.e., -0.45 V and 0.838 nA/cm^2 for Ti-26Nb-4Zr-3Mn, -0.48 V and 0.839 nA/cm^2 for Ti-26Nb-4Zr-5Mn, respectively.

4. Monolithic β phase is found in all Ti-25Nb-xMn-ySn alloys except in Ti-25Nb-2Mn-1Sn alloy which exhibits α"+β dual-phase microstructure. During compression testing, the Ti-25Nb-2Mn-1Sn alloy fails and demonstrates sufficient plasticity of ~ 41% and ultimate compressive strength of ~ 1800 MPa, where other alloys do not fail within the load capacity of 100 kN. Among all the investigated alloys, Ti-25Nb-4Mn-1Sn alloy exhibits the highest yield strength (~ 710 MPa) while Ti-25Nb-2Mn-1Sn alloy possesses the highest hardness (~ 244 HV). In this work, yield strength is influenced by solid solution and grain boundary strengthening while hardness is affected by the amount of constituent phases in each alloy. Additionally, Ti-25Nb-4Mn-1Sn shows the highest recoverable strain (2.35%) and superelastic recovery ratio (90%) during cyclic loading-unloading up to 3% strain level, with the highest total energy absorption among the investigated alloys.

5. The predicted deformation mechanisms based on deformation bands investigated around micro-hardness indentations, $\overline{Bo}$-$\overline{Md}$ diagram and $\overline{e/a}$-$\overline{\Delta r}$ diagram are in line with each other for theTi-25Nb-8Zr-xCr and Ti-25Nb-xSn-yCr alloys.

6. The results of deformation analysis after compression testing demonstrate the formation of shear bands, cracks and dimples for Ti-25Nb-8Zr-xCr, Ti-25Nb-xSn-yCr and Ti-25Nb-xMn-ySn. The alloys that failed during compression testing displayed some cracks, by contrast those that did not fail during compression testing demonstrated excessive shear bands and dimples formation on their deformed morphology.

7. Based on the results achieved in this work, it can be concluded that Ti-25Nb-8Zr-4Cr, Ti-25Nb-1Sn-2Cr, Ti-26Nb-4Zr-5Mn and Ti-25Nb-4Mn-1Sn alloys demonstrate a good blend of desired properties for orthopedic implant application.

This PhD study answers all the research questions presented for this thesis. However, while investigating the microstructure, mechanical properties and corrosion resistance are of critical importance for developing new generation of Ti alloys for orthopedic implant applications, further investigations to study other properties and/or further improve the performance of alloys are still required. The recommendations for some future work are summarized as below:

1. Investigating biocompatibility via cell culturing of the designed alloys and comparing the performance with those of Ti-6Al-4V and CP-Ti, as biocompatibility tests are of crucial importance for the suitability of designed alloys in orthopedic implant applications.

2. Investigating the tensile mechanical properties of designed alloys as tensile mechanical properties are supposed to be more reliable than compressive mechanical properties.
3. Studying the fatigue properties of designed alloys and investigating the effects of Cr, Mn, Sn and Zr on fatigue strength of Ti-Nb and compare the performance with that of Ti-6Al-4V and CP-Ti.

4. Producing the porous structure of designed alloys through different production methods such as spark plasma sintering and selective laser melting in order to further enhance the mechanical performance of the deigned alloys.

5. Employ some heat treatment and work hardening process such as solution treatment, aging, forging, cold rolling and hot rolling etc to further enhance the mechanical performance of the designed alloys.

Page deliberately left blank

References

[1] N. Manam, W. Harun, D. Shri, S. Ghani, T. Kurniawan, M. Ismail, M. Ibrahim, Study of corrosion in biocompatible metals for implants: A review, *J. Alloys Compd.* 701 **(2017)** 698-715. https://doi.org/10.1016/j.jallcom.2017.01.196.

[2] L. Kunčická, R. Kocich, T.C. Lowe, Advances in metals and alloys for joint replacement, *Prog. Mater. Sci.* 88 **(2017)** 232-280. https://doi.org/10.1016/j.pmatsci.2017.04.002.

[3] Q. Chen, G.A. Thouas, Metallic implant biomaterials, *Mater. Sci. Eng. R Rep.* 87 **(2015)** 1-57. https://doi.org/10.1016/j.mser.2014.10.001.

[4] M. Kaur, K. Singh, Review on titanium and titanium based alloys as biomaterials for orthopaedic applications, *Mater. Sci. Eng. C* 102 **(2019)** 844-862. https://doi.org/10.1016/j.msec.2019.04.064.

[5] M.Z. Ibrahim, A.A. Sarhan, F. Yusuf, M. Hamdi, Biomedical materials and techniques to improve the tribological, mechanical and biomedical properties of orthopedic implants–A review article, *J. Alloys Compd.* 714 **(2017)** 636-667. https://doi.org/10.1016/j.jallcom.2017.04.231.

[6] L.-C. Zhang, L.-Y. Chen, L. Wang, Surface Modification of Titanium and Titanium Alloys: Technologies, Developments, and Future Interests, *Adv. Eng. Mater.* 22 **(2020)** 1901258. https://doi.org/10.1002/adem.201901258.

[7] L. Zhang, L.Y. Chen, A review on biomedical titanium alloys: recent progress and prospect, *Adv. Eng. Mater.* 21 **(2019)** 1801215. https://doi.org/10.1002/adem.201801215.

[8] N. Dai, L.-C. Zhang, J. Zhang, X. Zhang, Q. Ni, Y. Chen, M. Wu, C. Yang, Distinction in corrosion resistance of selective laser melted Ti-6Al-4V alloy on different planes, *Corros. Sci.* 111 **(2016)** 703-710. https://doi.org/10.1016/j.corsci.2016.06.009.

[9] W.D. Callister, Fundamentals of materials science and engineering, seventh ed., John Wiley & Sons. Inc., New York, **2007**.

[10] L. Zhang, Y. Liu, S. Li, Y. Hao, Additive manufacturing of titanium alloys by electron beam melting: A review, *Adv. Eng. Mater.* 20 **(2018)** 1700842. https://doi.org/10.1002/adem.201700842.

[11] S.F. Jawed, C.D. Rabadia, Y.J. Liu, L.Q. Wang, Y.H. Li, X.H. Zhang, L.C. Zhang, Beta-type Ti-Nb-Zr-Cr alloys with large plasticity and significant strain hardening, *Mater. Des.* 181 **(2019)** 108064. https://doi.org/10.1016/j.matdes.2019.108064.

[12] P. Yadav, K.K. Saxena, Effect of heat-treatment on microstructure and mechanical properties of Ti alloys: An overview, *Mater. Today: Proc.* **(2020)** https://doi.org/10.1016/j.matpr.2020.02.541.

[13] C.D. Rabadia, Y.J. Liu, S.F. Jawed, L.Q. Wang, H. Sun, L.C. Zhang, Deformation and toughness behavior of β -type titanium alloys comprising C15-type Laves phase, *Mater. Today Sustainability* 9 **(2020)** 100034. https://doi.org/10.1016/j.mtsust.2020.100034.

[14] C.D. Rabadia, Y.J. Liu, L.Y. Chen, S.F. Jawed, L.Q. Wang, H. Sun, L.C. Zhang, Deformation and strength characteristics of Laves phases in titanium alloys, *Mater. Des.* 179 **(2019)** 107891. https://doi.org/10.1016/j.matdes.2019.107891.

[15] C.D. Rabadia, Y.J. Liu, L. Wang, H. Sun, L.C. Zhang, Laves phase precipitation in Ti-Zr-Fe-Cr alloys with high strength and large plasticity, *Mater. Des.* 154 **(2018)** 228-238. https://doi.org/10.1016/j.matdes.2018.05.035.

[16] R.P. Kolli, W.J. Joost, S. Ankem, Phase Stability and Stress-Induced Transformations in Beta Titanium Alloys, *JOM* 67 **(2015)** 1273-1280. https://doi.org/10.1007/s11837-015-1411-y.
[17] A. Ramezannejad, W. Xu, W.L. Xiao, K. Fox, D. Liang, M. Qian, New insights into nickel-free superelastic titanium alloys for biomedical applications, *Curr. Opin. Solid State Mater. Sci.* 23 **(2019)** 100783. https://doi.org/10.1016/j.cossms.2019.100783.
[18] C.H. Wang, A.M. Russell, G.H. Cao, A semi-empirical approach to the prediction of deformation behaviors of β-Ti alloys, *Scr. Mater.* 158 **(2019)** 62-65. https://doi.org/10.1016/j.scriptamat.2018.08.035.
[19] M. Abdel-Hady, K. Hinoshita, M. Morinaga, General approach to phase stability and elastic properties of β-type Ti-alloys using electronic parameters, *Scr. Mater.* 55 **(2006)** 477-480. https://doi.org/10.1016/j.scriptamat.2006.04.022.
[20] S.F. Jawed, C.D. Rabadia, Y.J. Liu, L.Q. Wang, Y.H. Li, X.H. Zhang, L.C. Zhang, Mechanical characterization and deformation behavior of β-stabilized Ti-Nb-Sn-Cr alloys, *J. Alloys Compd.* 792 **(2019)** 684-693. https://doi.org/10.1016/j.jallcom.2019.04.079.
[21] H. Yu, M. Yan, J. Li, A.R. Godbole, C. Lu, K. Tieu, H. Li, C. Kong, Mechanical properties and microstructure of a Ti-6Al-4V alloy subjected to cold rolling, asymmetric rolling and asymmetric cryorolling, *Mat. Sci. Eng. A-Struct.* 710 **(2018)** 10-16. https://doi.org/10.1016/J.MSEA.2017.10.075.
[22] F.d.F. Quadros, P.A.B. Kuroda, K.d.S.J. Sousa, T.A.G. Donato, C.R. Grandini, Preparation, structural and microstructural characterization of Ti-25Ta-10Zr alloy for biomedical applications, *J. Mater. Res. Technol.* 8 **(2019)** 4108-4114. https://doi.org/10.1016/j.jmrt.2019.07.020.
[23] Y.J. Liu, H.L. Wang, S.J. Li, S.G. Wang, W.J. Wang, W.T. Hou, Y.L. Hao, R. Yang, L.C. Zhang, Compressive and fatigue behavior of beta-type titanium porous structures fabricated by electron beam melting, *Acta Mater.* 126 **(2017)** 58-66. https://doi.org/10.1016/j.actamat.2016.12.052.
[24] N. Soro, H. Attar, E. Brodie, M. Veidt, A. Molotnikov, M.S. Dargusch, Evaluation of the mechanical compatibility of additively manufactured porous Ti–25Ta alloy for load-bearing implant applications, *J. Mech. Behav. Biomed. Mater.* 97 **(2019)** 149-158. https://doi.org/10.1016/j.jmbbm.2019.05.019.
[25] Y.J. Liu, D.C. Ren, S.J. Li, H. Wang, L.C. Zhang, T.B. Sercombe, Enhanced fatigue characteristics of a topology-optimized porous titanium structure produced by selective laser melting, *Addit. Manuf.* 32 **(2020)** 101060. https://doi.org/10.1016/j.addma.2020.101060.
[26] S. Bahl, S. Suwas, K. Chatterjee, Comprehensive review on alloy design, processing, and performance of β Titanium alloys as biomedical materials, *Int. Mater. Rev.* **(2020)** 1-26. https://doi.org/10.1080/09506608.2020.1735829.
[27] L. Wang, L. Xie, L.-C. Zhang, L. Chen, Z. Ding, Y. Lv, W. Zhang, W. Lu, D. Zhang, Microstructure evolution and superelasticity of layer-like NiTiNb porous metal prepared by eutectic reaction, *Acta Mater.* 143 **(2018)** 214-226. https://doi.org/10.1016/j.actamat.2017.10.021.
[28] L. Wang, C. Wang, L.-C. Zhang, L. Chen, W. Lu, D. Zhang, Phase transformation and deformation behavior of NiTi-Nb eutectic joined NiTi wires, *Sci. Rep.* 6 **(2016)** 23905. https://doi.org/10.1038/srep23905.

[29] H.Z. Lu, C. Yang, X. Luo, H.W. Ma, B. Song, Y.Y. Li, L.-C. Zhang, Ultrahigh-performance TiNi shape memory alloy by 4D printing, *Mater. Sci. Eng. A* 763 **(2019)** 138166. https://doi.org/10.1016/j.msea.2019.138166.
[30] Y. Al-Zain, A. Yamamoto, J.M. AlAjlouni, M.A. Al-Abbadi, M.R. Al-Sayyed, A.S. Aloweidi, H.Y. Kim, S. Miyazaki, Corrosion behavior, in vitro and in vivo biocompatibility of a newly developed Ti–16Nb–3Mo–1Sn superelastic alloy, *Mater. Sci. Eng. C* 104 **(2019)** 109906. https://doi.org/10.1016/j.msec.2019.109906.
[31] E. Frutos, M. Karl ík, J.A. Jim énez, H. Langhansov á, J. Lieskovsk á, T. Polcar, Development of new β/α″-Ti-Nb-Zr biocompatible coating with low Young's modulus and high toughness for medical applications, *Mater. Des.* 142 **(2018)** 44-55. https://doi.org/10.1016/j.matdes.2018.01.014.
[32] C. Baker, The Shape-Memory Effect in a Titanium-35 wt.-% Niobium Alloy, *Met. Sci. J.* 5 **(1971)** 92-100. https://doi.org/10.1179/030634571790439658.
[33] H.Y. Kim, Y. Ikehara, J.I. Kim, H. Hosoda, S. Miyazaki, Martensitic transformation, shape memory effect and superelasticity of Ti–Nb binary alloys, *Acta Mater.* 54 **(2006)** 2419-2429. https://doi.org/10.1016/j.actamat.2006.01.019.
[34] S. Li, Y.-w. Kim, M.-s. Choi, T.-h. Nam, Highly porous Ni-free Ti-based scaffolds with large recoverable strain for biomedical applications, *Intermetallics* 116 **(2020)** 106657. https://doi.org/10.1016/j.intermet.2019.106657.
[35] S. Li, T.-h. Nam, Superelasticity and tensile strength of Ti-Zr-Nb-Sn alloys with high Zr content for biomedical applications, *Intermetallics* 112 **(2019)** 106545. https://doi.org/10.1016/j.intermet.2019.106545.
[36] S.F. Jawed, Y.J. Liu, J.C. Wang, C.D. Rabadia, L.Q. Wang, Y.H. Li, X.H. Zhang, L.C. Zhang, Tailoring deformation and superelastic behaviors of beta-type Ti-Nb-Mn-Sn alloys, *J. Mech. Behav. Biomed. Mater.* 110 **(2020)** 103867. https://doi.org/10.1016/j.jmbbm.2020.103867.
[37] M. Niinomi, C.J. Boehlert, Titanium Alloys for Biomedical Applications, in: M. Niinomi, T. Narushima, M. Nakai (Eds.) Advances in Metallic Biomaterials: Tissues, Materials and Biological Reactions, Springer Berlin Heidelberg, Berlin, Heidelberg, **2015**, 179-213. https://doi.org/10.1007/978-3-662-46836-4_8.
[38] M. Motyka, K. Kubiak, J. Sieniawski, W. Ziaja, 2.02 - Phase Transformations and Characterization of α + β Titanium Alloys, in: S. Hashmi, G.F. Batalha, C.J. Van Tyne, B. Yilbas (Eds.) Comprehensive Materials Processing, Elsevier, Oxford, **2014**, 7-36. https://doi.org/10.1016/B978-0-08-096532-1.00202-8.
[39] R.P. Kolli, A. Devaraj, A review of metastable beta titanium alloys, *Met.* 8 **(2018)** 506. https://doi.org/10.3390/met8070506.
[40] C.D. Rabadia, Y.J. Liu, G.H. Cao, Y.H. Li, C.W. Zhang, T.B. Sercombe, H. Sun, L.C. Zhang, High-strength β stabilized Ti-Nb-Fe-Cr alloys with large plasticity, *Mater. Sci. Eng. A* 732 **(2018)** 368-377. https://doi.org/10.1016/j.msea.2018.07.031.
[41] S.F. Jawed, C.D. Rabadia, Y.J. Liu, L.Q. Wang, P. Qin, Y.H. Li, X.H. Zhang, L.C. Zhang, Strengthening mechanism and corrosion resistance of beta-type Ti-Nb-Zr-Mn alloys, *Mater. Sci. Eng. C* 110 **(2020)** 110728. https://doi.org/10.1016/j.msec.2020.110728.
[42] C.D. Rabadia, Y.J. Liu, S.F. Jawed, L. Wang, Y.H. Li, X.H. Zhang, T.B. Sercombe, H. Sun, L.C. Zhang, Improved deformation behavior in Ti-Zr-Fe-Mn alloys comprising the C14 type Laves and β phases, *Mater. Des.* 160 **(2018)** 1059-1070. https://doi.org/10.1016/j.matdes.2018.10.049.

[43] J. Park, R.S. Lakes, Biomaterials: an introduction, third ed., Springer-Verlag, New York, **2007**. https://doi.org/10.1007/978-0-387-37880-0.
[44] M. Geetha, A. Singh, R. Asokamani, A. Gogia, Ti based biomaterials, the ultimate choice for orthopaedic implants–a review, *Prog. Mater. Sci.* 54 **(2009)** 397-425. https://doi.org/10.1016/j.pmatsci.2008.06.004.
[45] G. Manivasagam, D. Dhinasekaran, A. Rajamanickam, Biomedical Implants: Corrosion and its Prevention-A Review, *Recent Pat. Corros. Sci.* 2 **(2010)** 40-54. https://doi.org/10.2174/1877610801002010040.
[46] S. Kurtz, K. Ong, E. Lau, F. Mowat, M. Halpern, Projections of primary and revision hip and knee arthroplasty in the United States from 2005 to 2030, *J. Bone Jt. Surg.* 89 **(2007)** 780-785. https://doi.org/10.2106/JBJS.F.00222.
[47] G. Giro, L. Chambrone, A. Goldstein, J.A. Rodrigues, E. Zenóbio, M. Feres, L.C. Figueiredo, A. Cassoni, J.A. Shibli, Impact of osteoporosis in dental implants: a systematic review, *World J. Orthop.* 6 **(2015)** 311. https://doi.org/10.5312/wjo.v6.i2.311.
[48] N.K. Paschos, Recent advances and future directions in the management of knee osteoarthritis: Can biological joint reconstruction replace joint arthroplasty and when?, *World J. Orthop.* 6 **(2015)** 655. https://doi.org/10.5312/wjo.v6.i9.655.
[49] H. Saleh, S. Yu, J. Vigdorchik, R. Schwarzkopf, Total knee arthroplasty for treatment of post-traumatic arthritis: Systematic review, *World J. Orthop.* 7 **(2016)** 584. https://doi.org/10.5312/wjo.v7.i9.584.
[50] United Nations, World Population Ageing Economic & social affairs, illustrated ed., New York, **2013**. https://doi.org/10.18356/e59eddca-en.
[51] R. Karre, S.R. Dey, Progress in Development of Beta Titanium Alloys for Biomedical Applications, in: S. Hashmi (Ed.) Reference Module in Materials Science and Materials Engineering, Elsevier, Amsterdam, Netherlands, **2019**. https://doi.org/10.1016/B978-0-12-803581-8.10501-6.
[52] R. Hugate, R. Holland, Handbook of Hip & Knee Joint Replacement: Through the Eyes of the Patient, Surgeon & Medical Team, first ed., CreateSpace Independent Publishing Platform, California,USA, **2012**.
[53] Total Hip Replacement Surgery (Hip Prosthesis), 2016. https://www.joint-surgeon.com/.
[54] Knee Replacement Market analysis by Top Player,Report, Trends, Sales, Share, Revenue Status & Forecast Period 2017-2023, 2018. https://www.medgadget.com/2018/06/page/19.
[55] W. Weng, A. Biesiekierski, Y. Li, C. Wen, Effects of selected metallic and interstitial elements on the microstructure and mechanical properties of beta titanium alloys for orthopedic applications, *Materialia* 6 **(2019)** 100323. https://doi.org/10.1016/j.mtla.2019.100323.
[56] M. Choroszyński, M.R. Choroszyński, S.J. Skrzypek, Biomaterials for hip implants–important considerations relating to the choice of materials, *Bio-Algorithms and Med-Systems* 13 **(2017)** 133-145. https://doi.org/10.1515/bams-2017-0017.
[57] V.S. de Viteri, E. Fuentes, Titanium and titanium alloys as biomaterials, in: J. Gegner (Ed.) Tribology-Fundamentals and advancements, IntechOpen, Rijeka, Croatia, **2013**, 155-181. https://doi.org/10.5772/55860.
[58] F. Barrère, T.A. Mahmood, K. de Groot, C.A. van Blitterswijk, Advanced biomaterials for skeletal tissue regeneration: Instructive and smart functions, *Mater. Sci. Eng. R Rep.* 59 **(2008)** 38-71. https://doi.org/10.1016/j.mser.2007.12.001.

[59] E. Eisenbarth, D. Velten, M. Müller, R. Thull, J. Breme, Biocompatibility of β-stabilizing elements of titanium alloys, *Biomaterials* 25 **(2004)** 5705-5713. https://doi.org/10.1016/j.biomaterials.2004.01.021.
[60] Y. Wang, Bioadaptability: an innovative concept for biomaterials, *J. Mater. Sci. Technol.* 32 **(2016)** 801-809. https://doi.org/10.1016/j.jmst.2016.08.002.
[61] S. Hanada, H. Matsumoto, S. Watanabe, Mechanical compatibility of titanium implants in hard tissues, *Int. Congr. Ser.* 1284 **(2005)** 239-247. https://doi.org/10.1016/j.ics.2005.06.084.
[62] M. Niinomi, T. Akahori, Improvement of the fatigue life of titanium alloys for biomedical devices through microstructural control, *Expert Rev. Med. Devices* 7 **(2010)** 481-488. https://doi.org/10.1586/erd.10.16
[63] D. Kuroda, M. Niinomi, M. Morinaga, Y. Kato, T. Yashiro, Design and mechanical properties of new β type titanium alloys for implant materials, *Mater. Sci. Eng. A* 243 **(1998)** 244-249. https://doi.org/10.1016/S0921-5093(97)00808-3.
[64] Y. Li, C. Yang, H. Zhao, S. Qu, X. Li, Y. Li, New developments of Ti-based alloys for biomedical applications, *Mater.* 7 **(2014)** 1709-1800. https://doi.org/10.3390/ma7031709.
[65] M. Calin, A. Gebert, A.C. Ghinea, P.F. Gostin, S. Abdi, C. Mickel, J. Eckert, Designing biocompatible Ti-based metallic glasses for implant applications, *Mater. Sci. Eng. C* 33 **(2013)** 875-883. https://doi.org/10.1016/j.msec.2012.11.015.
[66] M. Niinomi, Mechanical biocompatibilities of titanium alloys for biomedical applications, *J. Mech. Behav. Biomed. Mater.* 1 **(2008)** 30-42. https://doi.org/10.1016/j.jmbbm.2007.07.001.
[67] M. Niinomi, M. Nakai, J. Hieda, Development of new metallic alloys for biomedical applications, *Acta Biomater.* 8 **(2012)** 3888-3903. https://doi.org/10.1016/j.actbio.2012.06.037.
[68] J. Currey, Chapter A1 Cortical Bone, in: W. Murphy, J. Black, G. Hastings (Eds.) Handbook of Biomaterial Properties, Springer New York, New York, **2016**, 3-13. https://doi.org/10.1007/978-1-4939-3305-1_1.
[69] C.J. Hernandez, Chapter A2 Cancellous Bone, in: W. Murphy, J. Black, G. Hastings (Eds.) Handbook of Biomaterial Properties, Springer New York, New York, **2016**, 15-21. https://doi.org/10.1007/978-1-4939-3305-1_2.
[70] S.J. Hall, Basic Biomechanics, sixth ed., McGraw-Hill, New York, **2012**.
[71] R.C. Thomson, M.C. Wake, M.J. Yaszemski, A.G. Mikos, Biodegradable polymer scaffolds to regenerate organs, in: N.A. Peppas, R.S. Langer (Eds.) Biopolymers II, Springer Berlin Heidelberg, Berlin, Heidelberg, **1995**, 245-274. https://doi.org/10.1007/3540587888_18.
[72] A. Nouri, P.D. Hodgson, C.e. Wen, Biomimetic porous titanium scaffolds for orthopedic and dental applications, in: A. Mukherjee (Ed.) Biomimetics learning from nature, IntechOpen, Rijeka, Croatia, **2010**, 415-450. https://doi.org/10.5772/8787.
[73] F.G. Evans, Mechanical properties and histology of cortical bone from younger and older men, *Anat. Rec.* 185 **(1976)** 1-11. https://doi.org/10.1002/ar.1091850102.
[74] O. Lindahl, A.G. Lindgren, Cortical bone in man II. Variation in tensile strength with age and sex, *Acta Orthop. Scand.* 38 **(1967)** 141-147. https://doi.org/10.3109/17453676708989628.
[75] A.H. Burstein, D.T. Reilly, M. Martens, Aging of bone tissue: mechanical properties, *J. Bone Surg. Am.* 58 **(1976)** 82-86. https://doi.org/10.2106/00004623-197658010-00015.

[76] J.-Y. Rho, T.Y. Tsui, G.M. Pharr, Elastic properties of human cortical and trabecular lamellar bone measured by nanoindentation, *Biomaterials* 18 **(1997)** 1325-1330. https://doi.org/10.1016/S0142-9612(97)00073-2.
[77] O. Lindahl, Mechanical properties of dried defatted spongy bone, *Acta Orthop. Scand.* 47 **(1976)** 11-19. https://doi.org/10.3109/17453677608998966.
[78] M. Ding, M. Dalstra, C.C. Danielsen, J. Kabel, I. Hvid, F. Linde, Age variations in the properties of human tibial trabecular bone, *J. Bone Joint Surg. Br.* 79 **(1997)** 995-1002. https://doi.org/10.1302/0301-620X.79B6.0790995.
[79] C. Elias, J. Lima, R. Valiev, M. Meyers, Biomedical applications of titanium and its alloys, *JOM* 60 **(2008)** 46-49. https://doi.org/10.1007/s11837-008-0031-1.
[80] R. Asri, W. Harun, M. Samykano, N. Lah, S. Ghani, F. Tarlochan, M. Raza, Corrosion and surface modification on biocompatible metals: A review, *Mater. Sci. Eng. C* 77 **(2017)** 1261-1274. https://doi.org/10.1016/j.msec.2017.04.102.
[81] N. Eliaz, Corrosion of Metallic Biomaterials: A Review, *Mater.* 12 **(2019)** https://doi.org/10.3390/ma12030407.
[82] J.T. Scales, G.D. Winter, H.T. Shirley, Corrosion of orthopaedic implants, *J. Bone Joint Surg. Br.* 41-B **(1959)** 810-820. https://doi.org/10.1302/0301-620X.41B4.810.
[83] S. Affatato, D. Brando, 1 - Introduction to wear phenomena of orthopaedic implants, in: S. Affatato (Ed.) Wear of Orthopaedic Implants and Artificial Joints, Woodhead Publishing, **2013**, 3-26. https://doi.org/10.1533/9780857096128.1.3.
[84] V.K. Balla, M. Das, G. Manivasagam, Current advances in enhancement of wear and corrosion resistance of titanium alloys–a review, *Mater. Technol.* 31 **(2016)** 696-704. https://doi.org/10.1080/10667857.2016.1212780.
[85] J. Pellier, J. Geringer, B. Forest, Fretting-corrosion between 316L SS and PMMA: Influence of ionic strength, protein and electrochemical conditions on material wear. Application to orthopaedic implants, *Wear* 271 **(2011)** 1563-1571. https://doi.org/10.1016/j.wear.2011.01.082.
[86] M. Navarro, A. Michiardi, O. Castano, J. Planell, Biomaterials in orthopaedics, *J. R. Soc. Interface* 5 **(2008)** 1137-1158. https://doi.org/10.1098/rsif.2008.0151.
[87] W. Khan, M. Kapoor, N. Kumar, Covalent attachment of proteins to functionalized polypyrrole-coated metallic surfaces for improved biocompatibility, *Acta Biomater.* 3 **(2007)** 541-549. https://doi.org/10.1016/j.actbio.2007.01.006.
[88] C.M. Agrawal, Reconstructing the human body using biomaterials, *JOM* 50 **(1998)** 31-35. https://doi.org/10.1007/s11837-998-0064-5.
[89] H.R. Rezaie, L. Bakhtiari, A. Öchsner, Biomaterials and their applications, first ed., Springer International Publishing, Cham, Switzerland, **2015**. https://doi.org/10.1007/978-3-319-17846-2.
[90] M. Niinomi, Metals for biomedical devices, second ed., Woodhead publishing, Cambridge, United Kingdom, **2019**. https://doi.org/10.1016/c2017-0-03429-8
[91] E.N. Codaro, P. Melnikov, I. Ramires, A.C. Guastaldi, Corrosion behavior of a cobaltchromium-molybdenum alloy, *Russ. J. Electrochem.* 36 **(2000)** 1117-1121. https://doi.org/10.1007/BF02757531.
[92] L. Zhang, L. Wang, Microstructure and Mechanical Properties of Beta Type Ti-Fe Based Alloys, in: L. Zhang, L. Wang (Eds.) Development and Application of Biomedical Titanium Alloys, **2018**, 51-72. https://doi.org/10.2174/9781681086194118010005.
[93] R. Bolmaro, A.C. Parau, V. Pruna, M.A. Surmeneva, L.R. Constantin, M. Avalos, C.M. Cotrut, R. Tutuianu, M. Braic, D.V. Cojocaru, I. Dan, S. Croitoru, R.A. Surmenev, A.

Vladescu, Investigation of cast and annealed Ti25Nb10Zr alloy as material for orthopedic devices, *J. Mater. Res. Technol.* 8 **(2019)** 3399-3414. https://doi.org/10.1016/j.jmrt.2019.06.006.
[94] K. Wang, The use of titanium for medical applications in the USA, *Mater. Sci. Eng. A* 213 **(1996)** 134-137.
[95] S. Ozan, J. Lin, Y. Li, R. Ipek, C. Wen, Development of Ti–Nb–Zr alloys with high elastic admissible strain for temporary orthopedic devices, *Acta Biomater.* 20 **(2015)** 176-187. https://doi.org/10.1016/j.actbio.2015.03.023.
[96] F. Guillemot, F. Prima, R. Bareille, D. Gordin, T. Gloriant, M. Port é-Durrieu, D. Ansel, C. Baquey, Design of new titanium alloys for orthopaedic applications, *Med. Biol. Eng. Comput.* 42 **(2004)** 137-141. https://doi.org/10.1007/BF02351023.
[97] J.M. Cordeiro, V.A. Bar ão, Is there scientific evidence favoring the substitution of commercially pure titanium with titanium alloys for the manufacture of dental implants?, *Mater. Sci. Eng. C* 71 **(2017)** 1201-1215. https://doi.org/10.1016/j.msec.2016.10.025.
[98] A. Biesiekierski, J. Wang, M.A.-H. Gepreel, C. Wen, A new look at biomedical Ti-based shape memory alloys, *Acta Biomater.* 8 **(2012)** 1661-1669. https://doi.org/10.1016/j.actbio.2012.01.018.
[99] S.E. Haghighi, H. Lu, G. Jian, G. Cao, D. Habibi, L. Zhang, Effect of α ″martensite on the microstructure and mechanical properties of beta-type Ti–Fe–Ta alloys, *Mater. Des.* 76 **(2015)** 47-54. https://doi.org/10.1016/j.matdes.2015.03.028.
[100] P.S. Nnamchi, C. Obayi, I. Todd, M. Rainforth, Mechanical and electrochemical characterisation of new Ti–Mo–Nb–Zr alloys for biomedical applications, *J. Mech. Behav. Biomed. Mater.* 60 **(2016)** 68-77. https://doi.org/10.1016/j.jmbbm.2015.12.023.
[101] M. Balazic, J. Kopac, M.J. Jackson, W. Ahmed, Titanium and titanium alloy applications in medicine, *Int. J. Nano Biomater.* 1 **(2007)** 3-34. https://doi.org/10.1504/IJNBM.2007.016517.
[102] C. Veiga, J. Davim, A. Loureiro, Properties and applications of titanium alloys: a brief review, *Rev. Adv. Mater. Sci* 32 **(2012)** 133-148.
[103] M. Peters, J. Hemptenmacher, J. Kumpfert, C. Leyens, Structure and properties of titanium and titanium alloys, in: C. Leyens, M. Peters (Eds.) Titanium and titanium alloys: fundamentals and applications, Wiley-VCH, Weinheim, Germany, **2003**, 1-36. https://doi.org/10.1002/3527602119.ch1.
[104] A.T. Sidambe, Biocompatibility of advanced manufactured titanium implants—A review, *Mater.* 7 **(2014)** 8168-8188. https://doi.org/10.3390/ma7128168.
[105] Y. Oshida, Bioscience and Bioengineering of Titanium Materials, second ed., Elsevier, Oxford, United Kingdom, **2012**. https://doi.org/10.1016/C2011-0-07805-5.
[106] S. Mitragotri, J. Lahann, Physical approaches to biomaterial design, *Nat. Mater.* 8 **(2009)** 15-23. https://doi.org/10.1038/nmat2344.
[107] F.C. Campbell, Elements of metallurgy and engineering alloys, illustrated ed., ASM International, Materials Park, Ohio, **2008**. https://doi.org/10.31399/asm.tb.emea.9781627082518
[108] J.R. Davis, Handbook of materials for medical devices, first ed., ASM International, Materials Park, Ohio, **2003**. https://doi.org/10.1361/hrnrnd2003pl79.
[109] M. Niinomi, Mechanical properties of biomedical titanium alloys, *Mater. Sci. Eng. A* 243 **(1998)** 231-236. https://doi.org/10.1016/S0921-5093(97)00806-X.

[110] M. Schmidt, Space distribution and luminosity functions of quasi-stellar radio sources, *Astrophys. J.* 151 **(1968)** 393. https://doi.org/10.1086/149446.
[111] G. Lütjering, J. Williams, A. Gysler, Microstructure and mechanical properties of titanium alloys, in: J.C.M. Li (Ed.) Microstructure And Properties Of Materials: (Volume 2), World Scientific Publishing Company, Singapore, **2000**, 1-77. https://doi.org/10.1142/9789812793959_0001.
[112] W. Sha, S. Malinov, 1 - Introduction to titanium alloys, in: W. Sha, S. Malinov (Eds.) Titanium Alloys Modelling of Microstructure, Properties and Applications, Woodhead Publishing, Cambridge, United Kingdom, **2009**, 1-8. https://doi.org/10.1533/9781845695866.1.
[113] E. Collings, The physical metallurgy of titanium alloys, in: H.L. Gegel (Ed.) ASM series in metal processing ; 3., American Society for Metals, Cleveland, Metals Park, Ohio, **1984**.
[114] X. Lei, L. Dong, Z. Zhang, Y. Liu, Y. Hao, R. Yang, L.-C. Zhang, Microstructure, texture evolution and mechanical properties of VT3-1 titanium alloy processed by multi-pass drawing and subsequent isothermal annealing, *Met.* 7 **(2017)** 131. https://doi.org/10.3390/met7040131.
[115] A.R. McAndrew, P.A. Colegrove, C. Bühr, B.C.D. Flipo, A. Vairis, A literature review of Ti-6Al-4V linear friction welding, *Prog. Mater. Sci.* 92 **(2018)** 225-257. https://doi.org/10.1016/j.pmatsci.2017.10.003.
[116] J. Cohen, Biomaterials in orthopedic surgery, *Am. J. Surg.* 114 **(1967)** 31-41. https://doi.org/10.1016/0002-9610(67)90037-2.
[117] N. Dai, J. Zhang, Y. Chen, L.-C. Zhang, Heat Treatment Degrading the Corrosion Resistance of Selective Laser Melted Ti-6Al-4V Alloy, *J. Electrochem. Soc.* 164 **(2017)** C428-C434. https://doi.org/10.1016/10.1149/2.1481707jes.
[118] Y. Bai, X. Gai, S. Li, L.-C. Zhang, Y. Liu, Y. Hao, X. Zhang, R. Yang, Y. Gao, Improved corrosion behaviour of electron beam melted Ti-6Al–4V alloy in phosphate buffered saline, *Corros. Sci.* 123 **(2017)** 289-296. https://doi.org/10.1016/j.corsci.2017.05.003.
[119] R. Narayan, Biomedical materials, first ed., Springer-Verlag USA, **2009**. https://doi.org/10.1007/978-0-387-84872-3.
[120] S. Ehtemam-Haghighi, H.B. Lu, G.Y. Jian, G.H. Cao, D. Habibi, L.C. Zhang, Effect of α″martensite on the microstructure and mechanical properties of beta-type Ti–Fe–Ta alloys, *Mater. Des.* 76 **(2015)** 47-54. https://doi.org/10.1016/j.matdes.2015.03.028.
[121] B.D. Venkatesh, D.L. Chen, S.D. Bhole, Effect of heat treatment on mechanical properties of Ti–6Al–4V ELI alloy, *Mater. Sci. Eng. A* 506 **(2009)** 117-124. https://doi.org/10.1016/j.msea.2008.11.018.
[122] R. Pederson, **2002**, Microstructure and phase transformation of Ti-6Al-4V, Licentiate thesis, comprehensive summary, Luleå University of Technology, Luleå, Sweden, 31. http://urn.kb.se/resolve?urn=urn:nbn:se:ltu:diva-18361.
[123] Y.S. Zhang, J.J. Hu, W. Zhang, S. Yu, Z.T. Yu, Y.Q. Zhao, L.-C. Zhang, Discontinuous core-shell structured Ti-25Nb-3Mo-3Zr-2Sn alloy with high strength and good plasticity, *Mater. Charact.* 147 **(2019)** 127-130. https://doi.org/10.1016/j.matchar.2018.10.021.
[124] J.-R. Chen, W.-T. Tsai, In situ corrosion monitoring of Ti–6Al–4V alloy in H2SO4/HCl mixed solution using electrochemical AFM, *Electrochim. Acta* 56 **(2011)** 1746-1751. https://doi.org/10.1016/j.electacta.2010.10.024.

[125] M.A.-H. Gepreel, Texturing tendency in β-type Ti-alloys, in: P. Wilson (Ed.) Recent Developments in the Study of Recrystallization, IntechOpen, Rijeka, Croatia, **2013**. https://doi.org/10.5772/53588.
[126] M. Long, H.J. Rack, Titanium alloys in total joint replacement—a materials science perspective, *Biomaterials* 19 **(1998)** 1621-1639. https://doi.org/10.1016/S0142-9612(97)00146-4.
[127] Y. Zheng, **2013**, Nucleation mechanisms of refined alpha microstructure in beta titanium alloys, The Ohio State University, United States, 236. https://ui.adsabs.harvard.edu/#abs/2013PhDT.....141Z/abstract.
[128] M. Niinomi, Y. Liu, M. Nakai, H. Liu, H. Li, Biomedical titanium alloys with Young's moduli close to that of cortical bone, *Regen Biomater* 3 **(2016)** 173-185. https://doi.org/10.1093/rb/rbw016.
[129] Y. Yang, G. Li, H. Wang, S. Wu, L. Zhang, Y. Li, K. Yang, Formation of zigzag-shaped {1 1 2}< 1 1 1> β mechanical twins in Ti–24.5 Nb–0.7 Ta–2 Zr–1.4 O alloy, *Scr. Mater.* 66 **(2012)** 211-214. https://doi.org/10.1016/j.scriptamat.2011.10.031.
[130] M. Nakai, M. Niinomi, X. Zhao, X. Zhao, Self-adjustment of Young's modulus in biomedical titanium alloys during orthopaedic operation, *Mater. Lett.* 65 **(2011)** 688-690. https://doi.org/10.1016/j.matlet.2010.11.006.
[131] P.F. Santos, M. Niinomi, H. Liu, K. Cho, M. Nakai, A. Trenggono, S. Champagne, H. Hermawan, T. Narushima, Improvement of microstructure, mechanical and corrosion properties of biomedical Ti-Mn alloys by Mo addition, *Mater. Des.* 110 **(2016)** 414-424. https://doi.org/10.1016/j.matdes.2016.07.115.
[132] S. El-Hadad, M. Nady, W. Khalifa, A. Shash, Influence of heat treatment conditions on the mechanical properties of Ti–6Al–4V alloy, *Can. Metall. Q.* 57 **(2018)** 186-193. https://doi.org/10.1080/00084433.2017.1412557.
[133] H. Rack, J. Qazi, Titanium alloys for biomedical applications, *Mater. Sci. Eng. C* 26 **(2006)** 1269-1277. https://doi.org/10.1016/j.msec.2005.08.032.
[134] M. Kikuchi, Y. Takada, S. Kiyosue, M. Yoda, M. Woldu, Z. Cai, O. Okuno, T. Okabe, Mechanical properties and microstructures of cast Ti–Cu alloys, *Dent. Mater.* 19 **(2003)** 174-181. https://doi.org/10.1016/S0109-5641(02)00027-1.
[135] R. Filip, K. Kubiak, W. Ziaja, J. Sieniawski, The effect of microstructure on the mechanical properties of two-phase titanium alloys, *J. Mater. Process. Technol.* 133 **(2003)** 84-89. https://doi.org/10.1016/S0924-0136(02)00248-0.
[136] L.L. Chang, Y.D. Wang, Y. Ren, In-situ investigation of stress-induced martensitic transformation in Ti–Nb binary alloys with low Young's modulus, *Mater. Sci. Eng. A* 651 **(2016)** 442-448. https://doi.org/10.1016/j.msea.2015.11.005.
[137] S. Cai, L. Wang, J.E. Schaffer, J. Gao, Y. Ren, Influence of Sn on martensitic beta Ti alloys, *Mater. Sci. Eng. A* 743 **(2019)** 764-772. https://doi.org/10.1016/j.msea.2018.11.095.
[138] Z. Chen, Y. Liu, H. Jiang, M. Liu, C. Wang, G. Cao, Microstructures and mechanical properties of Mn modified, Ti-Nb-based alloys, *J. Alloys Compd.* 723 **(2017)** 1091-1097. https://doi.org/10.1016/j.jallcom.2017.06.311.
[139] S. Ehtemam-Haghighi, Y.J. Liu, G.H. Cao, L.-C. Zhang, Phase transition, microstructural evolution and mechanical properties of Ti-Nb-Fe alloys induced by Fe addition, *Mater. Des.* 97 **(2016)** 279-286. https://doi.org/10.1016/j.matdes.2016.02.094.
[140] S. Ehtemam-Haghighi, Y.J. Liu, G.H. Cao, L.C. Zhang, Influence of Nb on the β→ α ″martensitic phase transformation and properties of the newly designed Ti–Fe–Nb

alloys, *Mater. Sci. Eng. C* 60 **(2016)** 503-510. https://doi.org/10.1016/j.msec.2015.11.072.
[141] F.A. Shah, M. Trobos, P. Thomsen, A. Palmquist, Commercially pure titanium (cp-Ti) versus titanium alloy (Ti6Al4V) materials as bone anchored implants—Is one truly better than the other?, *Mater. Sci. Eng. C* 62 **(2016)** 960-966. https://doi.org/10.1016/j.msec.2016.01.032.
[142] S. Ozan, J. Lin, Y. Li, C. Wen, New Ti-Ta-Zr-Nb alloys with ultrahigh strength for potential orthopedic implant applications, *J. Mech. Behav. Biomed. Mater.* 75 **(2017)** 119-127. https://doi.org/10.1016/j.jmbbm.2017.07.011.
[143] C. Lan, Y. Wu, L. Guo, F. Chen, Effects of cold rolling on microstructure, texture evolution and mechanical properties of Ti-32.5 Nb-6.8 Zr-2.7 Sn-0.3 O alloy for biomedical applications, *Mater. Sci. Eng. A* 690 **(2017)** 170-176. https://doi.org/10.1016/j.msea.2017.02.045.
[144] I. Okulov, A. Volegov, H. Attar, M. Bönisch, S. Ehtemam-Haghighi, M. Calin, J. Eckert, Composition optimization of low modulus and high-strength TiNb-based alloys for biomedical applications, *J. Mech. Behav. Biomed. Mater.* 65 **(2017)** 866-871. https://doi.org/10.1016/j.jmbbm.2016.10.013.
[145] A. Biesiekierski, J. Lin, Y. Li, D. Ping, Y. Yamabe-Mitarai, C. Wen, Investigations into Ti–(Nb, Ta)–Fe alloys for biomedical applications, *Acta Biomater.* 32 **(2016)** 336-347. https://doi.org/10.1016/j.actbio.2015.12.010.
[146] V. Sheremetyev, V. Brailovski, S. Prokoshkin, K. Inaekyan, S. Dubinskiy, Functional fatigue behavior of superelastic beta Ti-22Nb-6Zr (at%) alloy for load-bearing biomedical applications, *Mater. Sci. Eng. C* 58 **(2016)** 935-944. https://doi.org/10.1016/j.msec.2015.09.060.
[147] J.-W. Kim, M.-J. Hwang, M.-K. Han, Y.-G. Kim, H.-J. Song, Y.-J. Park, Effect of manganese on the microstructure, mechanical properties and corrosion behavior of titanium alloys, *Mater. Chem. Phys.* 180 **(2016)** 341-348. https://doi.org/10.1016/j.matchemphys.2016.06.016.
[148] M.W. Mendes, C.G. Ágreda, A.H. Bressiani, J.C. Bressiani, A new titanium based alloy Ti–27Nb–13Zr produced by powder metallurgy with biomimetic coating for use as a biomaterial, *Mater. Sci. Eng. C* 63 **(2016)** 671-677. https://doi.org/10.1016/j.msec.2016.03.052.
[149] S. Ehtemam-Haghighi, K. Prashanth, H. Attar, A.K. Chaubey, G.H. Cao, L.C. Zhang, Evaluation of mechanical and wear properties of TixNb7Fe alloys designed for biomedical applications, *Mater. Des.* 111 **(2016)** 592-599. https://doi.org/10.1016/j.matdes.2016.09.029.
[150] J. Lin, S. Ozan, Y. Li, D. Ping, X. Tong, G. Li, C. Wen, Novel Ti-Ta-Hf-Zr alloys with promising mechanical properties for prospective stent applications, *Sci. Rep.* 6 **(2016)** 37901. https://doi.org/10.1038/srep37901.
[151] A. Biesiekierski, J. Lin, Y. Li, D. Ping, Y. Yamabe-Mitarai, C. Wen, Impact of ruthenium on mechanical properties, biological response and thermal processing of β-type Ti–Nb–Ru alloys, *Acta Biomater.* 48 **(2017)** 461-467. https://doi.org/10.1016/j.actbio.2016.09.012.
[152] A. Biesiekierski, D. Ping, Y. Li, J. Lin, K.S. Munir, Y. Yamabe-Mitarai, C. Wen, Extraordinary high strength Ti-Zr-Ta alloys through nanoscaled, dual-cubic spinodal reinforcement, *Acta Biomater.* 53 **(2017)** 549-558. https://doi.org/10.1016/j.actbio.2017.01.085.

[153] W. Cui, A. Guo, Microstructures and properties of biomedical TiNbZrFe β-titanium alloy under aging conditions, *Mater. Sci. Eng. A* 527 **(2009)** 258-262. https://doi.org/10.1016/j.msea.2009.08.057.
[154] S. Ozan, J. Lin, Y. Li, Y. Zhang, K. Munir, H. Jiang, C. Wen, Deformation mechanism and mechanical properties of a thermomechanically processed β Ti–28Nb–35.4 Zr alloy, *J. Mech. Behav. Biomed. Mater.* 78 **(2018)** 224-234. https://doi.org/10.1016/j.jmbbm.2017.11.025.
[155] N. Kamikawa, K. Sato, G. Miyamoto, M. Murayama, N. Sekido, K. Tsuzaki, T. Furuhara, Stress–strain behavior of ferrite and bainite with nano-precipitation in low carbon steels, *Acta Mater.* 83 **(2015)** 383-396. https://doi.org/10.1016/j.actamat.2014.10.010.
[156] X.X. Ye, B. Chen, J.H. Shen, J. Umeda, K. Kondoh, Microstructure and strengthening mechanism of ultrastrong and ductile Ti-xSn alloy processed by powder metallurgy, *J. Alloys Compd.* 709 **(2017)** 381-393. https://doi.org/10.1016/j.jallcom.2017.03.171.
[157] X.X. Ye, H. Imai, J.H. Shen, B. Chen, G.Q. Han, J. Umeda, M. Takahashi, K. Kondoh, Strengthening-toughening mechanism study of powder metallurgy Ti-Si alloy by interrupted in-situ tensile tests, *J. Alloys Compd.* 694 **(2017)** 82-92. https://doi.org/10.1016/j.jallcom.2016.09.319.
[158] J.Y. He, H. Wang, H.L. Huang, X.D. Xu, M.W. Chen, Y. Wu, X.J. Liu, T.G. Nieh, K. An, Z.P. Lu, A precipitation-hardened high-entropy alloy with outstanding tensile properties, *Acta Mater.* 102 **(2016)** 187-196. https://doi.org/10.1016/j.actamat.2015.08.076.
[159] G.H. Zhao, X.Z. Liang, B. Kim, P.E.J. Rivera-D ́ıaz-del-Castillo, Modelling strengthening mechanisms in beta-type Ti alloys, *Mater. Sci. Eng. A* 756 **(2019)** 156-160. https://doi.org/10.1016/j.msea.2019.04.027.
[160] M. Morinaga, 1.3 - The molecular orbital approach and its application to biomedical titanium alloy design, in: F.H. Froes, M. Qian (Eds.) Titanium in Medical and Dental Applications, Woodhead Publishing, Cambridge, United Kingdom, **2018**, 39-64. https://doi.org/10.1016/B978-0-12-812456-7.00003-2.
[161] Z. Feng, Y. Yang, Z. Xu, Q. Shi, Effect of Martensitic Transformation on Elastic Modulus Anisotropy of Ti-6Al-4V Alloy, *Mater. Res.* 21 **(2018)** https://doi.org/10.1590/1980-5373-mr-2018-0197
[162] M. Morishita, Y. Ashida, M. Chikuda, M. Morinaga, N. Yukawa, H. Adachi, Active Corrosion Rate for Ti-based Alloys in Aqueous Corrosion and Its Correlation with the Bond Order Obtained by Electron Theory, *ISIJ Int.* 31 **(1991)** 890-896. https://doi.org/10.2355/isijinternational.31.890.
[163] M. Morinaga, M. Kato, T. Kamimura, M. Fukumoto, I. Harada, K. Kubo, in: F.H. Froes, I.L. Caplan (Eds.) *Theoretical Design of β-type Titanium alloys*, Titanium '92, science and technology : proceedings of the Seventh International Conference on Titanium, Warrendale, Pa. : Metallurgical Society of AIME, San Diego, California, USA, I, June 29-July 2, **1992**, 276-283.
[164] S. Sadeghpour, S. Abbasi, M. Morakabati, A. Kisko, L. Karjalainen, D. Porter, On the compressive deformation behavior of new beta titanium alloys designed by d-electron method, *J. Alloys Compd.* 746 **(2018)** 206-217. https://doi.org/10.1016/j.jallcom.2018.02.212.
[165] F. Sun, J.Y. Zhang, M. Marteleur, C. Brozek, E.F. Rauch, M. Veron, P. Vermaut, P.J. Jacques, F. Prima, A new titanium alloy with a combination of high strength, high strain

hardening and improved ductility, *Scr. Mater.* 94 **(2015)** 17-20. https://doi.org/10.1016/j.scriptamat.2014.09.005.
[166] Q. Wang, C. Han, T. Choma, Q. Wei, C. Yan, B. Song, Y. Shi, Effect of Nb content on microstructure, property and in vitro apatite-forming capability of Ti-Nb alloys fabricated via selective laser melting, *Mater. Des.* 126 **(2017)** 268-277. https://doi.org/10.1016/j.matdes.2017.04.026.
[167] B. Jiang, Q. Wang, D. Wen, F. Xu, G. Chen, C. Dong, L. Sun, P.K. Liaw, Effects of Nb and Zr on structural stabilities of Ti-Mo-Sn-based alloys with low modulus, *Mater. Sci. Eng. A* 687 **(2017)** 1-7. https://doi.org/10.1016/j.msea.2017.01.047.
[168] Y.L. Yang, W.Q. Wang, F.L. Li, W.Q. Li, Y.Q. Zhang, The Effect of Aluminum Equivalent and Molybdenum Equivalent on the Mechanical Properties of High Strength and High Toughness Titanium Alloys, *Mater. Sci. Forum* 618 **(2009)** 169-172. https://doi.org/10.4028/www.scientific.net/MSF.618-619.169.
[169] M. Ikeda, S.-y. Komatsu, Y. Nakamura, Effects of Sn and Zr additions on phase constitution and aging behavior of Ti-50 mass% Ta alloys quenched from β single phase region, *Mater Trans* 45 **(2004)** 1106-1112. https://doi.org/10.2320/matertrans.45.1106.
[170] N.T.C. Oliveira, G. Aleixo, R. Caram, A.C. Guastaldi, Development of Ti–Mo alloys for biomedical applications: Microstructure and electrochemical characterization, *Mater. Sci. Eng. A* 452-453 **(2007)** 727-731. https://doi.org/10.1016/j.msea.2006.11.061.
[171] K. Endoh, M. Tahara, T. Inamura, H. Hosoda, Effect of Sn and Zr content on superelastic properties of Ti-Mo-Sn-Zr biomedical alloys, *Mater. Sci. Eng. A* 704 **(2017)** 72-76. https://doi.org/10.1016/j.msea.2017.07.097.
[172] J. Málek, F. Hnilica, J. Veselý, B. Smola, K. Kolařík, J. Fojt, M. Vlach, V. Kodetová, The effect of Zr on the microstructure and properties of Ti-35Nb-XZr alloy, *Mater. Sci. Eng. A* 675 **(2016)** 1-10. https://doi.org/10.1016/j.msea.2016.07.069.
[173] J.C. Williams, B.S. Hickman, D.H. Leslie, The effect of ternary additions on the decompositon of metastable beta-phase titanium alloys, *Metall. Trans.* 2 **(1971)** 477-484. https://doi.org/10.1007/bf02663337
[174] H.-C. Hsu, S.-C. Wu, S.-K. Hsu, T.-F. Lin, W.-F. Ho, Structure and mechanical properties of as-cast Ti–5Nb–xCr alloys, *Mater. Des.* 51 **(2013)** 268-273. https://doi.org/10.1016/j.matdes.2013.04.001.
[175] P. Wang, Y. Feng, F. Liu, L. Wu, S. Guan, Microstructure and mechanical properties of Ti–Zr–Cr biomedical alloys, *Mater. Sci. Eng. C* 51 **(2015)** 148-152. https://doi.org/10.1016/j.msec.2015.02.028.
[176] J. Gao, Y. Huang, D. Guan, A.J. Knowles, L. Ma, D. Dye, W.M. Rainforth, Deformation mechanisms in a metastable beta titanium twinning induced plasticity alloy with high yield strength and high strain hardening rate, *Acta Mater.* 152 **(2018)** 301-314. https://doi.org/10.1016/j.actamat.2018.04.035.
[177] Q. Li, M. Niinomi, J. Hieda, M. Nakai, K. Cho, Deformation-induced ω phase in modified Ti–29Nb–13Ta–4.6 Zr alloy by Cr addition, *Acta Biomater.* 9 **(2013)** 8027-8035. https://doi.org/10.1016/j.actbio.2013.04.032.
[178] M. Bönisch, A. Panigrahi, M. Calin, T. Waitz, M. Zehetbauer, W. Skrotzki, J. Eckert, Thermal stability and latent heat of Nb–rich martensitic Ti-Nb alloys, *J. Alloys Compd.* 697 **(2017)** 300-309. https://doi.org/10.1016/j.jallcom.2016.12.108.
[179] Y.S. Kim, H.J. Park, J.T. Kim, S.H. Hong, G.H. Park, J.M. Park, J.Y. Suh, K.B. Kim, Influence of Nb on microstructure and mechanical properties of Ti-Sn ultrafine eutectic alloy, *Met. Mater. Int.* 23 **(2017)** 20-25. https://doi.org/10.1007/s12540-017-6263-2.

[180] L.H. Liu, C. Yang, L.M. Kang, Y. Long, Z.Y. Xiao, P.J. Li, L.C. Zhang, Equiaxed Ti-based composites with high strength and large plasticity prepared by sintering and crystallizing amorphous powder, *Mater. Sci. Eng. A* 650 **(2016)** 171-182. https://doi.org/10.1016/j.msea.2015.10.048.
[181] J. Ureña, E. Tabares, S. Tsipas, A. Jiménez-Morales, E. Gordo, Dry sliding wear behaviour of β-type Ti-Nb and Ti-Mo surfaces designed by diffusion treatments for biomedical applications, *J. Mech. Behav. Biomed. Mater.* 91 **(2019)** 335-344. https://doi.org/10.1016/j.jmbbm.2018.12.029.
[182] J. Ureña, S. Tsipas, A.M. Pinto, F. Toptan, E. Gordo, A. Jiménez-Morales, Corrosion and tribocorrosion behaviour of β-type Ti-Nb and Ti-Mo surfaces designed by diffusion treatments for biomedical applications, *Corros. Sci.* 140 **(2018)** 51-60. https://doi.org/10.1016/j.corsci.2018.06.024.
[183] X. Zhao, M. Niinomi, M. Nakai, J. Hieda, T. Ishimoto, T. Nakano, Optimization of Cr content of metastable β-type Ti–Cr alloys with changeable Young's modulus for spinal fixation applications, *Acta Biomater.* 8 **(2012)** 2392-2400. https://doi.org/10.1016/j.actbio.2012.02.010.
[184] J.J. Gutiérrez-Moreno, Y. Guo, K. Georgarakis, A.R. Yavari, G.A. Evangelakis, C.E. Lekka, The role of Sn doping in the β-type Ti–25at%Nb alloys: Experiment and ab initio calculations, *J. Alloys Compd.* 615 **(2014)** S676-S679. https://doi.org/10.1016/j.jallcom.2014.05.024.
[185] Y. Guo, K. Georgarakis, Y. Yokoyama, A.R. Yavari, On the mechanical properties of TiNb based alloys, *J. Alloys Compd.* 571 **(2013)** 25-30. https://doi.org/10.1016/j.jallcom.2013.03.192.
[186] K. Endoh, M. Tahara, T. Inamura, H. Hosoda, Effect of Sn and Zr addition on the martensitic transformation behavior of Ti-Mo shape memory alloys, *J. Alloys Compd.* 695 **(2017)** 76-82. https://doi.org/10.1016/j.jallcom.2016.10.108.
[187] P.F. Santos, M. Niinomi, K. Cho, M. Nakai, H. Liu, N. Ohtsu, M. Hirano, M. Ikeda, T. Narushima, Microstructures, mechanical properties and cytotoxicity of low cost beta Ti–Mn alloys for biomedical applications, *Acta Biomater.* 26 **(2015)** 366-376. https://doi.org/10.1016/j.actbio.2015.08.015.
[188] W.A. Rachinger, A "super-elastic" single crystal calibration bar, *Br. J. Appl.* 9 **(1958)** 250-252. https://doi.org/10.1088/0508-3443/9/6/308.
[189] W. Wang, X. Zhang, W. Mei, J. Sun, Role of omega phase evolution in plastic deformation of twinning-induced plasticity β Ti–12V–2Fe–1Al alloy, *Mater. Des.* 186 **(2020)** 108282. https://doi.org/10.1016/j.matdes.2019.108282.
[190] S. Liu, J. Liu, L. Wang, R.L.-W. Ma, Y. Zhong, W. Lu, L.-C. Zhang, Superelastic behavior of in-situ eutectic-reaction manufactured high strength 3D porous NiTi-Nb scaffold, *Scr. Mater.* 181 **(2020)** 121-126. https://doi.org/10.1016/j.scriptamat.2020.02.025.
[191] J.C. Wang, Y.J. Liu, P. Qin, S.X. Liang, T.B. Sercombe, L.C. Zhang, Selective laser melting of Ti–35Nb composite from elemental powder mixture: Microstructure, mechanical behavior and corrosion behavior, *Mater. Sci. Eng. A* 760 **(2019)** 214-224. https://doi.org/10.1016/j.msea.2019.06.001.
[192] V. Brailovski, S. Prokoshkin, M. Gauthier, K. Inaekyan, S. Dubinskiy, M. Petrzhik, M. Filonov, Bulk and porous metastable beta Ti–Nb–Zr(Ta) alloys for biomedical applications, *Mater. Sci. Eng. C* 31 **(2011)** 643-657. https://doi.org/10.1016/j.msec.2010.12.008.

[193] F. Sun, Y.L. Hao, S. Nowak, T. Gloriant, P. Laheurte, F. Prima, A thermo-mechanical treatment to improve the superelastic performances of biomedical Ti–26Nb and Ti–20Nb–6Zr (at.%) alloys, *J. Mech. Behav. Biomed. Mater.* 4 **(2011)** 1864-1872. https://doi.org/10.1016/j.jmbbm.2011.06.003.
[194] A. Morita, H. Fukui, H. Tadano, S. Hayashi, J. Hasegawa, M. Niinomi, Alloying titanium and tantalum by cold crucible levitation melting (CCLM) furnace, *Mater. Sci. Eng. A* 280 **(2000)** 208-213. https://doi.org/10.1016/S0921-5093(99)00668-1.
[195] L.C. Zhang, Z.Q. Shen, J. Xu, Glass formation in a (Ti, Zr, Hf)–(Cu, Ni, Ag)–Al high-order alloy system by mechanical alloying, *J. Mater. Res.* 18 **(2003)** 2141-2149. https://doi.org/10.1557/JMR.2003.0300.
[196] L.C. Zhang, J. Das, H.B. Lu, C. Duhamel, M. Calin, J. Eckert, High strength Ti–Fe–Sn ultrafine composites with large plasticity, *Scr. Mater.* 57 **(2007)** 101-104. https://doi.org/10.1016/j.scriptamat.2007.03.031.
[197] G.K. Williamson, R.E. Smallman, III. Dislocation densities in some annealed and cold-worked metals from measurements on the X-ray debye-scherrer spectrum, *Philos. Mag.* 1 **(1956)** 34-46. https://doi.org/10.1080/14786435608238074.
[198] R. Huang, Y. Han, The effect of SMAT-induced grain refinement and dislocations on the corrosion behavior of Ti–25Nb–3Mo–3Zr–2Sn alloy, *Mater. Sci. Eng. C* 33 **(2013)** 2353-2359. https://doi.org/10.1016/j.msec.2013.01.068.
[199] G.K. Williamson, W.H. Hall, X-ray line broadening from filed aluminium and wolfram, *Acta Metall.* 1 **(1953)** 22-31. https://doi.org/10.1016/0001-6160(53)90006-6.
[200] K. Bazzi, A. Rathi, V.M. Meka, R. Goswami, T.V. Jayaraman, Significant reduction in intrinsic coercivity of high-entropy alloy FeCoNiAl0.375Si0.375 comprised of supersaturated f.c.c. phase, *Materialia* 6 **(2019)** https://doi.org/10.1016/j.mtla.2019.100293.
[201] C.D. Rabadia, Y.J. Liu, C.H. Zhao, J.C. Wang, S.F. Jawed, L.Q. Wang, L.Y. Chen, H. Sun, L.C. Zhang, Improved trade-off between strength and plasticity in titanium based metastable beta type Ti-Zr-Fe-Sn alloys, *Mater. Sci. Eng. A* 766 **(2019)** 138340. https://doi.org/10.1016/j.msea.2019.138340.
[202] C. Brozek, F. Sun, P. Vermaut, Y. Millet, A. Lenain, D. Embury, P.J. Jacques, F. Prima, A β-titanium alloy with extra high strain-hardening rate: Design and mechanical properties, *Scr. Mater.* 114 **(2016)** 60-64. https://doi.org/10.1016/j.scriptamat.2015.11.020.
[203] D.R.N. Correa, F.B. Vicente, T.A.G. Donato, V.E. Arana-Chavez, M.A.R. Buzalaf, C.R. Grandini, The effect of the solute on the structure, selected mechanical properties, and biocompatibility of Ti–Zr system alloys for dental applications, *Mater. Sci. Eng. C* 34 **(2014)** 354-359. https://doi.org/10.1016/j.msec.2013.09.032.
[204] S. Liang, X. Feng, L. Yin, X. Liu, M. Ma, R. Liu, Development of a new β Ti alloy with low modulus and favorable plasticity for implant material, *Mater. Sci. Eng. C* 61 **(2016)** 338-343. https://doi.org/10.1016/j.msec.2015.12.076.
[205] Y.L. Zhou, M. Niinomi, T. Akahori, Effects of Ta content on Young's modulus and tensile properties of binary Ti–Ta alloys for biomedical applications, *Mater. Sci. Eng. A* 371 **(2004)** 283-290. https://doi.org/10.1016/j.msea.2003.12.011.
[206] W.-F. Ho, S.-C. Wu, S.-K. Hsu, Y.-C. Li, H.-C. Hsu, Effects of molybdenum content on the structure and mechanical properties of as-cast Ti–10Zr-based alloys for biomedical applications, *Mater. Sci. Eng. C* 32 **(2012)** 517-522. https://doi.org/10.1016/j.msec.2011.12.003.

[207] D.J. Lin, J.H. Chern Lin, C.P. Ju, Structure and properties of Ti–7.5Mo–xFe alloys, *Biomaterials* 23 **(2002)** 1723-1730. https://doi.org/10.1016/S0142-9612(01)00233-2.
[208] Y. Kusano, T. Inamura, H. Kanetaka, S. Miyazaki, H. Hosoda, Phase Constitution and Mechanical Properties of Ti-(Cr, Mn)-Sn Biomedical Alloys, *Mater. Sci. Forum* 654-656 **(2010)** 2118-2121. https://doi.org/10.4028/www.scientific.net/MSF.654-656.2118.
[209] S.-P. Wang, J. Xu, TiZrNbTaMo high-entropy alloy designed for orthopedic implants: As-cast microstructure and mechanical properties, *Mater. Sci. Eng. C* 73 **(2017)** 80-89. https://doi.org/10.1016/j.msec.2016.12.057.
[210] P. Zhang, S.X. Li, Z.F. Zhang, General relationship between strength and hardness, *Mater. Sci. Eng. A* 529 **(2011)** 62-73. https://doi.org/10.1016/j.msea.2011.08.061.
[211] J.S. Keist, T.A. Palmer, Development of strength-hardness relationships in additively manufactured titanium alloys, *Mater. Sci. Eng. A* 693 **(2017)** 214-224. https://doi.org/10.1016/j.msea.2017.03.102.
[212] Y. Yang, S. Wu, G. Li, Y. Li, Y. Lu, K. Yang, P. Ge, Evolution of deformation mechanisms of Ti–22.4 Nb–0.73 Ta–2Zr–1.34 O alloy during straining, *Acta Mater.* 58 **(2010)** 2778-2787. https://doi.org/10.1016/j.actamat.2010.01.015.
[213] M.J. Lai, T. Li, D. Raabe, ω phase acts as a switch between dislocation channeling and joint twinning- and transformation-induced plasticity in a metastable β titanium alloy, *Acta Mater.* 151 **(2018)** 67-77. https://doi.org/10.1016/j.actamat.2018.03.053.
[214] I. Gutierrez-Urrutia, D. Raabe, Dislocation and twin substructure evolution during strain hardening of an Fe–22wt.% Mn–0.6wt.% C TWIP steel observed by electron channeling contrast imaging, *Acta Mater.* 59 **(2011)** 6449-6462. https://doi.org/10.1016/j.actamat.2011.07.009.
[215] K.K. Chawla, M. Meyers, Mechanical behavior of materials, second ed., Prentice Hall Up. Saddle River, **1999**.
[216] Y.L. Hao, S.J. Li, S.Y. Sun, C.Y. Zheng, Q.M. Hu, R. Yang, Super-elastic titanium alloy with unstable plastic deformation, *Appl. Phys. Lett.* 87 **(2005)** 091906. https://doi.org/10.1063/1.2037192.
[217] M.J. Lai, C.C. Tasan, D. Raabe, On the mechanism of {332} twinning in metastable β titanium alloys, *Acta Mater.* 111 **(2016)** 173-186. https://doi.org/10.1016/j.actamat.2016.03.040.
[218] U. Ramamurty, S. Jana, Y. Kawamura, K. Chattopadhyay, Hardness and plastic deformation in a bulk metallic glass, *Acta Mater.* 53 **(2005)** 705-717. https://doi.org/10.1016/j.actamat.2004.10.023.
[219] A.L. Greer, Y.Q. Cheng, E. Ma, Shear bands in metallic glasses, *Materials Science and Engineering R* 74 **(2013)** 71-132. https://doi.org/10.1016/j.mser.2013.04.001.
[220] M.A. Meyers, G. Subhash, B.K. Kad, L. Prasad, Evolution of microstructure and shear-band formation in α-hcp titanium, *Mech. Mater.* 17 **(1994)** 175-193. https://doi.org/10.1016/0167-6636(94)90058-2.
[221] Y. Yang, X.M. Li, X.L. Tong, Q.M. Zhang, C.Y. Xu, Effects of microstructure on the adiabatic shearing behaviors of titanium alloy, *Mater. Sci. Eng. A* 528 **(2011)** 3130-3133. https://doi.org/10.1016/j.msea.2010.12.068.
[222] Y.L. Hao, S.J. Li, S.Y. Sun, R. Yang, Effect of Zr and Sn on Young's modulus and superelasticity of Ti–Nb-based alloys, *Mater. Sci. Eng. A* 441 **(2006)** 112-118. https://doi.org/10.1016/j.msea.2006.09.051.

[223] C. Lee, W. Ho, C.-P. Ju, J.C. Lin, Structure and properties of titanium–25 niobium–x iron alloys, *J. Mater. Sci. Mater. Med.* 13 **(2002)** 695-700. https://doi.org/10.1023/A:1015798011434.
[224] C. Lee, C.-P. Ju, J. Chern Lin, Structure–property relationship of cast Ti–Nb alloys, *J. Oral Rehabil.* 29 **(2002)** 314-322. https://doi.org/10.1046/j.1365-2842.2002.00825.x.
[225] Y. Xu, D. Zhang, Y. Zhou, W. Wang, X. Cao, Study on Topology Optimization Design, Manufacturability, and Performance Evaluation of Ti-6Al-4V Porous Structures Fabricated by Selective Laser Melting (SLM), *Mater.* 10 **(2017)** https://doi.org/10.3390/ma10091048.
[226] P.E.L. Moraes, R.J. Contieri, E.S.N. Lopes, A. Robin, R. Caram, Effects of Sn addition on the microstructure, mechanical properties and corrosion behavior of Ti–Nb–Sn alloys, *Mater. Charact.* 96 **(2014)** 273-281. https://doi.org/10.1016/j.matchar.2014.08.014.
[227] N. Okano, Y. Shinohara, Y. Kusano, M. Tahara, T. Inamura, S. Miyazaki, H. Hosoda, Effect of Sn Content on Phase Constitution and Mechanical Properties of Ti-Cr-Sn Shape Memory Alloys, *Mater. Today: Proc.* 2 **(2015)** S825-S828. https://doi.org/10.1016/j.matpr.2015.07.409.
[228] P. Sellappan, T. Rouxel, F. Celarie, E. Becker, P. Houizot, R. Conradt, Composition dependence of indentation deformation and indentation cracking in glass, *Acta Mater.* 61 **(2013)** 5949-5965. https://doi.org/10.1016/j.actamat.2013.06.034.
[229] P. Manda, U. Chakkingal, A.K. Singh, Hardness characteristic and shear band formation in metastable β-titanium alloys, *Mater. Charact.* 96 **(2014)** 151-157. https://doi.org/10.1016/j.matchar.2014.07.027.
[230] Y.J. Liu, Y.S. Zhang, L.C. Zhang, Transformation-induced plasticity and high strength in beta titanium alloy manufactured by selective laser melting, *Materialia* 6 **(2019)** 100299. https://doi.org/10.1016/j.mtla.2019.100299.
[231] J. Xu, G.d. Wang, X. Lu, L. Liu, P. Munroe, Z.-H. Xie, Mechanical and corrosion-resistant properties of Ti–Nb–Si–N nanocomposite films prepared by a double glow discharge plasma technique, *Ceram. Int.* 40 **(2014)** 8621-8630. https://doi.org/10.1016/j.ceramint.2014.01.079.
[232] S. Ehtemam-Haghighi, G.h. Cao, L.C. Zhang, Nanoindentation study of mechanical properties of Ti based alloys with Fe and Ta additions, *J. Alloys Compd.* 692 **(2017)** 892-897. https://doi.org/10.1016/j.jallcom.2016.09.123.
[233] H.Y. Kim, J. Fu, H. Tobe, J.I. Kim, S. Miyazaki, Crystal Structure, Transformation Strain, and Superelastic Property of Ti–Nb–Zr and Ti–Nb–Ta Alloys, *Shap. Mem. Superelasticity* 1 **(2015)** 107-116. https://doi.org/10.1007/s40830-015-0022-3.
[234] M.J. Bermingham, S.D. McDonald, M.S. Dargusch, D.H. StJohn, Grain-refinement mechanisms in titanium alloys, *J. Mater. Res.* 23 **(2008)** 97-104. https://doi.org/10.1557/JMR.2008.0002.
[235] S.J. Dai, Y. Wang, F. Chen, X.Q. Yu, Y.F. Zhang, Influence of Zr content on microstructure and mechanical properties of implant Ti–35Nb–4Sn–6Mo–xZr alloys, *T. Nonferr. Metal. Soc.* 23 **(2013)** 1299-1303. https://doi.org/10.1016/S1003-6326(13)62597-2.
[236] L.-C. Zhang, H.-B. Lu, C. Mickel, J. Eckert, Ductile ultrafine-grained Ti-based alloys with high yield strength, *Appl. Phys. Lett.* 91 **(2007)** 051906. https://doi.org/10.1063/1.2766861.

[237] M. Bönisch, M. Calin, J. van Humbeeck, W. Skrotzki, J. Eckert, Factors influencing the elastic moduli, reversible strains and hysteresis loops in martensitic Ti–Nb alloys, *Mater. Sci. Eng. C* 48 **(2015)** 511-520. https://doi.org/10.1016/j.msec.2014.12.048.
[238] J. Chakrabarty, Applied plasticity, second ed., Springer-Verlag, USA, **2000**. https://doi.org/10.1007/978-1-4757-3268-9.
[239] A. Shabani, M.R. Toroghinejad, A. Shafyei, P. Cavaliere, Effect of cold-rolling on microstructure, texture and mechanical properties of an equiatomic FeCrCuMnNi high entropy alloy, *Materialia* 1 **(2018)** 175-184. https://doi.org/10.1016/j.mtla.2018.06.004.
[240] L.A. Gypen, A. Deruyttere, The combination of atomic size and elastic modulus misfit interactions in solid solution hardening, *Scripta Metall.* 15 **(1981)** 815-820. https://doi.org/10.1016/0036-9748(81)90257-X.
[241] I. Toda-Caraballo, P.E.J. Rivera-Díaz-del-Castillo, Modelling solid solution hardening in high entropy alloys, *Acta Mater.* 85 **(2015)** 14-23. https://doi.org/10.1016/j.actamat.2014.11.014.
[242] L.A. Gypen, A. Deruyttere, Multi-component solid solution hardening, *J. Mater. Sci.* 12 **(1977)** 1028-1033. https://doi.org/10.1007/bf00540987.
[243] D. Wu, J. Zhang, J.C. Huang, H. Bei, T.G. Nieh, Grain-boundary strengthening in nanocrystalline chromium and the Hall–Petch coefficient of body-centered cubic metals, *Scr. Mater.* 68 **(2013)** 118-121. https://doi.org/10.1016/j.scriptamat.2012.09.025.
[244] Z.C. Cordero, B.E. Knight, C.A. Schuh, Six decades of the Hall–Petch effect – a survey of grain-size strengthening studies on pure metals, *Int. Mater. Rev.* 61 **(2016)** 495-512. https://doi.org/10.1080/09506608.2016.1191808.
[245] Z. Fan, P. Tsakiropoulos, P.A. Smith, A.P. Miodownik, Extension of the Hall-Petch relation to two-ductile-phase alloys, *Philos. Mag. A* 67 **(1993)** 515-531. https://doi.org/10.1080/01418619308207175.
[246] R. Madec, B. Devincre, L. Kubin, From dislocation junctions to forest hardening, *Phys. Rev. Lett.* 89 **(2002)** http://10.1103/PhysRevLett.89.255508.
[247] H. Yang, S. Kano, J. Shen, J. McGrady, Z. Zhao, Z. Duan, H. Abe, On the strength-hardness relationships in a Zr-Nb alloy plate with bimodal basal texture microstructure, *Mater. Sci. Eng. A* 732 **(2018)** 333-340. https://doi.org/10.1016/j.msea.2018.07.028.
[248] H.-G. Kim, I.-H. Kim, J.-Y. Park, Y.-H. Koo, Influence of alloy composition on work hardening behavior of zirconium-based alloys, *Nucl. Eng. Technol.* 45 **(2013)** 505-512. https://doi.org/10.5516/NET.07.2012.055.
[249] P. Li, Microstructure and mechanical properties of novel B2-type ductile Zr–Co–Cu alloys containing the B33 phase, *Mater. Res. Express* 4 **(2017)** https://doi.org/10.1088/2053-1591/aa80fc.
[250] C. Zhao, X. Chen, F. Pan, J. Wang, S. Gao, T. Tu, C. Liu, J. Yao, A. Atrens, Strain hardening of as-extruded Mg-xZn (x = 1, 2, 3 and 4 wt%) alloys, *J. Mater. Sci. Technol.* 35 **(2019)** 142-150. https://doi.org/10.1016/j.jmst.2018.09.015.
[251] K. Miyakusu, Y. Uematsu, K. Hoshino, Effect of Alloying Elements on Strain Hardening Exponent of Ferritic Stainless Steel, *Tran. ISIJ* 26 **(1986)** 228-235. https://doi.org/10.2355/isijinternational1966.26.228.
[252] A.I.O. Zaid, S.M.A. Al-Qawabah, Effect of Zr addition on the mechanical characteristics and wear resistance of Al grain refined by Ti after extrusion, *IOP Conference Ser. : Mater. Sci. Eng.* 146 **(2016)** https://doi.org/10.1088/1757-899x/146/1/012023.

[253] Z. Fan, H. Mingzhi, S. Deke, The relationship between the strain-hardening exponent n and the microstructure of metals, *Mater. Sci. Eng. A* 122 **(1989)** 211-213. https://doi.org/10.1016/0921-5093(89)90632-1.
[254] R. Silva, A. Pinto, A. Kuznetsov, I. Bott, Precipitation and Grain Size Effects on the Tensile Strain-Hardening Exponents of an API X80 Steel Pipe after High-Frequency Hot-Induction Bending, *Met.* 8 **(2018)** https://doi.org/10.3390/met8030168.
[255] S. Nagarjuna, B. Gopalakrishna, M. Srinivas, On the strain hardening exponent of Cu–26Ni–17Zn alloy, *Mater. Sci. Eng. A* 429 **(2006)** 169-172. https://doi.org/10.1016/j.msea.2006.05.096.
[256] J. Zhang, F. Sun, Z. Chen, Y. Yang, B. Shen, J. Li, F. Prima, Strong and ductile beta Ti–18Zr–13Mo alloy with multimodal twinning, *Materials Research Letters* 7 **(2019)** 251-257. https://doi.org/10.1080/21663831.2019.1595763.
[257] M. Dinu, S. Franchi, V. Pruna, C.M. Cotrut, V. Secchi, M. Santi, I. Titorencu, C. Battocchio, G. Iucci, A. Vladescu, 2.4 - Ti-Nb-Zr system and its surface biofunctionalization for biomedical applications, in: F.H. Froes, M. Qian (Eds.) Titanium in Medical and Dental Applications, Woodhead Publishing, Cambridge, United Kingdom, **2018**, 175-200. https://doi.org/10.1016/B978-0-12-812456-7.00008-1.
[258] P. Qin, Y. Chen, Y.-J. Liu, J. Zhang, L.-Y. Chen, Y. Li, X. Zhang, C. Cao, H. Sun, L.-C. Zhang, Resemblance in Corrosion Behavior of Selective Laser Melted and Traditional Monolithic β Ti-24Nb-4Zr-8Sn Alloy, *ACS Biomater. Sci. Eng.* 5 **(2019)** 1141-1149. https://doi.org/10.1021/acsbiomaterials.8b01341.
[259] Y. Abdelrhman, M.A.H. Gepreel, S. Kobayashi, S. Okano, T. Okamoto, Biocompatibility of new low-cost (α + β)-type Ti-Mo-Fe alloys for long-term implantation, *Mater. Sci. Eng. C* 99 **(2019)** 552-562. https://doi.org/10.1016/j.msec.2019.01.133.
[260] P. Qin, Y. Liu, T.B. Sercombe, Y. Li, C. Zhang, C. Cao, H. Sun, L.-C. Zhang, Improved Corrosion Resistance on Selective Laser Melting Produced Ti-5Cu Alloy after Heat Treatment, *ACS Biomater. Sci. Eng.* 4 **(2018)** 2633-2642. https://doi.org/10.1021/acsbiomaterials.8b00319.
[261] M. Morinaga, N. Yukawa, T. Maya, K. Sone, H. Adachi, in: P. Lacombe, R. Tricot, G. Béranger (Eds.) *Theoretical design of titanium alloys*, Sixth World Conference on Titanium, Les éditions de physique, Cannes, France, III, June 6-9, **1988**, 1601-1606.
[262] W. Zhu, J. Lei, C. Tan, Q. Sun, W. Chen, L. Xiao, J. Sun, A novel high-strength β-Ti alloy with hierarchical distribution of α-phase: The superior combination of strength and ductility, *Mater. Des.* 168 **(2019)** 107640. https://doi.org/10.1016/j.matdes.2019.107640.
[263] L. You, X. Song, A study of low Young′s modulus Ti–Nb–Zr alloys using d electrons alloy theory, *Scr. Mater.* 67 **(2012)** 57-60. https://doi.org/10.1016/j.scriptamat.2012.03.020.
[264] Y. Alshammari, F. Yang, L. Bolzoni, Mechanical properties and microstructure of Ti-Mn alloys produced via powder metallurgy for biomedical applications, *J. Mech. Behav. Biomed. Mater.* 91 **(2019)** 391-397. https://doi.org/10.1016/j.jmbbm.2018.12.005.
[265] D.C. Zhang, S. Yang, M. Wei, Y.F. Mao, C.G. Tan, J.G. Lin, Effect of Sn addition on the microstructure and superelasticity in Ti–Nb–Mo–Sn Alloys, *J. Mech. Behav. Biomed. Mater.* 13 **(2012)** 156-165. https://doi.org/10.1016/j.jmbbm.2012.04.017.
[266] J.I. Kim, H.Y. Kim, T. Inamura, H. Hosoda, S. Miyazaki, Shape memory characteristics of Ti–22Nb–(2–8)Zr(at.%) biomedical alloys, *Mater. Sci. Eng. A* 403 **(2005)** 334-339. https://doi.org/10.1016/j.msea.2005.05.050.

[267] H.Y. Kim, S. Miyazaki, Martensitic transformation and superelastic properties of Ti-Nb base alloys, *Mater Trans* 56 **(2015)** 625-634. https://doi.org/10.2320/matertrans.M2014454.
[268] S. Miyazaki, H.Y. Kim, H. Hosoda, Development and characterization of Ni-free Ti-base shape memory and superelastic alloys, *Mater. Sci. Eng. A* 438-440 **(2006)** 18-24. https://doi.org/10.1016/j.msea.2006.02.054.
[269] Y. Huang, M. Long, P. Liu, D. Chen, H. Chen, L. Gui, T. Liu, S. Yu, Effects of Partition Coefficients, Diffusion Coefficients, and Solidification Paths on Microsegregation in Fe-Based Multinary Alloy, *Metall. Mater. Trans. B* 48 **(2017)** 2504-2515. https://doi.org/10.1007/s11663-017-1045-2.
[270] L. Zhang, D.G. Eskin, A. Miroux, L. Katgerman, Role of Solute and Transition Metals in Grain Refinement of Aluminum Alloys under Ultrasonic Melt Treatment, in: W. H., R. A.D., C. W.A. (Eds.) ICAA13 Pittsburgh, Springer International Publishing, Cham, **2016**, 1389-1394. https://doi.org/10.1007/978-3-319-48761-8_212.
[271] M. Easton, D. StJohn, An analysis of the relationship between grain size, solute content, and the potency and number density of nucleant particles, *Metall. Mater. Trans. A* 36 **(2005)** 1911-1920. https://doi.org/10.1007/s11661-005-0054-y.
[272] G.A. Salishchev, R.M. Galeyev, O.R. Valiakhmetov, M.F.X. Gigliotti, B.P. Bewlay, C.U. Hardwicke, Effect of deformation conditions on grain size and microstructure homogeneity of β-rich titanium alloys, *J. Mater. Eng. Perform.* 14 **(2005)** 709-716. https://doi.org/10.1361/105994905X75493.
[273] M.R. Dal Bó, C.A.F. Salvador, M.G. Mello, D.D. Lima, G.A. Faria, A.J. Ramirez, R. Caram, The effect of Zr and Sn additions on the microstructure of Ti-Nb-Fe gum metals with high elastic admissible strain, *Mater. Des.* 160 **(2018)** 1186-1195. https://doi.org/10.1016/j.matdes.2018.10.040.
[274] D. Ding, D.C. Zhang, Z.C. Luo, C.G. Tan, Y. Zhang, J.G. Lin, Effects of Si addition on mechanical properties and superelasticity of Ti–7.5Nb–4Mo–2Sn shape memory alloy, *Mater. Des.* 61 **(2014)** 146-149. https://doi.org/10.1016/j.matdes.2014.04.043.
[275] J. Ma, I. Karaman, B. Kockar, H.J. Maier, Y.I. Chumlyakov, Severe plastic deformation of Ti74Nb26 shape memory alloys, *Mater. Sci. Eng. A* 528 **(2011)** 7628-7635. https://doi.org/10.1016/j.msea.2011.06.051.
[276] Y. Al-Zain, H.Y. Kim, H. Hosoda, T.H. Nam, S. Miyazaki, Shape memory properties of Ti–Nb–Mo biomedical alloys, *Acta Mater.* 58 **(2010)** 4212-4223. https://doi.org/10.1016/j.actamat.2010.04.013.
[277] Y. Shinohara, M. Tahara, T. Inamura, S. Miyazaki, H. Hosoda, Effect of Annealing Temperature on Microstructure and Superelastic Properties of Ti-Au-Cr-Zr Alloy, *Mater Trans* 56 **(2015)** 404-409. https://doi.org/10.2320/matertrans.M2014439.
[278] Y.J. Liu, S.J. Li, L.C. Zhang, Y.L. Hao, T.B. Sercombe, Early plastic deformation behaviour and energy absorption in porous β-type biomedical titanium produced by selective laser melting, *Scr. Mater.* 153 **(2018)** 99-103. https://doi.org/10.1016/j.scriptamat.2018.05.010.
[279] D. Raabe, 23 - Recovery and Recrystallization: Phenomena, Physics, Models, Simulation, in: D.E. Laughlin, K. Hono (Eds.) Physical Metallurgy (Fifth Edition), Elsevier, Oxford, **2014**, 2291-2397. https://doi.org/10.1016/B978-0-444-53770-6.00023-X.